High-Speed
Scanning Tunneling Microscopy
on Thin Oxide Film Systems

Dissertation zur Erlangung des akademischen Grades
doctor rerum naturalium
(Dr. rer. nat.)
im Fach Chemie
Spezialisierung:
Physikalische und Theoretische Chemie

eingereicht an der
Mathematisch-Naturwissenschaftlichen Fakultät
der Humboldt-Universität zu Berlin

von
M.Sc. Leonard Gordian Gura

Präsidentin der Humboldt-Universität zu Berlin:
Prof. Dr Julia von Blumenthal
Dekanin der Mathematisch-Naturwissenschaftlichen Fakultät:
Prof. Dr. Caren Tischendorf

Gutachter:

1. Prof. Dr. Hans-Joachim Freund
2. Prof. Dr. Klaus Rademann
3. Prof. Dr. Hans-Peter Steinrück

Tag der mündlichen Prüfung: 27.02.2023

Leonard Gordian Gura: *High-Speed Scanning Tunneling Microscopy on Thin Oxide Film Systems*

Diese Dissertation wurde von Dezember 2017 bis November 2022 am Fritz-Haber-Institut in Berlin unter Leitung von Herrn Professor Dr. Hans-Joachim Freund angefertigt.
Das Projekt wurde vom European Research Council (ERC) im Rahmen des European Unions Horizon 2020 Research and Innovation Program (Grant Agreement Nr. 669179) gefördert.

"La sapienza è figliola dell'esperienza."

"Wissen ist das Kind der Erfahrung."

Leonardo da Vinci (1452 - 1519)

ABSTRACT

Dynamics related to thin silicon- and germanium dioxide films that are grown on Ru(0001) crystals are investigated. Between the film and the metal support oxygen species are present that play a crucial role for these film systems. First, these oxygen adlayers on Ru(0001) are analyzed by high-speed scanning tunneling microscopy (STM) with the focus on dynamic processes. In a next step, the monolayer of germanium dioxide, termed also germania, supported on Ru(0001) is studied at elevated frame rates. For the structural analysis of the two-dimensional oxide network, a semi-automated network detection tool is developed. Finally, the bilayer of silicon dioxide, termed also silica, on Ru(0001) is studied by conventional and by high-speed STM both at room temperature and at elevated temperatures of 600 K.

To realize fast STM measurements at elevated temperatures, a high-speed STM is designed and built that can operate at variable temperatures. Mechanical and electronic components are custom designed. For high-speed STM measurements, an unconventional spiral scan pattern is implemented for the first time. Frame rates of 120 Hz are achieved without reaching the limits of the mechanical setup. The high-speed images are free of drift and distortion artifacts.

With the spiral scan approach, the dynamics in oxygen adlayers are investigated for the first time at elevated frame rates. Experimental results are supported by density functional theory (DFT) calculations performed externally. Dynamic events are observed in the oxygen adlayers that are stable at room temperature, namely O(2×2)/Ru(0001), O(2×1)/Ru(0001), and 3O(2×2)/Ru(0001). The occupation of an intermediate state along the oxygen diffusion pathway and fast "flipping" events of atomic one-dimensional stripe patterns are observed.

On the germania monolayer on Ru(0001), complex domain boundary structures are resolved with high-speed STM. In high-speed measurements on the silica bilayer on Ru(0001), dynamic changes of the imaging contrast are observed that may relate to the mobile species in the oxygen interfacial layer. Measurements at elevated temperature reveal dynamic contrast changes of mesoscopic features. These measurements constitute the first high-speed STM scans on the silica film at elevated temperatures and form the basis for future studies with the focus on dynamic processes in thin oxide film systems. One of the most encouraging long-term objectives is the observation of dynamic processes at the atomic scale in real space and in real time resulting in the structural transformation between crystalline and vitreous networks.

ZUSAMMENFASSUNG

Dünne Silizium- und Germaniumdioxidfilme auf Ru(0001)-Kristallen werden hinsichtlich dynamischer Prozesse untersucht. Zwischen Oxidfilm und Substrat befinden sich Sauerstoffatome, die eine entscheidende Rolle in diesen Systemen spielen. Zunächst werden diese Sauerstofflagen auf Ru(0001) mittels Hochgeschwindigkeits-Rastertunnelmikroskopie (STM) analysiert. Daraufhin wird die Germaniumdioxid-Monolage auf Ru(0001) bei hohen Bildraten untersucht. Für die Strukturanalyse der Oxidnetzwerke wird eine halbautomatische Netzwerkdetektion entwickelt. Schließlich wird die Siliziumdioxid-Bilage auf Ru(0001) mit konventionellen sowie mit schnellen STM-Messungen bei Raumtemperatur und bei erhöhten Temperaturen von 600 K abgebildet.

Um schnelle Messungen bei erhöhten Temperaturen zu realisieren, wird ein Hochgeschwindigkeits-STM mit selbstentwickelten mechanischen und elektronischen Kompenententen konstruiert, welches bei unterschiedlichen Temperaturen betrieben werden kann. Erstmals werden unkonventionelle Spiralgeometrien für schnelle STM-Messungen verwendet. Damit werden Bildraten von 120 Hz erreicht, ohne an Grenzen des mechanischen Aufbaus zu stoßen. Die Hochgeschwindigkeitsbilder zeigen weder Driftartefakte noch Verzerrungen.

Die adsorbierten Sauerstofflagen werden zum ersten Mal bei hohen Bildraten untersucht. Die experimentellen Ergebnisse werden durch extern durchgeführte Dichtefunktionaltheorie-Berechnungen ergänzt. In den bei Raumtemperatur stabilen Sauerstofflagen O(2×2)/Ru(0001), O(2×1)/Ru(0001) und 3O(2×2)/Ru(0001) werden dynamische Prozesse beobachtet. Die Besetzung des Zwischenzustandes entlang des Diffusionspfades und schnelle "Umklapp"-Prozesse eindimensionaler Linien werden auf atomarer Ebene aufgelöst.

Komplexe Domänengrenzen in der Germaniumoxid-Monolage auf Ru(0001) werden mit Hochgeschwindigkeits-STM abgebildet. Die Messungen an der Siliziumdioxid-Bilage auf Ru(0001) zeigen dynamische Änderungen des Abbildungskontrasts, die möglicherweise mit den mobilen Sauertsoffatomen an der Grenzfläche zusammenhängen. Messungen bei hohen Temperaturen zeigen dynamische Kontraständerungen von mesoskopischen Strukturen. Diese Messungen stellen die ersten STM-Hochgeschwindigkeitsaufnahmen des Siliziumdioxidfilms bei hohen Temperaturen dar und bilden die Grundlage für künftige Studien zu dynamischen Veränderungen in dünnen Oxidschichtsystemen. Eines der Langzeitziele ist die Beobachtung atomarer dynamischer Prozesse im Realraum und in Echtzeit, die zur strukturellen Umwandlung zwischen kristallinen und gläsernen Netzwerken führen.

CONTENTS

LIST OF FIGURES

LIST OF TABLES

ACRONYMS

1D	one-dimensional
2D	two-dimensional
AES	auger electron spectroscopy
AFM	atomic force microscopy
ALD	atomic layer deposition
CAV	constant angular velocity
CLV	constant linear velocity
CPU	central processing unit
DAC	digital-to-analog converter
DFT	density functional theory
EPICS	experimental physics and industrial control system
HDF5	hierarchical data format version 5
FIM	field ion microscopy
FS	fast-scan
GUI	graphical user interface
IETS	inelastic electron tunneling spectroscopy
LDOS	local densitiy of states
LEED	low-energy electron diffraction
LEEM	low-energy electron microscopy
LHe	liquid helium
LN2	liquid nitrogen
ML	monolayer
OV	overview
PV	process variable
RAG	region adjacency graph
RPA	random phase approximation
RTEMS	real time executive for multiprocessor systems
SCAN	strongly-constrained-and-appropriately-normed
STM	scanning tunneling microscopy
SPM	scanning probe microscopy
TEM	transmission electron microscopy
TSP	titanium sublimation pump

UHV ultra-high vacuum

VMEbus Versa Module Eurocard-bus

XRD X-ray diffraction

Part I

INTRODUCTION

1 MOTIVATION

Electronic devices, electrochemical systems, and catalysts are omnipresent in our everyday lives, in science, and in technology. For the continuous improvement and further development of these applications, their underlying fundamental dynamic processes must be understood. Dynamics of importance include chemical and physical reactions, compound formation, concentration fluctuations, phase transformations, and diffusion in general. [1, 2]

To fully understand these dynamics and their origin, the knowledge of fundamental processes occurring at the atomic scale is crucial. However, most processes of interest include complex multi-step mechanisms that are not directly experimentally accessible. Therefore, reducing the complexity of the studied system by using adequate model systems constitutes a sophisticated approach to assess fundamental processes at the atomic level.

The design of adequate model systems may consist of the reduction of its dimensionality from three to two dimensions. Instead of investigating bulk properties that are only accessible to diffraction, spectroscopy methods, and other averaging techniques, well defined surfaces can be prepared. These atomically flat surfaces can be investigated with well established surface science tools. The famous work of Gerhard Ertl and coworkers is an excellent example of how surface science revealed individual steps of the ammonia synthesis resulting in the comprehensive understanding of the overall process. [3]

The versatile toolbox of surface science enables the investigation of phenomena in real space and has the great advantage that experiments can be performed at various temperatures. Measurements ranging from cryogenic temperatures up to several hundred degrees Celsius are possible. On the one hand, variable temperatures influence the degree of complexity of the measurement. On the other hand, by measuring at various temperatures, the rates of temperature dependent reactions and phenomena can be tuned and dynamic processes become accessible. Considering these possibilities, surface science tools are promising to assess dynamics at the atomic scale on surfaces and other atomically flat sample systems, such as 2D materials.

Motivated by this prospect, this thesis describes the development and implementation of an ultra-high vacuum (UHV) chamber system that includes standard surface science tools and is designed to perform high-speed scanning tunneling microscopy (STM) measurements at variable temperature. For high-speed STM measurements, innovative spiral scan patterns are implemented. With the new spiral scanning,

dynamics at surfaces are investigated, focusing on surface diffusion of chemisorbed oxygen atoms on the Ru(0001) surface. The present studies reveal that the increased image acquisition rate and the continuous data sampling allows STM to shed light on physical chemistry questions with a new precision in time resolution. This approach, which constitutes the beginning of a possible paradigm shift in the field of STM scanning, allows to revisit well-known sample systems and to solve interesting future questions in fundamental and applied science.

2 LITERATURE REVIEW

2.1 DYNAMICS ON SURFACES

The approach to investigate dynamic processes at surfaces opens the possibility to study many physical and chemical phenomena. Surface studies include the interaction with the medium at the interface, such as liquid or gaseous environments. These interactions are important, especially in catalysis. In catalysis research, the movement of reactants to the reaction site is one of the most essential processes. In many cases, the influence of adsorbed surface species on the solid surface plays a major role. [1, 4] Interesting research questions include, how individual adsorbed species evolve to two-dimensional (2D) phases and how compounds form on surfaces. For thin film growth in general, the processes that affect the epitaxy are of great interest. Especially surface diffusion can determine the growth and the reaction mechanisms. [5] To elucidate these processes, the underlying fundamental mechanisms must be understood.

For many dynamic processes on surfaces at finite temperatures, surface diffusion plays a major role. [4] 100 years ago, the first experimental evidence for surface diffusion was provided by Volmer and Estermann, who observed the fast growth of mercury crystals on the macroscopic scale. [6] Since then, a variety of different experimental methods has been developed to study mobile surface species. The observation of individual atoms was possible with field ion microscopy (FIM) invented by Müller in 1951. [7] Graham and Ehrlich, for instance, observed the diffusion of a pair of tungsten adatoms, as shown in Figure 2.1. [8]

The example in Figure 2.1 illustrates a common approach to assess dynamics. Individual, independent snapshots are acquired in a static configuration, e.g. at low temperature. Drawing conclusions from the comparison of these snapshots can give insights to some underlying mechanisms. However, the fundamental processes remain unrevealed because the dynamics are not directly observed. The direct observation of dynamic processes is challenging due to the fast timescales.

Figure 2.2 provides an overview of timescales and corresponding frequency ranges of fundamental physical and chemical processes. Acquisition speeds of various methods used to investigate dynamic processes are indicated.

At high frequencies beyond the GHz regime, spectroscopy techniques like inelastic electron tunneling spectroscopy (IETS) and THz-STM can resolve motions at the atomic scale. By combining pump-

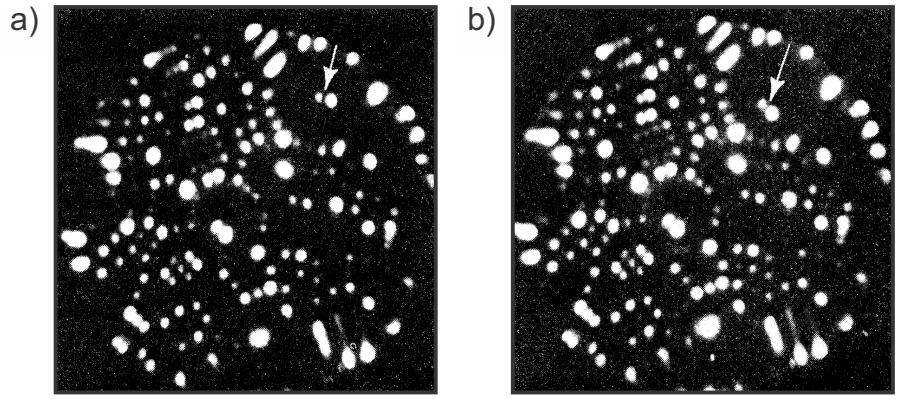

Figure 2.1: Surface self-diffusion of atom pairs captured with FIM. FIM micrographs acquired at 15 K showing the [111] tungsten surface. In the time of 13 min between a) and b), the sample was heated thirteen times to 275 K. Moving pairs over the 211 planes are observed, highlighted with white arrows. Reprinted with permission from Ref. [8]. Copyright 1973 by the American Physical Society.

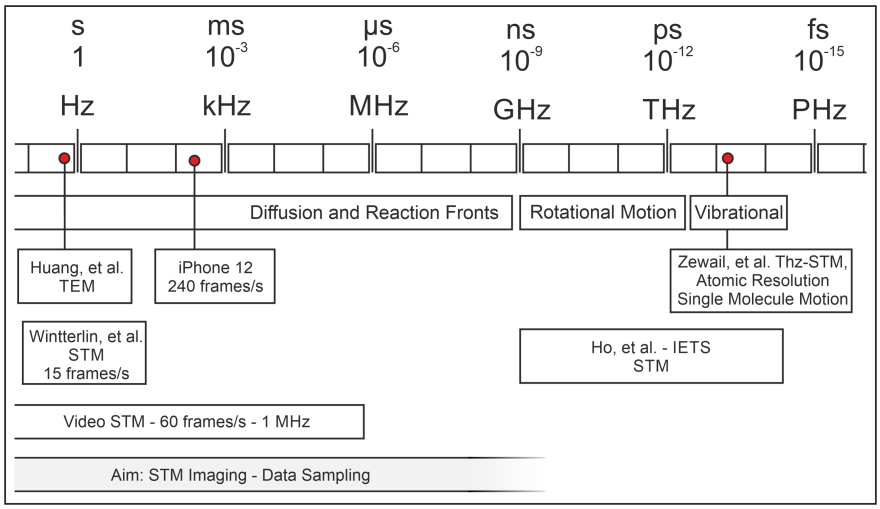

Figure 2.2: Overview of experimental imaging and spectroscopy techniques. The methods are assigned to their acquisition speed. Timescales of fundamental chemical and physical processes are indicated at the top. Reproduced from Ref. [9], licensed under a Creative Commons Attribution (CC BY) license.

probe techniques [10] with STM, dynamics in the subpicosecond regime can be studied. Voltage or THz laser pulses create excited states in the tunneling junction and their decay can be studied using spectroscopy methods. [11–15] IETS measures additional current contributions caused by inelastic excitation processes in the tunneling junction. With these measurements, vibrational and rotational properties of molecules can be assessed at the femtosecond timescale. [16–18] During these measurements, the STM tip rests at a fixed position. The

drawback of these methods is that the dynamics cannot be monitored in real space and that solely reversible processes can be assessed.

To monitor dynamics in real space, in real time, and at the atomic scale, the acquisition rate of conventionally slow microscope types can be increased. For instance, Huang et al. imaged with 0.5 frames/s with their transmission electron microscopy (TEM). While TEM can be used to study thin films, it cannot be applied to solid surfaces.

The invention of the scanning tunneling microscope in 1982 enabled the investigation of atomic structures with extraordinary spatial resolution. [19] Due to its high spatial resolution, STM is a well established surface science tool to investigate atomic structures on surfaces. STM revealed surface structures [20–22] and surface properties. [23, 24]

The drawback of conventional STM is its slow acquisition time of typically more than 100 s per image. Compared to these slow image rates, the dynamic processes of interest are on different timescales. Although today conventional STM measurements are acquired with slow tip velocities and long image acquisition times, surprisingly, already several years after the invention, efforts were made to increase the scan speed of STM. In a recent contribution, we give an overview of attempts to increase the frame rate in STM, which is outlined in the following. [25]

Already a few years after its invention, the advantages of higher scan speeds were discussed. The major purpose was to reduce low frequency noise, $1/f$ noise and hysteresis of the piezoelectric scanner. [26] Bryant et al. measured the graphite surface with line scan frequencies of 1 kHz and averaged several consecutive images over time. [26] Figure 2.3 compares the slow scan on the graphite surface with a line scan frequency of 10 Hz in a) and the average of consecutive high line frequency scans on the graphite surface in b). The averaged high line frequency STM image in Figure 2.3b is slightly distorted. Nevertheless, it enables the assignment of the hexagonal arrangement of carbon atoms.

The advantages of high-speed STM were well known since then and the perspective was to resolve dynamic processes. Several other groups worked on increasing the scan speed of STM [28–30] until Wintterlin et al. in 1997 resolved the first dynamics at the atomic scale by high-speed STM. [31]

The fact that it took more than 10 years from the initial approach to increase the scan speed in STM significatnly to the first resolved atomic dynamics, illustrates the complexity to increase the frame rate of STM without sacrificing its outstanding spatial resolution.

Since then high-speed STMs have been developed and measurements were performed in vacuum, in a gas atmosphere, and in liquid. Table 2.1 gives an exemplary overview of studied systems and achieved frame rates.

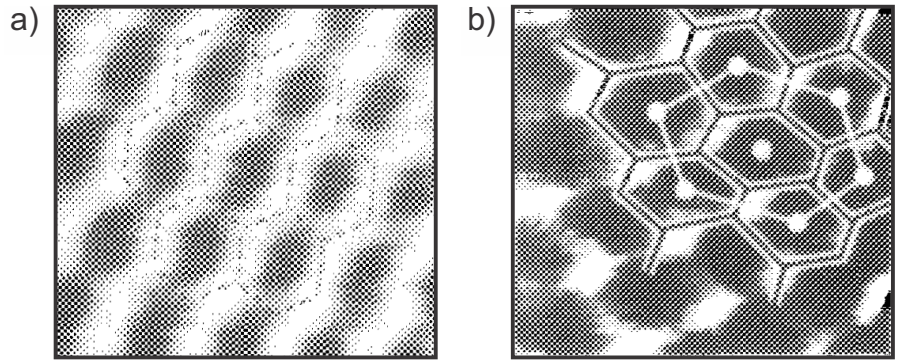

Figure 2.3: High line frequency in STM scans. a) The graphite surface is imaged with the conventional slow raster scan with a scan frequency of 10 Hz. (V_S = 10 mV, I_T = 5 nA) Adapted from Ref. [27], with the permission of AIP Publishing.. b) The average of several scans with high line frequencies of 1 kHz are shown. (V_S = 40 mV, I_T = 1 nA) Adapted from Ref. [26], with the permission of AIP Publishing.

Table 2.1: Studied sample systems by state-of-the-art high-speed STMs. Achieved frame rates and corresponding scanning parameters are listed. Adapted from [9], licensed under a Creative Commons Attribution (CC BY) license.

Condition	Sample system	Image size (nm^2)	Resolution	frame rate (Hz)	Ref.
RT-UHV	O diffusion on Ru(0001)	8 × 8	atomic	15	[31]
Liquid	S diffusion on Cu(100)	9.4 × 9.4	atomic	20	[2]
Ambient	static HOPG	1 × 1	atomic	52	[32]
LT-UHV	molecular self-assembly	6 × 6	sub-molecular	60	[33]
HT-UHV	graphene growth on Ni(111)	1.5 × 3	atomic	60	[34]
RT-UHV	static HOPG	5 × 5	atomic	80	[35]
HT-UHV	surface reconstruction of Rh(110)	6.5 × 6.5	atomic row	100	[36]

Figure 2.4 covers some examples of fast STM measurements reported in literature. The investigated physical and chemical processes include graphene growth, deconstruction of atomic rows, and diffusion in the context of electrochemical applications and catalytic reactions.

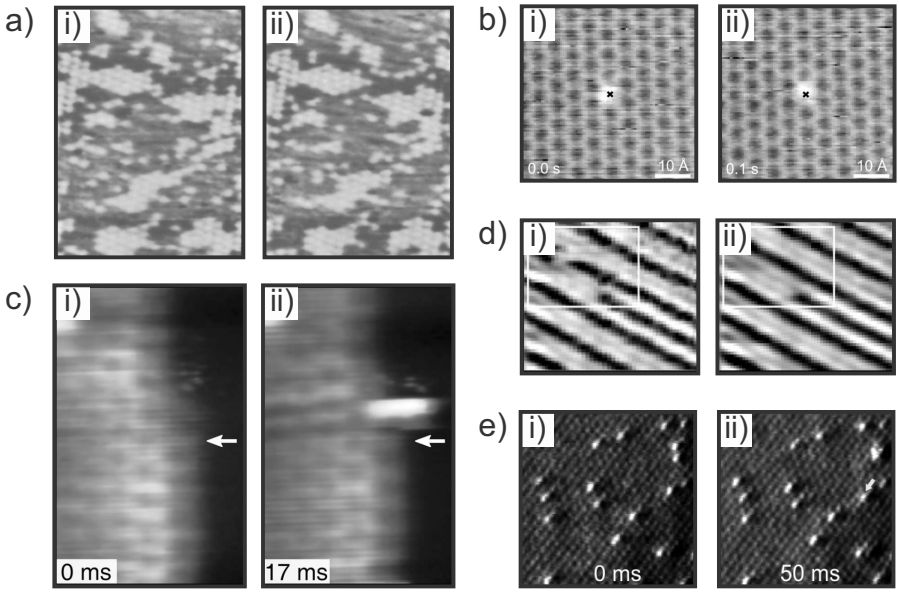

Figure 2.4: Overview of fast STM measurements. a) Diffusion of chemisorbed oxygen on Ru(0001) (V_S = -1.6 V, I_T = 3 nA, scan area = 8 × 19 nm^2, T = 300 K 6 frames s^{-1}). b) Diffusion of embedded oxygen in CO/Ru(0001) (V_S = -0.22 V, I_T = 10 nA, scan area = 5 × 5 nm^2, T = 300 K, 10 frames s^{-1}). c) Graphene growth on Ni(111) (V_S = 0.02 V, I_T = 7 nA, scan area = 1.6 × 2.5 nm^2, T = 710 K, 60 frames s^{-1}). d) Deconstruction of the oxygen covered Rh(110) surface in hydrogen atmosphere (T = 473 K, 100 frames s^{-1}) e) Sulfur adatom diffusion on the Cl covered Cu(100) surface in 0.01m HCl at -0.32 V versus a standard calomel electrode. (20 frames s^{-1})
a) Reprinted from Ref. [31], Copyright 1997, with permission from Elsevier Science B.V. b) From [37]. Reprinted with permission from AAAS. c) From Ref. [34]. Reprinted with permission from AAAS. d) Reprinted from Ref. [36], with the permission of AIP Publishing. e) Adapted from Ref. [2], Copyright 2019 Wiley-VCH Verlag GmbH & Co. KGaA, Weinheim.

All the examples shown in Figure 2.4 and in general all high-speed STMs, so far, use sinusoidal raster scans. It is well known that the conventional raster scan motion in scanning probe microscopy (SPM) is not favorable at high scan speeds. [38–46] Nevertheless, in contrast to other scanning microscopy techniques, STM still restricts to the raster paradigm. [42, 44, 47–49] Altering the scan motion might be a promising pathway to generally increase the frame rate of STM. The high impact that STM has in surface science might transfer even faster to important fields like electrochemistry, biology, and materials science.

[50] Certainly, higher imaging rates would lead to broader applications of STM in science and industry.

2.2 OXYGEN ON RU(0001)

Chemisorbed oxygen on Ruthenium was one of the first sample systems to study surface diffusion in UHV. [4, 51] It serves as model system for gas adsorption, catalytic reactions, including water splitting applications, and therefore, has been studied extensively during the last decades. [52–54]

As mentioned in Section 2.1, the first video STM resolved atomic equilibrium fluctuations of chemisorbed oxygen atoms on the Ru(0001). [31] Since then, the mobility of single oxygen species at low oxygen coverages is well known. However, for thin film growth or model catalyst preparation, dense oxygen adlayers and the oxygen mobility in these layers are very important.

At room temperature, several ordered phases of chemisorbed oxygen on Ru(0001) exist. [31, 55–58] Figure 2.5a shows the schematic mechanism of adsorption and dissociation of the oxygen molecules (red balls) on the Ru(0001) surface (gray balls).

The superstructures depend on the temperature during exposure and the amount of dosed oxygen. [54, 57] The oxygen concentration on the surface is expressed as the coverage θ, which represents the fraction of occupied hcp sites with respect to the total number of available hcp sites on the Ru(0001) surface. In the case of full coverage (θ=1), every hcp hollow site on the Ru(0001) surface is occupied by an oxygen atom, as shown in Figure 2.5b. Figures 2.5c-e show the structures of the O(2×2), the O(2×1), and the 3O(2×2) adlayers, respectively. The O(2×2) and the 3O(2×2) structure with a coverage of θ=0.25 and 0.75, respectively exhibits hexagonal lattices as shown in the STM images in Figures 2.5f,h. The O(2×1) structure results in characteristic one-dimensional (1D) lines in STM measurements, as shown in Figure 2.5g. [54, 56, 57].

The only estimation of hopping rates within the O(2×2) adlayer is based on conventional STM measurements. [62] Atomic jumps every 100 to 50 s were determined, which agrees with the expectation that the mobility decreases with increasing oxygen coverage. [31, 62] Apart from these studies, in the literature, no real space experimental quantification of the oxygen mobility within the dense oxygen adlayers is reported. This is surprising considering that the diffusion inside the adlayers is of great importance for the interactions to water on the Ru(0001) surface [63–66] and the thin film growth of materials, such as graphene, [67, 68] silicates, [69] and silica. [70] Especially for the preparation of atomically flat silicon- and germanium oxide thin films, the 3O(2×2) adlayer is essential. These film systems will be described in Section 2.3.

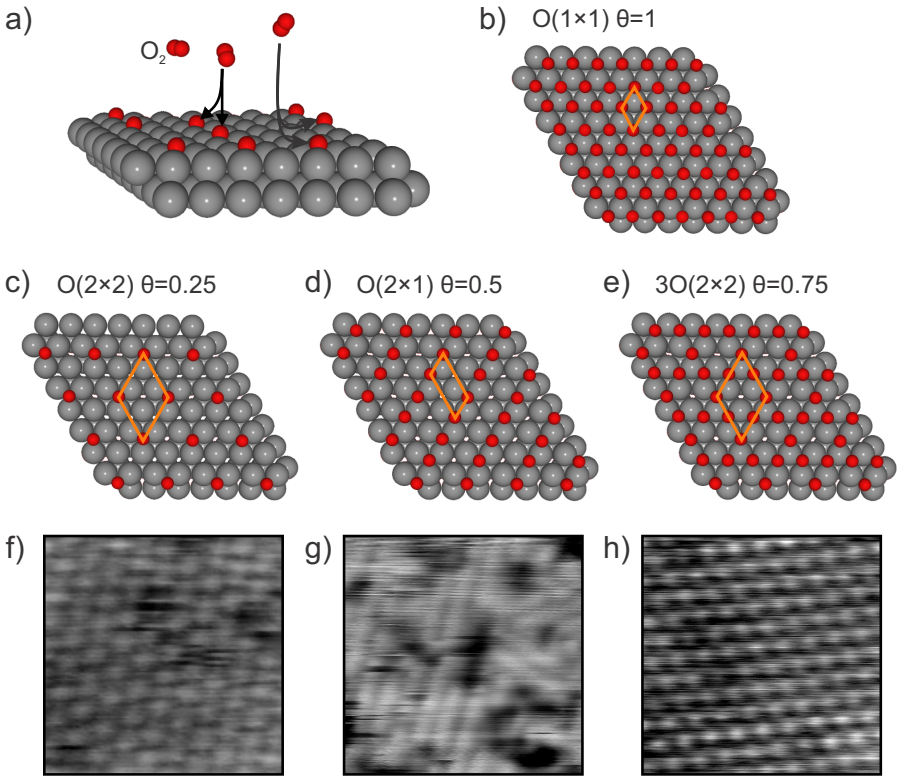

Figure 2.5: Schematic of oxygen adsorption on Ru(0001). a) Molecular oxygen dissociates and oxygen atoms chemisorb on the Ru(0001) surface. b) $O(1 \times 1)$ adlayer correponsing to a full coverage of $\theta = 1$. c) $O(2 \times 2)$ adlayer correponsing to a coverage of $\theta = 0.25$. d) $O(2 \times 1)$ adlayer correponsing to a coverage of $\theta = 0.5$. e) $3O(2 \times 2)$ adlayer correponsing to a coverage of $\theta = 0.75$. c-e) are stable structures at room temperature. f-h) Conventional STM images acquired in constant current mode at room temperature (5 nm×5 nm). f) V_S = 1 V, I_T = 1.4 nA. g,h) V_S = 1 V, I_T = 1 nA. Based on Refs. [59–61].

2.3 ULTRATHIN OXIDE FILMS

One of the naturally most abundant and at the same time technological most relevant oxides is silicon dioxide, also known as silica. Besides its crystalline phases, silica exhibits the amorphous or vitreous phase: glass. The nature of the glassy state, especially its atomic structure is one of the main research questions in this day and age. [71] The great importance of this material is reflected in the fact that the year 2022 was officially declared by the United Nations General Assembly as the International Year of Glass. [72]

As described at the beginning of this chapter, 2D materials can serve as model systems to answer fundamental research questions. Approximately ten years ago, the 2D silica film was prepared on Ru(0001) pre-covered with oxygen. [73–75] Figure 2.6a shows the Ru(0001) surface covered with atomic oxygen. The system was introduced in

Section 2.2 and serves as the starting point for the preparation of thin silica films on Ru(0001). The silica monolayer is shown in Figure 2.6b. The monolayer phase is chemically bound to the metal substrate.[74] At higher SiO_2 coverages, the silica bilayer forms, as shown in Figure 2.6c. The bilayer phase is dispersively bound to the underlying metal substrate by van der Waals forces. After the film preparation, interfacial oxygen adlayers remain at the interface, as indicated by the oxygen atoms (red balls) in Figure 2.6.

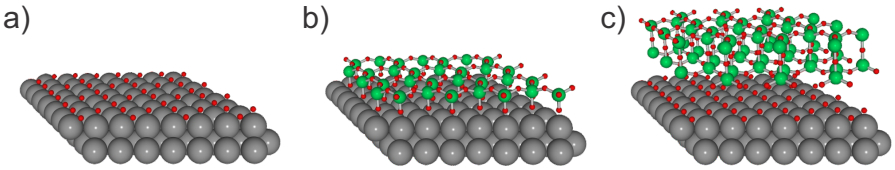

Figure 2.6: Schematic representation of 2D silica on Ru(0001). a) The Ru(0001) surface is covered with atomic oxygen. b) The silica monolayer is chemically bound on Ru(0001). c) The silica bilayer is van der Waals bound to the substrate. The atoms are color coded (O: red balls, Si: green balls, Ru: gray balls). Adapted from Ref. [76].

The preparation of atomically flat 2D silica films enabled the application of surface science tools. This constitutes the sophisticated approach to study the atomic structure of the glass former at the atomic scale in real space. Figure 2.7 shows low temperature STM images of the silica bilayer on the oxygen covered Ru(0001) surface. The positions of silicon and oxygen atoms are superimposed by green and red balls, respectively. Rings of different sizes are detected that are labeled as n-membered rings, where n is the number of silicon atoms per ring. While in the left STM image only 6-membered rings are identified, in the right STM image 4- to 9-membered rings are identified. The different ring structures result in a non-periodic arrangement. This vitreous phase of the silica bilayer represents the 2D model silica glass. [75] Structural analyses of the vitreous phase confirmed theoretical models of the atomic structure of glass proposed by Zachariasen in 1932. [75, 77, 78] The vitreous and the crystalline phase can coexist on the same sample. [79]

In the last decade, the silica film has been studied thoroughly. Characteristic structural parameters such as the interatomic distances and bond angles in the 2D film are comparable to values for 3D silica glass determined by X-ray diffraction (XRD), neutron and X-ray scattering. [75, 79] This agreement legitimates to transfer insights gained on 2D silica to 3D. [80] The silica film inertness was proven by atomic force microscopy (AFM) measurements in liquid. [81] Silica ring-ring distances that show characteristic values of approximately 0.54 nm were used to compare the network structure in UHV and in liquid. [81] Beyond the investigation of the near range order, the mesoscopic structure of the silica film was studied. [82] Furthermore, integrative studies have been performed that relate to the mesoscopic features like

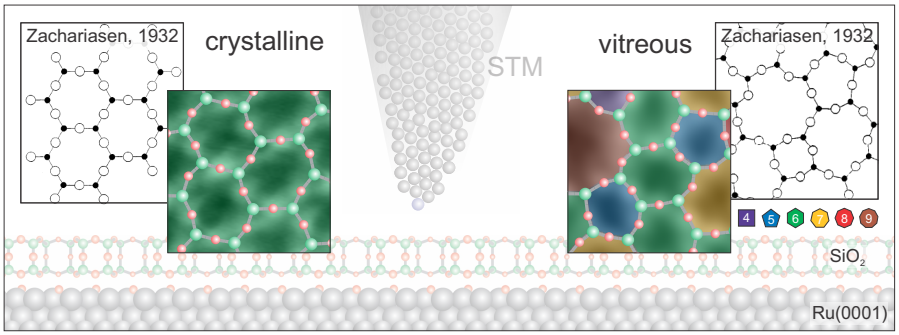

Figure 2.7: Comparison of crystalline and vitreous 2D silica. STM images of the crystalline and vitreous phase of the silica bilayer supported on oxygen covered Ru(0001) are shown in the front (V_S = 0.1 V, I_T = 0.1 nA, scan area = 1.3 nm × 1.3 nm, T = 5 K). The silica rings are color coded according to the legend provided on the right. The side view of the structural model is drawn in the back. The schematic top view provided by Zachariasen in 1932 is shown in the upper left and right corner for the crystalline and vitreous phase, respectively. [77] Adapted with permission from Ref. [78]. Copyright 2012 American Chemical Society.

the coverage of metal edges and mechanical properties. The bending rigidity of the silica bilayer was derived from inelastic helium atom scattering data. A detailed review, including a chronological list of breakthroughs in the field of structural studies of 2D silica films is provided in Ref. [76]

One of the important milestones in understanding the formation of the 2D silica film was the discovery of a metastable phase. This metastable phase is a 2D zigzag polymporph of silica that exhibits intermediate coupling characteristics to the substrate compared to the monolayer and bilayer phase. [83] Most importantly, silica is not the only oxide exhibiting this broad structural diversity, including vitreous networks. Germanium oxide, termed also germania, grows in different structural configurations depending on the underlying metal substrate. Figure 2.8 provides an overview of known silica and germania phases on different substrate materials. The stable phases depend on the film-substrate interaction. A detailed comparison of the oxide film systems is provided in Ref. [84].

In the key modern technologies of electronic devices, integrated circuites, and optical fibers, both silica and germania play a crucial role. High accuracy in terms of structural defects is required, making the 2D model systems of germania and silica films interesting for atomic structure studies. Potential applications of the 2D oxides extend beyond conventional transistors and optical fibers.

It was shown that the 2D silica bilayer film can be lift off and transferred freely to other substrates, as schematically shown in Figure 2.9a. [85] Recent advances in preparing silica films on larger scales with atomic layer deposition (ALD) based methods open new perspectives

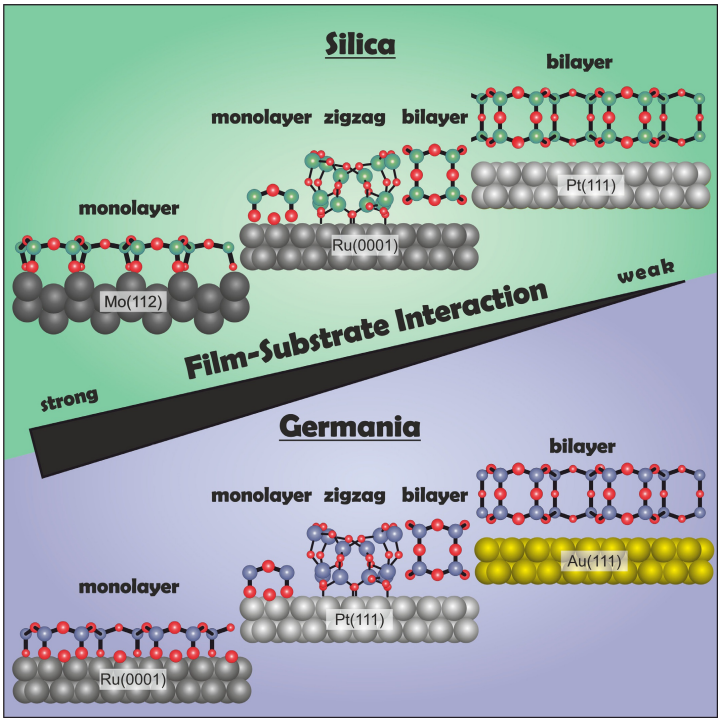

Figure 2.8: Overview of glass-former materials on various metal supports. Selected substrates that support 2D silica and germania films ranging from monolayer over zigzag to bilayer films. Both silica and germania bilayer films consist of tetrahedral XO_4 (X = Si, Ge) building blocks that form crystalline or vitreous network structures. The comparison emphasizes the influence of the underlying metal substrate on the stable phases of the two oxide network formers. Reproduced from Ref. [84]. Copyright 2020 The Authors. Published by Wiley-VCH GmbH.

to use the insulating oxide layer in 2D stacked heterostructures, as schematically shown in Figure 2.9b. [86]

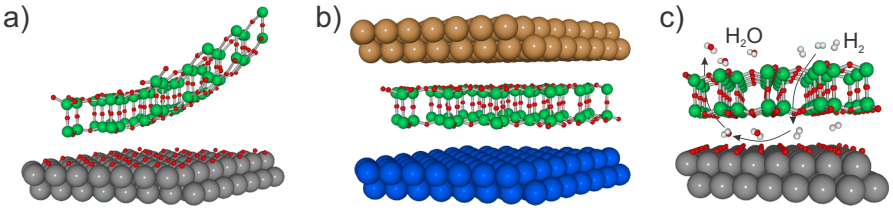

Figure 2.9: Schematic drawing of the 2D silica in applications. a) The silica bilayer is mechanically removed from the substrate. b) The silica bilayer is placed onto another arbitrary substrate to form a stacked 2D heterostructure. c) Hydrogen penetrates the silica bilayer and reacts with interfacial oxygen to water in the confined space formed by the silica film and the substrate. The atoms are color coded (O: red balls, Si: green balls, Ru: gray balls, arbitrary 2D layers: blue and yellow balls). Adapted from Ref. [76].

Due to the different pore sizes, 2D silica has the potential to act as size-selective permeable membrane in 2D heterostructures. [80] In catalysis, it may be applied as 2D confining layer that is selective in terms of particle shape and size. [80] As evident from recent advances in the field of 2D silica, the research interest shifts towards dynamic phenomena related to the oxide film. Permeation experiments were performed revealing that the chemical affinity toward the silica layer affects the permeance. [87] Future mass-transfer studies can lead to a better understanding of the effects of different pore sizes. The porous structure of the 2D silica film supported on Ru(0001) enables the penetration of oxygen, which then dissociates on the Ru(0001) surface into atomic oxygen. [88] The interfacial oxygen can be removed upon thermal annealing in hydrogen atmosphere. Hydrogen can penetrate the silica film and react with the interfacial oxygen to water. The dynamic reaction front of this process was monitored with the averaging technique low-energy electron microscopy (LEEM) in real space and in real time. [89]

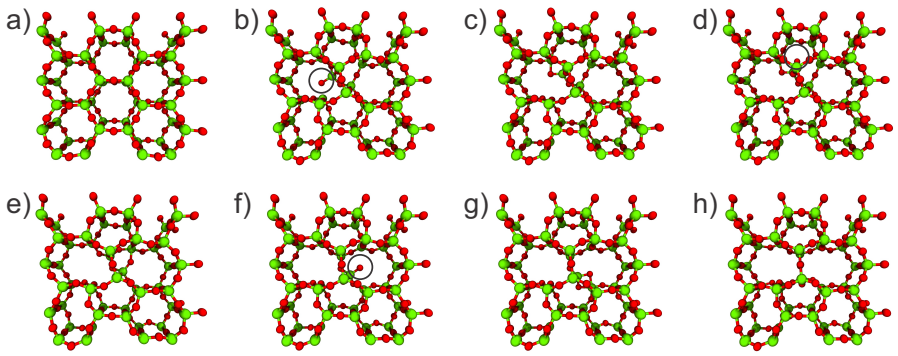

Figure 2.10: Structural reformations in the silica bilayer. Intermediate structures during the formation processes of a Stone-Wales defect based on density functional theory (DFT) calculations. Changes in the lower layer are shown exemplarily. Black circles mark temporarily existing dangling bonds. Extracted from Ref. [90]. Copyright 2020 the authors. Published by Wiley-VCH Verlag GmbH & Co. KGaA, Weinheim.

In addition to dynamic processes through and underneath the silica film, the dynamics within the film system are of great interest. Structural modifications in the silica film supported on graphene were observed with TEM using the electron bombardment as trigger to activate the dynamic processes. [91] Thermally activated structural changes were monitored in reciprocal space by time-dependent low-energy electron diffraction (LEED) studies. [90] For the structural conversion from the crystalline to the vitreous phase in UHV conditions, an apparent activation barrier of 4.2 eV was determined. This value agrees with the calculated energy barrier of 4.3 eV to form a Stone-Wales-like defect. Supporting DFT calculations propose a complex sequence of

structural changes in the upper and lower layer of the silica bilayer. [90] Exemplary snapshots of this breaking and making of bonds in the lower layer are shown in Figure 2.10. The black circles in Figures 2.10b,d,f mark temporarily existing dangling bonds.

As obvious from these studies, thermally activated dynamic processes in, on top of, and underneath the oxide film systems are very important. A fundamental understanding of these dynamics is crucial to optimize the growth characteristics of the films and to design future application like 2D heterostructures. The dynamics of atomic species under or on top of the oxide is of great interest, especially for catalytic reactions.

With the present work we pave the way for time resolved STM studies in real space on the thin oxide film systems at variable temperature. The underlying fundamental considerations and the design of a high-speed variable temperature STM are described in the following sections.

Part II

EXPERIMENTAL DETAILS

3 TECHNIQUES

This chapter describes the working principles of STM and emphasizes the limitations and challenges with respect to high-speed STM. The discussion of the main limitations in Section 3.2 is part of Ref. [25]. Our experimental setup including the UHV chamber and the STM is discussed in Chapter 5 of this thesis.

3.1 SCANNING TUNNELING MICROSCOPY

Scanning tunneling microscopy was invented by Binning and Rohrer in 1982. [19] Today it is a well established surface science technique that has resolved numerous static sample systems in chemistry, biology, and physics. Due to its high spatial resolution, single atomic sites can be detected and characterized. This high spatial resolution in real space is beyond the limits of integrating surface science methods.

With STM, conductive solid surfaces can be investigated. Figure 3.1a shows the schematic arrangement of the metallic STM tip and the atomically flat substrate underneath. The metal tip is ideally atomically sharp with a single atom occupying the lowest position, as marked in purple in Figure 3.1a. When the distance between the tip and the substrate is reduced to approximately 5 Å and the bias voltage V_S is applied between tip and sample, a current in the range of a few nanoamperes is detected. The current flows before the tip touches the sample surface due to the quantum mechanical effect of tunneling electrons. The small distance between tip and sample causes the wave function of the electrons in the tunneling junction to be nonzero. This permits electrons to cross the barrier, as indicated by the black horizontal arrows in Figure 3.1b. If the bias voltage applied to the tip is negative, the Fermi level E_F of the tip shifts upwards. The electrons in the filled states of the tip cross the barrier and occupy empty states of the sample, marked with the gray area in Figure 3.1b. The polarity of the bias voltage influences the direction of electron tunneling.

The quantum tunneling effect is sensitive to the local densitiy of states (LDOS) of tip and sample and to the tip-sample distance. By scanning the tip across the surface, the sample can be probed in real space. From the measured tunneling current and the tip height, the surface topography can be determined.

STM can be operated in constant current and in constant height mode. The constant current mode is mostly used in conventional STM. In this mode, the tip-sample distance is adjusted by an electronic feedback loop to obtain a constant tunneling current. In Figure 3.2a

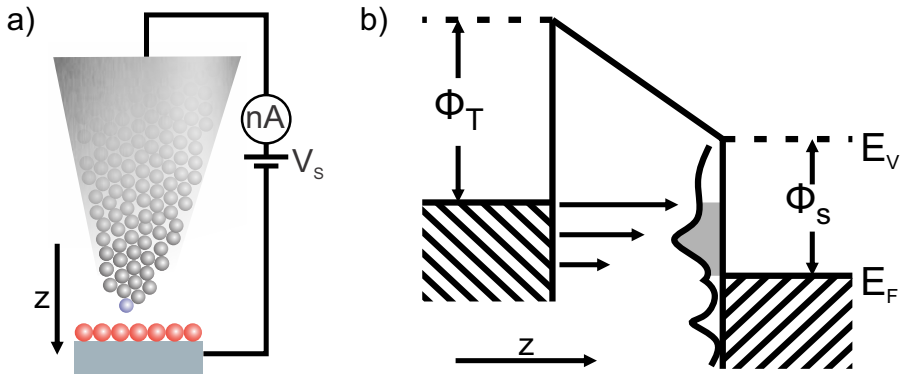

Figure 3.1: Schematic working principle of STM. a) Atomically sharp metal tip close to the atomically flat substrate. b) Schematic energy levels and LDOS at the quantum tunneling junction. Respective vacuum levels E_V are drawn with dotted lines, Fermi levels E_F with solid lines, and the respective work functions ϕ_T, ϕ_S are assigned. Adapted from Ref. [92]

the tip height z is controlled while the tunneling current I_T is constant. The result of a constant current scan is an image that relies on the tip height as a function of the lateral spatial coordinates. In addition to the high lateral resolution, the constant current image exhibits a high vertical resolution.

The second common STM mode scans with constant tip height z, as illustrated in Figure 3.2b. The changes in the tunneling current provide the image contrast, where the logarithm of the tunneling current can be related to the surface topography. Due to this non-linear dependence of tunneling current and tip height, the vertical resolution is not as high as in the constant current mode. However, measuring at constant height mode has the great advantage that the electronic feedback loop to control the tip height can be neglected.

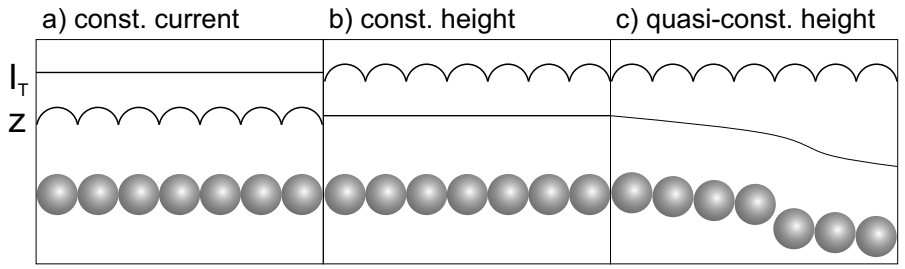

Figure 3.2: Schematic of STM modes. a) In constant current mode, the tip height z is adjusted by an internal electronic feedback loop to keep the tunneling current I_T constant. b) In constant height mode, the tip height is not altered and the tunneling current signal carries all information to construct the STM image. c) In quasi-constant height mode, the tip height is adjusted with an intentionally very slow feedback loop to avoid tip crashes due to thermal drift or slowly changing topography. Partly adapted from Ref. [93].

When scanning in constant height mode, the tilt between the sample surface and the plane of tip propagation must be corrected to avoid tip crashes. For measurements over several minutes thermal drifts and other artifacts can lead to unwanted crashes of the scanning tip into the sample surface. To avoid these crashes, a slow electronic feedback loop can be used. This feedback compensates only for slow motions in the vertical direction, as schematically shown in Figure 3.2c. This mode with slow feedback parameters is referred to as quasi-constant height mode. [9]

3.2 HIGH-SPEED STM

The advantages of high scan speeds in STM are well known since the 1980s. [26] Unfortunately, high scan speeds are not achieved very easily in conventional STMs. The scan speed and therefore the frame rate is limited by several factors. More than in conventional STM, a compact and rigid mechanical design is crucial that exhibits high mechanical resonance frequencies. Different approaches are reported that lead to increased scan speeds. They include the optimization of the mechanical design of the STM, especially increasing mechanical resonance frequencies. [2, 30, 35, 94–102] The other main important limitations are 1) the electronic feedback loop, 2) the hardware and software for the data acquisition, and 3) the scan geometry.

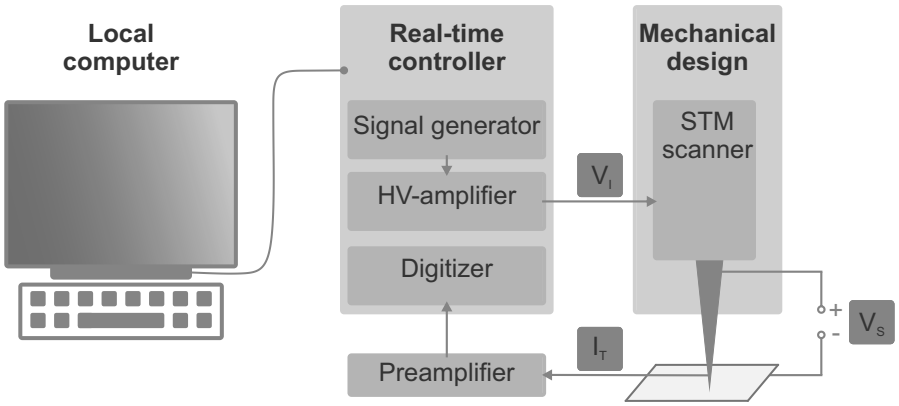

Figure 3.3: Schematic of STM design. Scan parameters are set using a local computer that has access to the real-time controller unit. The STM scanner is driven with the voltage input signals V_I. The tunneling current I_T is amplified and digitized. V_S is the potential difference between STM tip and sample. Adapted from Ref. [9] licensed under a Creative Commons Attribution (CC BY) license.

Figure 3.3 and Table 3.1 help to identify the individual limiting components. Conventionally, the STM is operated by the user from a local computer. This computer communicates with the real-time controller of the scan hardware. Within this real-time controller unit, generators and amplifiers for the voltage input signals V_I are included.

Table 3.1: Bandwidths of commercial hardware components that are suitable for high-speed applications. Compared to the electron tunneling limit. Table adapted from Ref. [9] licensed under a Creative Commons Attribution (CC BY) license.

Electronics	Bandwidth (Hz)	Time constant (s)	Ref.
Electron tunneling	3 G (1 nA)	0.33 n	[100]
Real-time controller	30 k	33 μ	[103]
Preamplifier	600 k (10^9 V/A)	1.7 μ	[104]
Digitizer	250 M	4 n	[105]
HV amplifier	5 M	200 n	[106]

The signals are converted to lateral displacements of the STM scanner by typically piezo ceramic elements. The resulting tunneling current I_T is amplified by the preamplifier. In the digitizing unit, the analog tunneling current signal is converted to a digital signal that is used to reconstruct the final STM image and serves as the input signal for the electronic feedback loop.

Every single step in this process has its own limitations owed to the physical constraints of the individual hardware and software components. Typical bandwidths of these components are listed in Table 3.1. They are addressed in the following sections.

3.2.1 *Limitation: Electronic Feedback*

Looking at the physical limitations of each component in Table 3.1 it becomes obvious that the real time controller and the preamplifier exhibit the lowest bandwidths.

Some approaches exist to increase the scan speed using constant current mode. [30, 95, 96] However, since the mechanical resonances are quickly lower than the time constant of the feedback loop, most often the constant height mode is applied to increase the scan speed. [31, 33, 36] As mentioned in Section 3.1, the constant height mode does not require a fast feedback loop. Other approaches to adjust the feedback loops for fast scans include the so-called hybrid mode that generates images based on both, the tip height and the error of the tip height. Furthermore a mechanical separation of the fast and the slow scan is possible by running two independent feedback loops. [30, 95]

According to Table 3.1, in all scanning modes, the next important limiting component is the preamplifier. The bandwidth of the pream-

plifier determines the signal to noise ratio of the measured tunneling current. High bandwidth preamplifiers are commercially available, as listed in Table 3.1, for instance. In the literature various approaches are reported that use sophisticated preamplifiers to increase the scan speed in STM. [33, 35, 36, 95, 107–109]

When the scan speed exceeds the preamplifier cut-off frequency, the acquired data points must be oversampled. [33] Oversampling and the closely related topic of data acquisition will be discussed in Section 3.2.2.

3.2.2 *Limitation: Data Acquisition*

For high image rates and to guarantee sufficient data oversampling, the data acquisition must be designed for high-speed applications. Although some commercial STM control units are equipped with digital input channels with data sampling rates of up to 200 MHz, [103] conventionally STM hardware does in general not support high-speed measurements. Furthermore, the analog signal from the preamplifier must be converted to a digital signal prior to data acquisition.

Custom programmed hardware digitizer units can exceed sampling rates of 250 MHz. For oversampling and reading the data from the digitizer, fast calculations are necessary that require high processing speeds in realtime. For example, acquiring 200×200 pixel images with 100 Hz and and 16 bit resolution results in data streams of more than 64 Mbit s^{-1}. [36] The factor for data oversampling must be added to this calculation, which then results in data streams that easily exceed 200 Mbit s^{-1}.

Furthermore, high-speed STM measurements ask for sophisticated designs for data storage and data visualization during the scan. For data storage, data loss must be avoided. [36] Therefore, separated processes to store the data and to display the data, are recommended. [2]

The possibility to record over longer times exceeding minutes or hours at constantly high frame rates seems advantageous to capture statistically occurring dynamic processes.

In addition, the acquired signal must be synchronized and labeled correctly to allow for correct assignment. This is especially true if more than one signal is recorded. For instance, the simultaneous acquisition of the tunneling current and the tip height position is useful. If the spatial coordinates of the tip position are monitored, in contrast to conventional STM data acquisition, the perfect synchronization of the individual input signals must be guaranteed to allow for correct image reconstructions. The latter point is especially important if the scan geometry differs from the conventional line-by-line raster method.

3.2.3 *Limitation: Scan Geometry*

In conventional STM images, the tip scans with a line-by-line motion across the surface. This scan geometry is owed to the easy representation of the data as 2D grid image. In fact, in every scanning microscopy technique, the line-by-line raster motion constitutes the conventional scan pattern.

At the same time, this line-by-line motion has great drawbacks. During one measuring cycle, the sample surface is scanned four times (forward, backward, upward, and donward scan), which slows the achievable frame rate down considerably. The input signals and the resulting lateral displacement consist of sharp triangular waveforms, as shown in Figure 3.4a. In SPM, these sharp points of inversion cause rapid changes of the tip propagation direction and of the tip velocity. Due to non-linear displacements and high inertia, these rapid changes, in turn, excite mechanical resonances in the system that lead to distortions in the acquired images. [44] The image distortions become very severe at increased scan speeds and can make atomic resolution impossible.

Therefore, alternative scan geometries are discussed for SPM applications. [38–47, 110] Figure 3.4 shows promising candidates that have been tested for AFM applications. [40, 41, 46, 47, 110–114]

All of these scan geometries avoid sharp points of inversion in the input signal. However, so far all high-speed STM measurements reported in literature are performed using the sinusoidal scan geometry, as evident from Figure 2.4. Most likely, the reason for this is the similar scan pattern compared to the triangular raster scan, which makes the signal generation and the image visualization easier. The drawbacks are inevitable image reconstructions and distortion corrections. [32, 33, 35, 99, 115]

From the side-by-side comparison in Figure 3.4 it becomes obvious that the spiral scans the real space faster than the sinusoidal and the Lissajous geometry. The spiral scan input signals consisting of sine and cosine waves exhibit lower frequencies compared to the other scan geometries. Considering these points, the spiral geometry is favored for high-speed scans. However, the data points along the spiral trajectory do not coincide with the 2D grid, as shown in Figure 3.4d. Therefore, the data representation constitutes major challenge for the implementation of spiral scan geometries. In Chapter 6 solutions for the data representation and further details of the spiral scan implementation are provided.

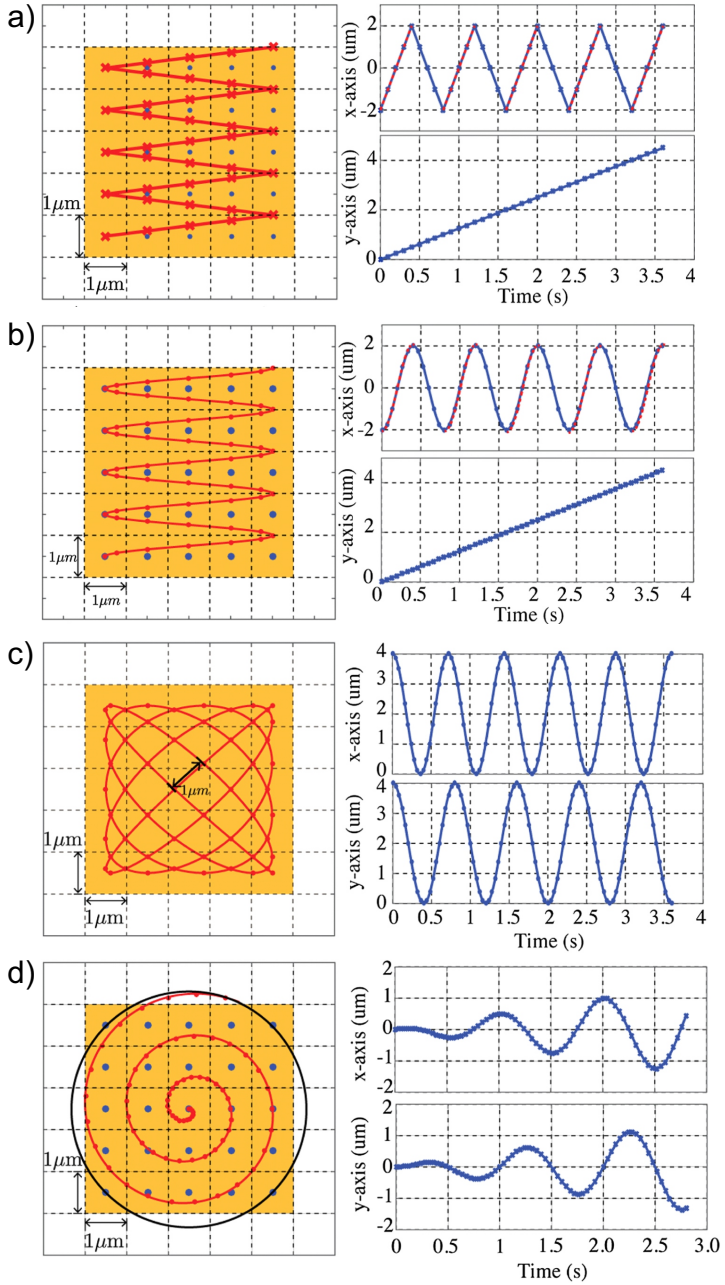

Figure 3.4: Overview of possible SPM scan geometries. The corresponding input signals are shown on the right. a) Conventional raster scan. b) Sinusoidal raster scan. c) Lissajous scan. d) Spiral scan. Adapted from [110]. Copyright 2016 Chinese Automatic Control Society and John Wiley & Sons Australia, Ltd.

4

PREPARATION CONDITIONS

In this section, the procedures for crystal cleaning, preparation of oxygen adlayers, and growing of ultrathin oxide films are described.

4.0.1 *Clean Single Crystals*

The single crystals are transferred to the UHV chamber system with a base pressure in the range of 10^{-9} to 10^{-10} mbar. The crystal surfaces are exposed to repeating cycles of Ar^+-ion bombardment, annealing at elevated temperatures for 1 to 5 min, and annealing in oxygen atmosphere (3×10^{-6} mbar) for 20 min. The annealing temperature depends on the single crystal material. Ru(0001) is annealed in UHV at 1300 to 1400 K. Au(111) is annealed in UHV at 800 K.

4.0.2 *Oxygen Adlayers on Ru(0001)*

Molecular oxygen is dosed on the clean Ru(0001) surface at pressures of approximately 2×10^{-6} mbar. The oxygen coverage depends on the exposure time. For low coverages as presented in Section 6.5 several tens of seconds are sufficient. For the O(2×1) phase, as presented in Section 7.2, the exposure time is 1 to 2 min at temperatures below 380 K. Another approach is to dose oxygen at elevated temperatures of 1200 to 1250 K for 10 min. Following this procedure, the 3O(2×2) structure results, which is shown in Sections 6.4, 6.3. The oxygen coverage can be adjusted subsequently by heating the sample shortly to elevated temperatures of 1200 K in UHV. The slightly reduced O(2×2) adlayer can be prepared in this manner, as shown in Section 7.1.

4.0.3 *Ultrathin Oxide Films on Ru(0001)*

After covering the clean Ru(0001) surface with the 3O(2×2) structure, silicon or germanium are evaporated with an oxygen back-pressure. The preparation procedures are similar and vary only slightly depending on the sample system. For clarity, they are described separately in the following:

For the preparation of silica films, silicon is evaporated from a solid rod in an oxygen atmosphere of 2.3×10^{-7} mbar at a constant ion flux of 15 nA and an applied voltage of 950 V. Subsequently, the sample is annealed in 2.2×10^{-6} mbar oxygen atmosphere at 1225 K for 15 min. The final cooling is performed in the same oxygen atmosphere.

For the preparation of germania films, germanium is evaporated from a crucible in an oxygen atmosphere of 2×10^{-6} mbar at a constant ion flux of 15 nA and an applied voltage of 900 V. Subsequently, the sample is annealed in 2×10^{-6} mbar oxygen atmosphere at 850 K for 10 min. The final cooling is performed in the same oxygen atmosphere.

Part III

DESIGN AND CONSTRUCTION

5 DESIGN OF MECHANICAL COMPONENTS

To resolve thermally activated dynamics, we combined the two fields of high-speed STM and variable-temperature STM. We developed a variable-temperature high-speed STM, that can track dynamic processes at the atomic scale on well defined surfaces.

This chapter starts with an overview of the UHV chamber system. Then, the sample holder, the cryostat and the STM design are explained in detail. In this chapter, the focus is on the mechanical properties. Most of the concepts presented in this chapter are published in Review of Scientific Instruments, Ref. [9].

5.1 ULTRAHIGH-VACUUM CHAMBER SYSTEM

The experimental data presented in this work was collected in a newly designed and assembled UHV chamber system. The system is designed for high-speed and variable-temperature STM measurements. The UHV-system consists of two chambers separated by a gate valve, as shown in Figure 5.1. The chambers are accessed with a manipulator (1). The manipulator head uses a SPECS tool with custom modifications to fit the custom designed sample holder. The sample holder is described in section 5.2. At the retracted position, the sample is located in the preparation chamber (2). This chamber is equipped with standard surface science preparation tools, such as a sputter gun, gas inlets, and an e-beam evaporator to clean samples and to prepare thin films. The LEED and auger electron spectroscopy (AES) setup enable surface characterization of single crystals, adsorbate layers, and thin films. The separately pumped load lock (3) enables a quick sample transfer from ambient environment to the sample storage (4) that can host up to eight sample holders in UHV. A gate valve connects the preparation chamber to the main chamber (5). At the extended position, the manipulator reaches the main chamber, where the STM is mounted. The STM is located inside a liquid flow cryostat (6). The cryostat, the transfer tube (7), and the can for liquid nitrogen/hydrogen (8) are presented in detail in Section 5.3.

To ensure base pressures in the 10^{-10} mbar range, the preparation chamber is equipped with a turbomolecular pump (9), while the main chamber is connected to an ion getter pump with integrated titanium sublimation pump (TSP) (10).

The commercial Nanonis hardware (11) for conventional STM measurements and the electronic control units (12) are located inside the frame to reduce external vibrations.

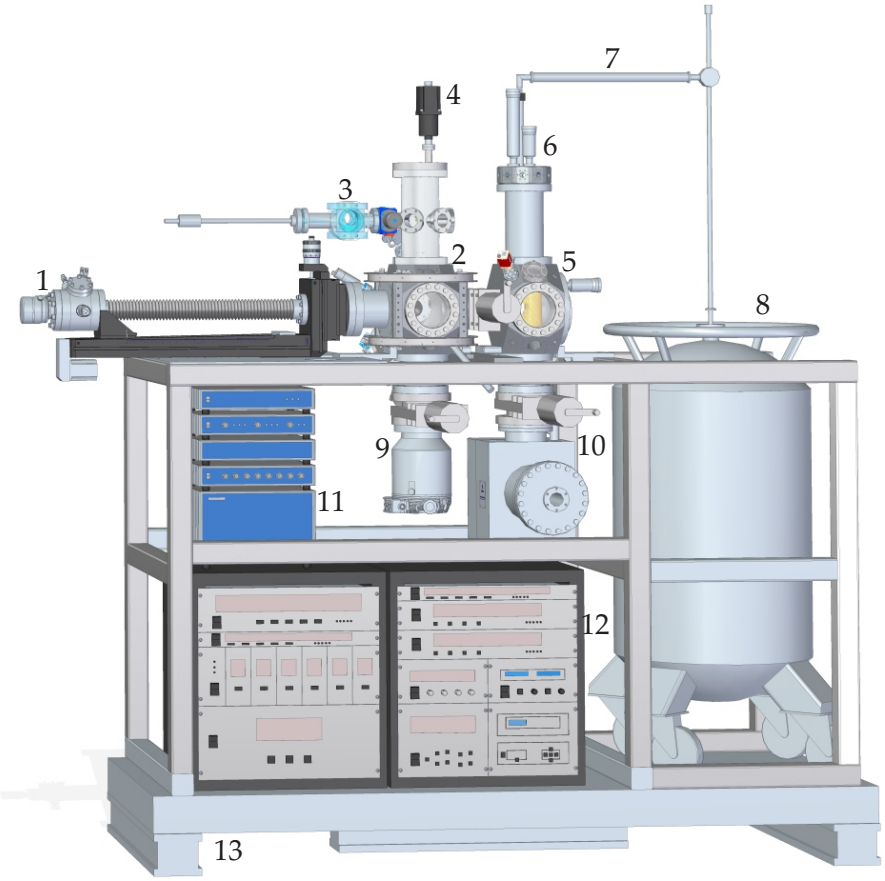

Figure 5.1: Scheme of the UHV chamber system, which was assembled and used in the experiments. (1) Manipulator for sample transfer. (2) Chamber for sample preparation and characterization. (3) Load lock to introduce samples to UHV. (4) Rotary feed through to move the sample storage. (5) UHV chamber that hosts the STM inside a (6) liquid flow cryostat. (7) transfer tube for the liquid nitrogen (LN_2) to the cryostat. (8) LN_2 or liquid helium (LHe) can, respectively. (9) Turbomolecular pump. (10) Ion getter pump. (11) Nanonis control unit for slow STM scans. (12) Electronic hardware to control the surface science tools. (13) Opta optical breadboard supported on three vibrational dampers. Based on Ref. [9] licensed under a Creative Commons Attribution (CC BY) license.

The electronic hardware for high-speed scans is located on a separate rack.

The two chambers are mounted on a rigid metal frame that is placed on an Opta optical breadboard. The breadboard is supported by three active damping legs (13) that keep the entire setup mechanically stable.

5.2 SAMPLE HOLDER DESIGN

The sample holder is custom designed. As for the entire setup, two main aspects are considered in the design: the high-speed scans and

the variable temperature measurements. The high-speed aspect asks for a mechanically stable sample holder. To ensure a good vibrational behavior and to reduce thermal drifts, the design is rigid, compact and radial symmetric as shown in Figure 5.2.

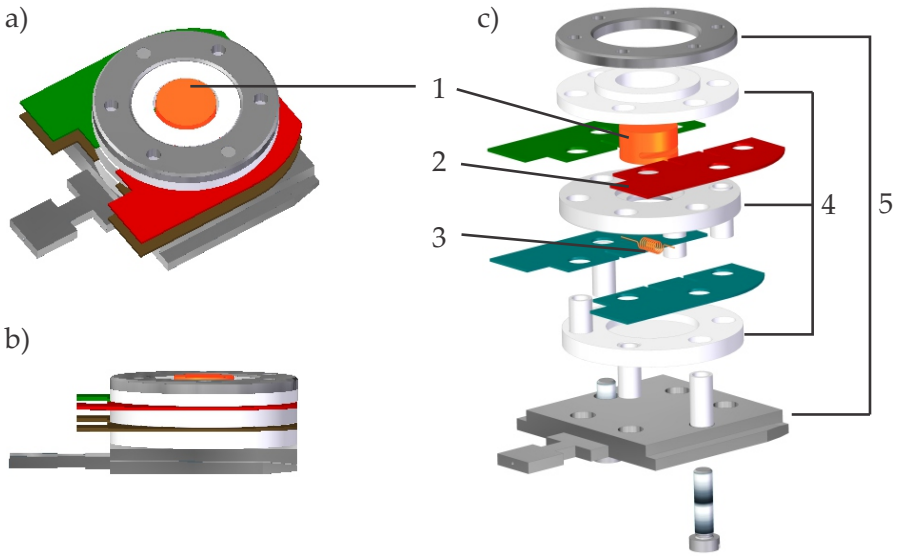

Figure 5.2: Scheme of the custom designed sample holder. a) Diagonal top view and (b) side view of the assembled sample holder. b) Exploded view of the sample holder. (1) Single crystal with notches at the sides for support. (2) K-type thermocouple plates. (3) Tungsten filament and Mo plates. (4) Al_2O_3 ceramics as electrical isolation layers. (5) Mo ring and base plate to fix the sample holder with the Mo screws and the Al_2O_3 tubes. Based on Ref. [9] licensed under a Creative Commons Attribution (CC BY) license.

The variable temperature application asks for a reliable control of the sample temperature inside the microscope. The sample (1) is connected to K-type thermal couple plates (2) that ensure precise temperature reading. For heating inside and outside of the STM, an electron bombardment heating is integrated inside the sample holder. The thin tungsten filament (3) and the connected molybdenum plates are electrically decoupled from the sample by alumina spacers and alumina tubes (4). Also the molybdenum ring and the base plate that clamp the stacked design with Mo screws are electrically decoupled from the sample and the filament. During electron bombardment heating, the sample is grounded and the filament is set to a lower potential while a current is applied. The emitted electrons heat the sample from the back to temperatures above 1500 K.

The filament and the thermocouple plates enable the electrical connections between sample holder and manipulator (1), as illustrated in Figure 5.3. An insulating macor piece in the manipulator head decouples the sample holder from the UHV chamber. After sample preparation and characterization, the sample holder can be transferred

to the sample storage (2) or directly to the STM, which is located in the continuous flow cryostat (3).

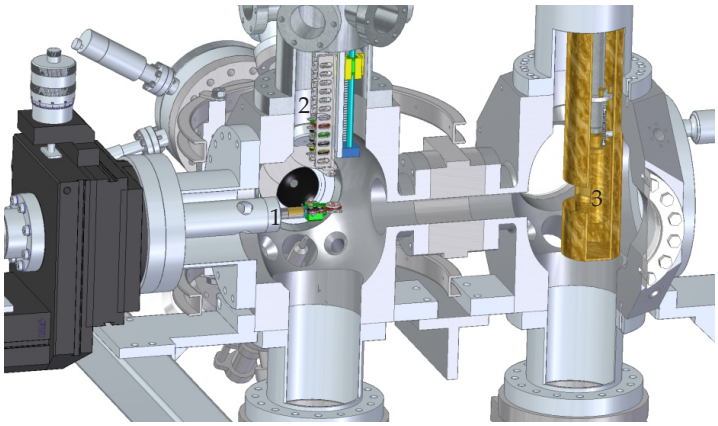

Figure 5.3: Insight to UHV chamber and sample transfer system. (1) Load Lock. (2) Sample storage. (3) Manipulator. (4) Cryostat shields with STM inside. Based on Ref. [9] licensed under a Creative Commons Attribution (CC BY) license.

5.3 CONTINUOUS FLOW CRYOSTAT

The liquid flow cryostat enables measurements at cryogenic temperatures on the one hand and can be used to counter-cool the STM body during high temperature measurements on the other hand. For STM measurements at elevated temperatures, the scanner must be counter-cooled to avoid thermal drift and to guarantee that the piezos are not heated too high with respect to their Curie temperature. The liquid flow cryostat is cooled via a transfer tube, which is connected to the liquid nitrogen or liquid helium can, as shown in Figure 5.1. The other end of the transfer tube is connected to the liquid inlet (1) in Figure 5.4a). A membrane pump at the exhaust line operates in the range of hundreds of mbar and regulates the constant gas flow through the cryostat. The shutter regulation (2) in Figure 5.4 enables convenient sample transfers in the open shutter position and a well isolated environment for measurements at the closed shutter position. The thermal connection to the STM unit can be adjusted with the clamping regulation (3). All electrical connections for heating, temperature reading, and STM measurements are fed through at the top of the cryostat (4). Surrounded by the outer (5) and inner cryostat shield (6), the microscope unit (7) is decoupled from the room temperature environment.

Figure 5.4b) shows the magnified microscope unit. The entire unit can be mechanically decoupled from the cryostat by releasing it to three springs (8). The decoupling affects also the temperature coupling to the cold finger (9) and can be used to isolate the microscope from

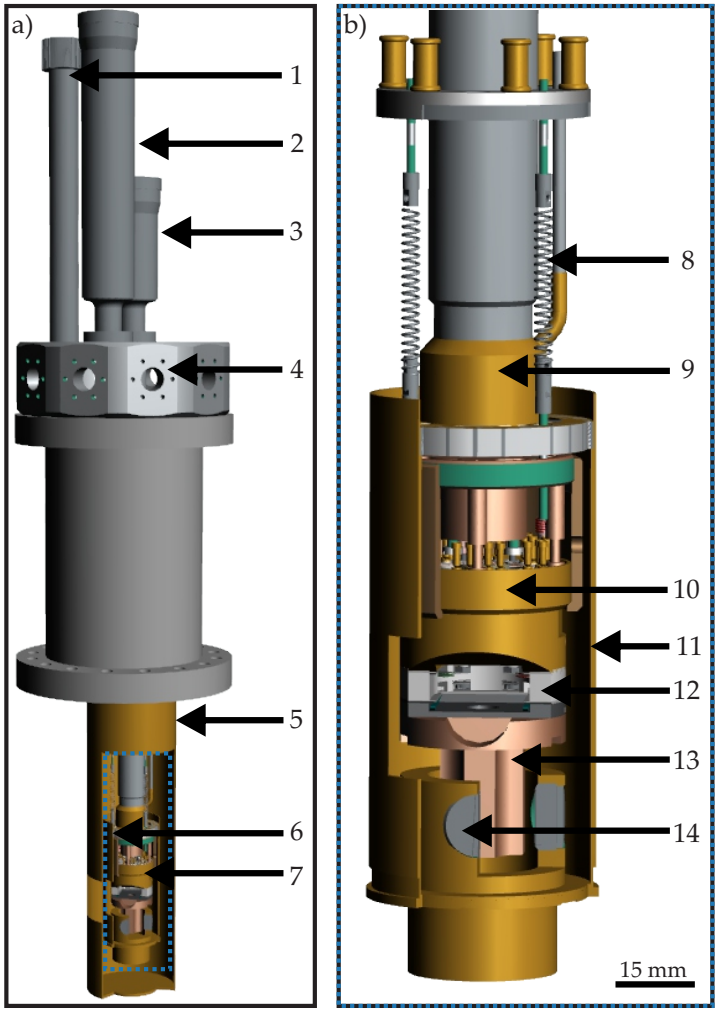

Figure 5.4: Cryostat design. a) Continuous flow cryostat: (1) liquid inlet, (2) shutter regulation, (3) clamping regulation, (4) ports for vacuum feedthroughs, (5) outer cryostat shield, (6) inner cryostat shield, and (7) microscope unit marked in blue. b) Magnified microscope unit: (8) custom springs for mechanical decoupling, (9) cold finger, (10) microscope body, (11) inner cryostat shield, (12) sample holder stage, (13) copper cross, and (14) magnets for eddy current damping. Adapted from Ref. [9] licensed under a Creative Commons Attribution (CC BY) license.

the surrounding. Clamping the microscope unit results in fast cooling behavior.

5.4 STM HEAD AND HYBRID SCANNER

For low noise levels during STM measurements, the microscope unit is unclamped. Figure 5.5a) shows the individual parts of the unit in an exploded view. The STM head (2) and the sample stage (3) are tightly connected to avoid lateral drifts during measurements. The

eddy current damping reduces mechanical vibrations and consists of of a copper cross (4) and four aligned magnets (5).

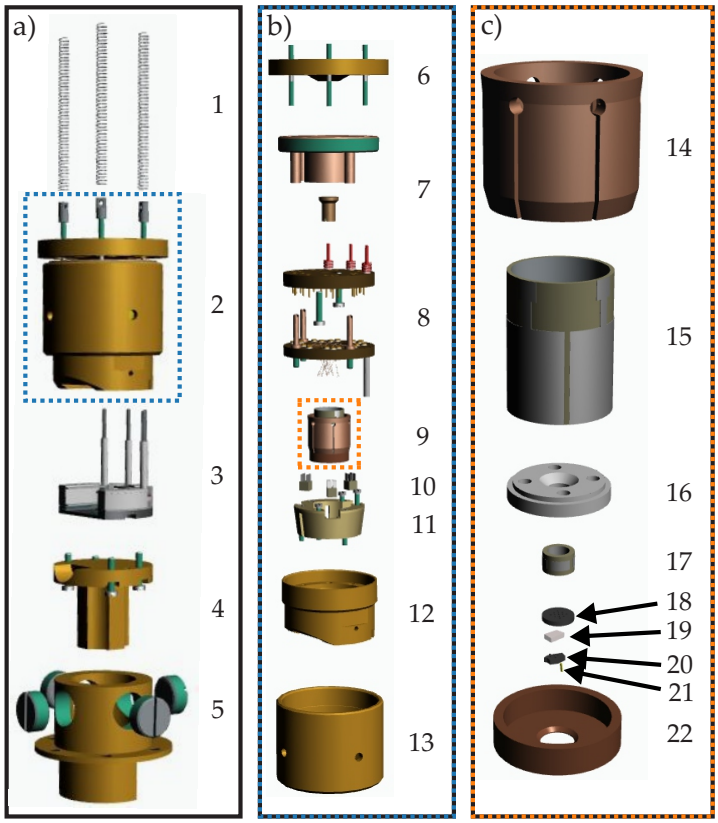

Figure 5.5: Setup of the microscope unit. a) Exploded view of microscope unit: (1) springs, (2) STM head, (3) sample holder stage, (4) copper cross and (5) magnets for eddy current damping. b) Exploded view of STM head: (6) connection to cryostat, (7) clamping mechanism, (8) electrical connections, (9) scanner unit, (10) shear piezos for stick-slip coarse approach, (11) copper block to support shear piezos with adjustable tension, (12) lower and (13) outer microscope body parts. c) Exploded view of scanner unit: (14) copper walker with vertical slits for increased elasticity, (15) overview (OV) piezo, (16) macor disk for mechanical connection and electrical isolation, (17) fast-scan (FS) piezo, (18) graphite plate, (19) insulation spacer, (20) graphite plate to support the STM tip (21), and (22) copper shield for electrical shielding of scan signals. Adapted from Ref. [9] licensed under a Creative Commons Attribution (CC BY) license.

Figure 5.5b) shows that the scanner unit (9) is supported by three shear stack piezos (10) mounted in a copper block (11). This design is based on the Pan-STM [97] and allows for precise coarse approaches using the stick-slip motion. In addition, the scanner unit is rotatable due to its cylindrical shape. The detailed components of the scanner unit are shown in Figure 5.5c). The copper cylinder (14) has six vertical slits transforming it to an elastic component that clamps itself in

between the shear stack piezos. At the bottom of the tube piezo ceramic arrangement (15, 16, 17), several layers (18, 19, 20) shield the Pt-Ir tip (21) from other electronic signals. Placing the tip off-center and using the rotation of the scanner unit enables to change the scan region on the macroscopic scale. For additional electric shielding and to avoid cross talk, a copper cap (22) covers the lower segment of the scanner unit.

All metal components are manufactured from oxygen-free copper. Using the same material guarantees similar thermal expansions of the single components and therefore the microscope can operate within a wide temperature range. For heating the sample inside the microscope, similar contact plates are used as in the manipulator design described in Section 5.2. The contact plates (5) are located at the back of the sample holder stage, as shown in Figure 5.6. For mechanical stability, the sample holder is clamped by Mo springs (6).

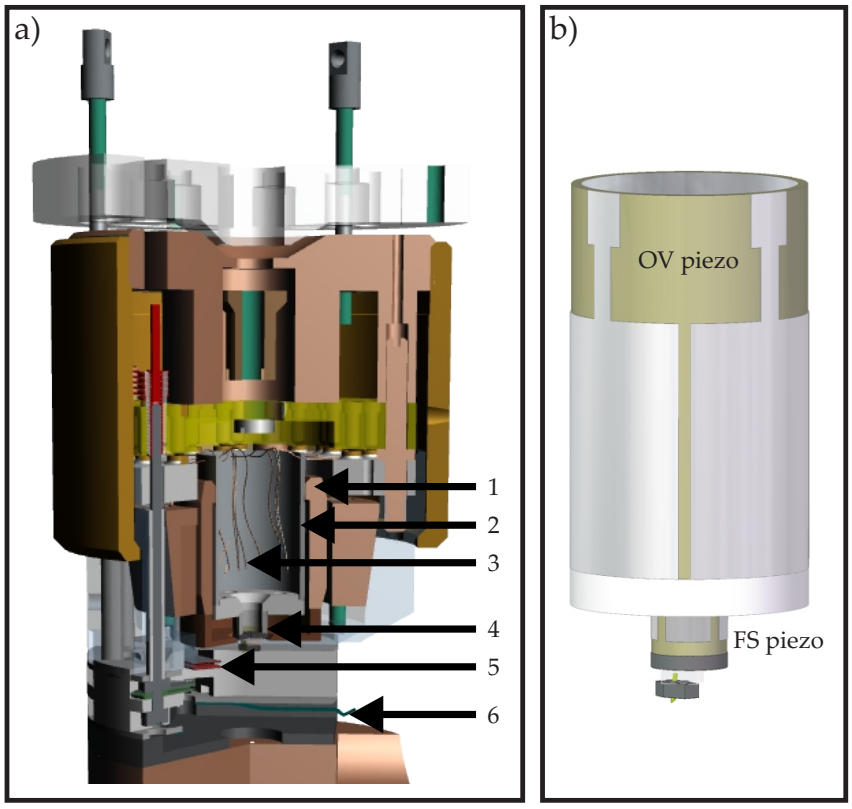

Figure 5.6: Microscope design. a) Section view of microscope unit: (1) copper walker, (2) OV tube piezo, (3) thin copper cables, (4) FS tube piezo, (5) electrical connections for thermocouple and filament of the sample holder, and (6) Mo springs to clamp sample holder. b) Hybrid scanner consisting of the OV piezo and the FS piezo. Adapted from Ref. [9] licensed under a Creative Commons Attribution (CC BY) license.

To ensure the mechanical stability of the scanner unit, the components are densely arranged with solid mechanical connections inside the STM head, as shown in Figure 5.6.

The heart of the scanner unit is the self built hybrid scanner. The hybrid scanner consists of two independently operating tube piezos. For large scale images, the OV piezo is used, which has a scan range of 2500×2500 nm^2 at ± 200 V and 300 K. High-speed measurements are realized with the FS piezo, which has a range of 500×500 nm^2 and a resonance frequency above 1 MHz. The FS piezo is attached to the bottom of the OV piezo with an electrical isolation spacer, as shown in Figure 5.6b. Both piezos are aligned precisely with respect to their four segmented electrodes to ensure that they elongate laterally in the same directions. Isolated cables for the four segments of the tube piezo and its inner electrode are fed through the overview piezo, as shown in Figure 5.6. The five electrical connections for the FS piezo and the OV piezo are separated to enable independent control.

6 HIGH-SPEED SETUP

In this chapter, the experimental setup to perform high-speed STM measurements is presented. The working principles of the high-speed scan control, the data acquisition, and the live display are explained. For all of these tasks, the high-speed electronic hardware is introduced. In this context, the software solutions for the high-speed scan input signal generation, data acquisition, and data visualization are demonstrated. Most of the concepts presented and several of the figures shown in this chapter are published in Applied Physics Letter in Ref. [59].

6.1 SCAN CONTROL

The two tube piezos OV piezo and FS piezo can be controlled independently. The schematic overview of the scan control is provided in Figure 6.1. The OV piezo is controlled with the conventional Nanonis hardware and software while the FS piezo is controlled by custom programmed high-speed electronics. The High-speed electronics for control, monitoring, and data acquisition are integrated into the experimental physics and industrial control system (EPICS) framework. [116]

The hybrid scanner design allows to measure overview images and to locate the STM tip based on this image at the desired position to perform high-speed scans. The high-speed scan starts immediately without tip retraction and the tip scans in quasi-constant height mode. In this mode, the Nanonis unit controls the tip height with feedback parameters that are slower than the acquisition time of the high-speed scan images. Due to the independent control of the two piezos, the tip position can be adjusted while high-speed scans are performed. The resulting shift of the scan area can be observed in real time thanks to the live display, which is described in Section 6.5. In Figure 6.2, the Phoebus [117] user interface shows an exemplarily live display of a spiral scan on the Au(111) surface. More details about this scan are provided in Figure 6.5.

The heart of the scan control is the arbitrary waveform generator (V375 from Highland Technology) that is mounted inside a Versa Module Eurocard-bus (VMEbus) rack. On the waveform generator, four arbitrary waveforms can be defined that can be represented as individual 1D 16-bit arrays. The user sets parameters within the EPICS framework via the Phoebus [117] interface, which is shown in Figure 6.2. With the parameter settings, the user defines the input signals,

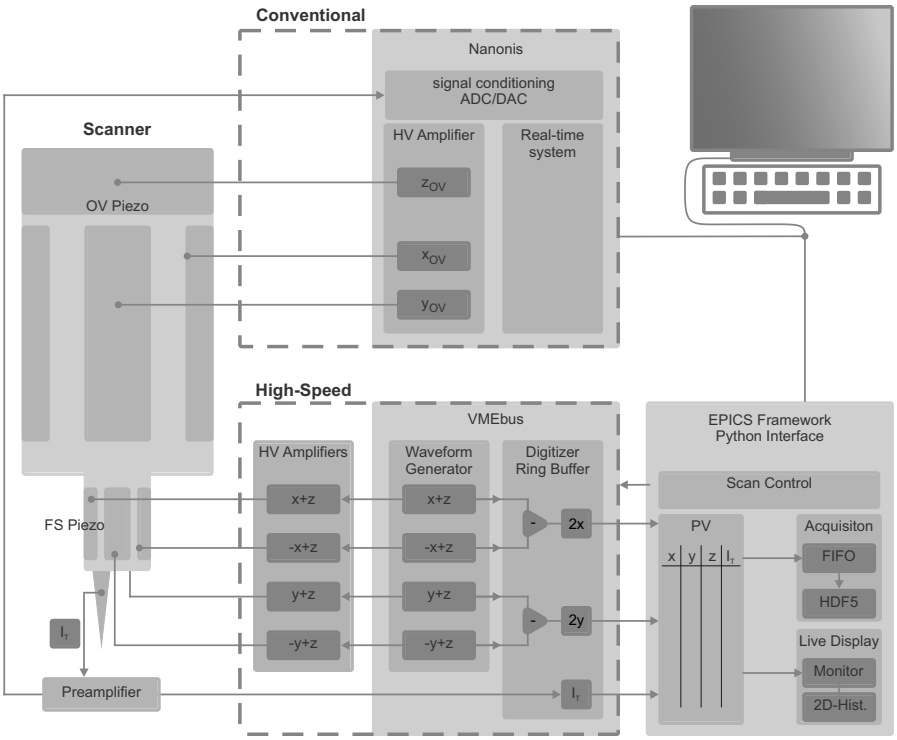

Figure 6.1: Schematic scan control of both conventional and fast STM measurements. The local computer communicates with both the conventional unit and the high-speed unit. The communication to the high-speed unit is realized within the EPICS framework using python interfaces. Adapted from Ref. [9] licensed under a Creative Commons Attribution (CC BY) license.

the scan speed, and the scan range. The scan range is controlled by the voltage amplification inside the waveform generator that acts as digital-to-analog converter (DAC). The maximum output voltage of the waveform generator is limited within the EPICS framework to avoid overvoltages. With the maximum voltage range of ± 3 V, the input signals are amplified with a factor of 50 by four identical HV amplifiers (WMA-300 from Falco Systems). The amplified signals are applied to the outer electrodes of the FS piezo.

The scan geometry of the piezo can be tuned with the waveforms input signals and unconventional scan patterns that favor high-speed measurements can be generated. Details of the unconventional and very customizable spiral scan signal are described in Section 6.3.

6.2 DATA ACQUISITION

For data acquisition, a digitizer is integrated in the VMEbus system running EPICS on a real time executive for multiprocessor systems (RTEMS) [118]. The Struck SIS3316 digitizer acquires up to 250 megasamples per second per channel with 14-bit resolution. Four input channels

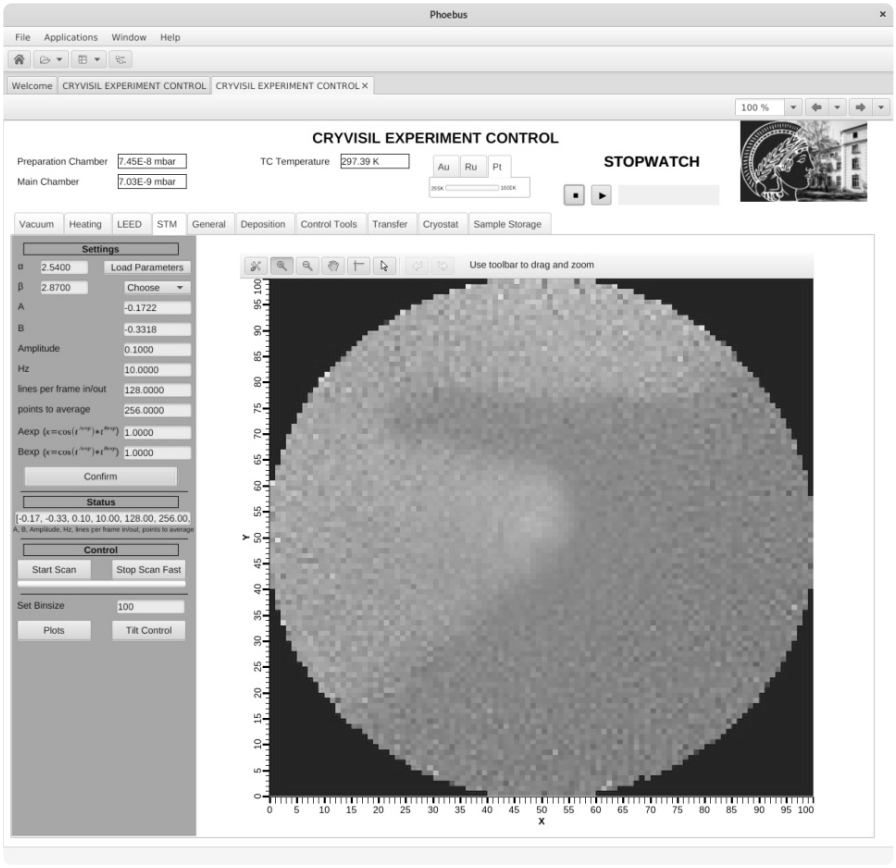

Figure 6.2: User interface to perform high-speed STM measurements. The user interface is realized with Phoebus. [117] On the left, scan parameters for the high-speed scan can be set. The exemplary spiral STM image on the right shows the Au(111) surface, described in more detail in Figure 6.5.

acquire the voltage input signals from the waveform generator. From these four signals the internal central processing unit (CPU) calculates the spatial coordinates that directly relate to the lateral displacement of the FS piezo. Two other digitizer channels read the z position of the OV piezo and the pre-amplified tunneling current I_T. The tunneling current is split between conventional and high-speed electronics to enable quasi-constant height measurements and to switch between high-speed and conventional scan instantaneously. Trigger signals serve as communication for starting and ending frames between waveform generator and digitizer. The trigger causes a sequence of actions inside the digitizing unit: i) The collected spatial coordinates are processed to extract the lateral displacement as indicated in Figure 6.1. ii) The data ($2x$, $2y$, z, I_T) is locally stored in a ring buffer. iii) The data is written to a process variable (PV) provided within the EPICS framework. The python interface for EPICS pvapy [119] is used for the PV-server and the data storage routine. The PV-server that handles the data chunks as ndarrays [120] runs on a Unix-System.

Various users within the network can access the data from the provided PV independently. By default, one thread provides a queue to temporally buffer the data on a local computer. A PV monitor acquires the data and writes the data chunks into the queue, as outlined by the following code snippet written in python. [1]

```
import numpy as np
import queue
import pvaccess as pva

q = queue.Queue(1000000)

def callback(x):
"""Collect data."""
        global q

        if not q.full():
                q.put(x)

        return q

channel = pva.Channel("High_Speed_PV")
channel.setMonitorMaxQueueLength(-1)
channel.subscribe("callback", callback)
```

In parallel, a consumer thread collects the queue data in chronological order and creates an hierarchical data format version 5 (HDF5) file as illustrated by the following python code snippet. [1]

```
        import numpy as np
        import h5py
        import threading
        import queue
        import time

hf = h5py.File(filename, 'a')

class ConsumerThread(threading.Thread):

        def __init__(self):
                super(ConsumerThread, self).__init__()
                self._stop_event = threading.Event()

        def stop(self):
```

1 The code snippets are outlines that have been simplified for better comprehension.

```
16                 self._stop_event.set()
17
18         def run(self):
19                 global q
20                 while True:
21                         if not q.empty():
22                                 x = q.get()
23                                 data = np.dstack((x, y, z, I)
24                                 ).squeeze()
25                         dset = hf.create_dataset(
26                                 f"{time.time_ns()}", data=data)
27                         q.task_done()
28
29 c = ConsumerThread()
30 c.daemon = True
31 c.start()
32
33 # Once the measurement stops:
34
35 q.join() # waits for thread to finish
36 hf.close()
37 c.stop()
```

This file contains all data to reconstruct the high-speed scan image: tunneling current, spatial coordinates, and real time timestamps. In addition meta data information are stored, such as the ideal waveform signal from the waveform generator, all parameters that define the scan, and the unix timestamp when every single data chunk was stored. This unix timestamp is different from the real time timestamp from the real time operating system RTEMS of the digitizing unit. For image processing and data analysis, the real time time stamp is used. Since, in contrast to commercial scan file types, the read back values from positional coordinates are saved in addition to the ideal input-waveform signals, arbitrary scan patterns can be processed and analyzed. This feature is important for unconventional scan patterns that are described in Section 6.3.

6.3 SPIRAL SCAN PATTERN

The frame rate in conventional STM is limited by its line-by-line raster motion. Figures 6.3a and b show the tip trajectory and the input signals for conventional raster scans. For visualization, the tip trajectories are shown schematically with a reduced number of data acquisition points. The points are represented by color coded triangles that indicate the scan direction. As obvious from Figures 6.3a and b, the raster scan consists of sharp triangular input signals. These sharp points of

inversion result in image distortions at high scan speeds. At the end of every scanning line, the tip must travel back to start the next line scan. Hence, the data is acquired discontinuously and one measurement cycle consists of forward, backward, downward, and upward scan. The surface is scanned four times with alternating tip propagation directions.

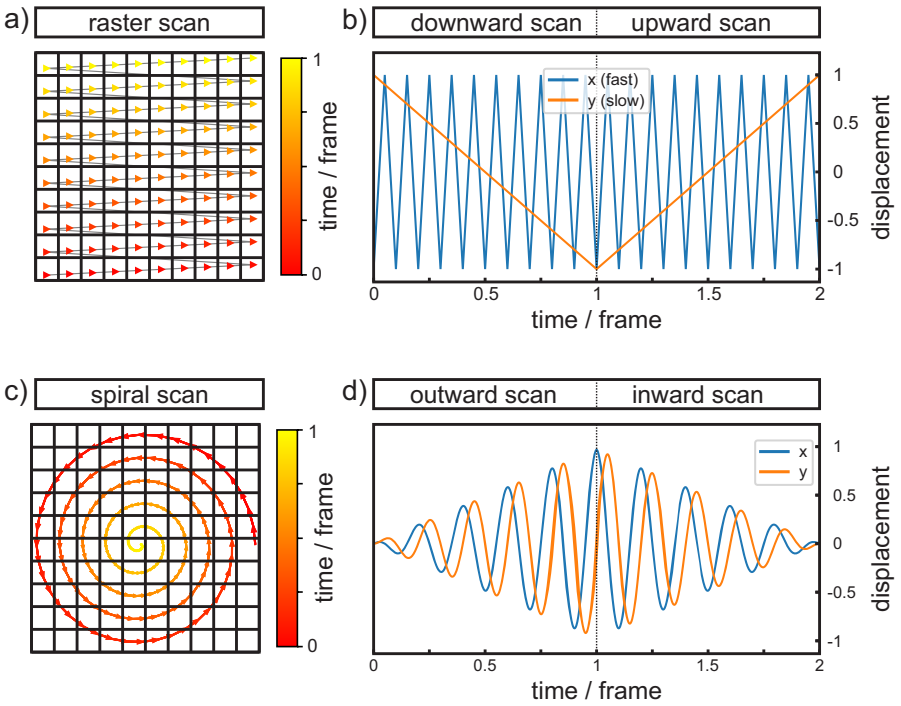

Figure 6.3: Schematic raster and spiral scan signals. a) Conventional raster scan pattern. Triangles represent data sampling points and indicate the scan direction. The color code is shown on the right and indicates the scan time. b) Lateral displacement of the scanning tip as a function of time. In analogy, c) and d) show the schematic spiral pattern and the lateral displacement, respectively. adapted from Ref. [59] licensed under a Creative Commons Attribution (CC BY) license.

To increase the frame rate of STM measurements, i) the input signal for the piezo movement must be smooth, ii) the real space must be scanned efficiently, and iii) the time per measurement cycle must be reduced.

As discussed in Section 3.2.3, spiral geometries, as shown in Figures 6.3c and d, are promising candidates to overcome the speed limitations set by STM scan patterns.

Spiral scans satisfy all of the above requirements: i) The input signals are smooth because spirals consist of a combination of two sine and cosine functions. ii) Spirals scan the real space without crossing of lines and iii) the scan direction of the tip is continuous, which produces images of similar contrast and, therefore, reduces the time per measurement cycle.

To visualize the data in this section, the 2D-histogram is used, which maps the data points on the 2D grid as indicated in Section 6.4. More details on image reconstruction are provided in Figure 6.8.

Various mathematical expression exist to describe spiral patterns. In the present study, Cartesian coordinates are used because they serve as amplitude of the voltage input signal and directly relate to the lateral tip displacement. To generate the input signals, the following equations are used for x and y:

$$x = t^a \cdot \cos\left(\omega \cdot t^b\right) \tag{6.1}$$

$$y = t^a \cdot \sin\left(\omega \cdot t^b\right) \tag{6.2}$$

Parameter a changes the amplitude over the time t and b adjusts the data point density along the trajectory. ω is the frequency of the sine and cosine functions and adjusts the line density of the spiral geometry. The line density can also be expressed in the distance of two neighbored lines (pitch size) or the number of rotations of the tip per frame. If ω increases, the scan speed increases, too, while the frame rate remains unchanged. At a given ω, the tip velocity and the spiral geometry are tuned with parameters a and b. Spiral geometries can be tuned, for instance to Archimedean or Fermat spirals and tip velocities can be varied from e.g. constant angular velocity (CAV) to constant linear velocity (CLV). Furthermore, intermediate geometries and modes are possible by changing a and b by smaller increments.

To implement the signals to STM measurements in quasi-constant height mode, the tilt of the sample surface with respect to the STM tip must be compensated. This compensation is independent of the type of spiral trajectory. For visualization, Figure 6.4a illustrates the tilting by the angle α in the x-direction. To correct the tilt in both x- and y-direction (α and β), the additional z signal is applied to all four outer electrodes of the FS piezo, as given in equation 6.3:

$$z = \tan(\alpha) \cdot 2x + \tan(\beta) \cdot 2y \tag{6.3}$$

This dynamic offset results in no lateral displacement but in height differenced of the piezo. In Figure 6.4 the displacements in x-, y-, and z-direction are plotted for the outward scan of the CAV Archimedean Scan. The amplitudes increase linearly over time. $2x$ and $2y$ are phase shifted by 90°. For the shown case, the tilt angles α and β are the same. Therefore, z is phase shifted by 45°. For visualization, the displacement in z is scaled arbitrarily.

The spiral geometry is applied in scans on the Au(111) surface in ambient conditions. A wide range of scan speeds and frame rates is tested and compared to conventional raster scans of characteristic step edge formations. The slow raster scan images are shown in Figures 6.5a-c and are acquired in 130 s. The lower row of Figure 6.5 shows

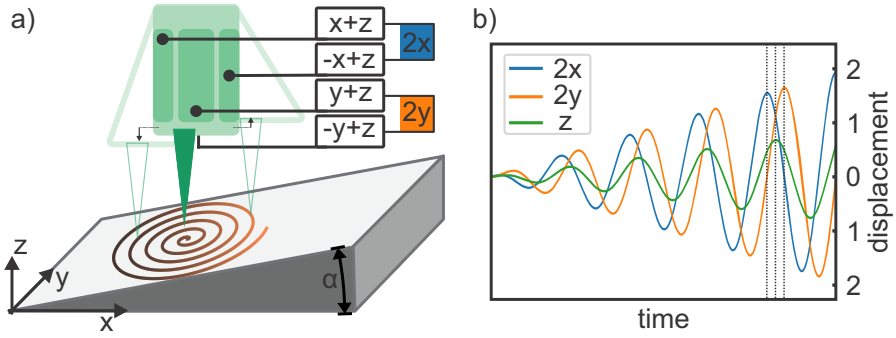

Figure 6.4: Tilt correction for quasi-constant height spiral scans. a) Schematic illustration of the tilt angle α in x-direction. The tilt angle is corrected with respect to the STM tip. For the correction, an additional signal z is added to the four input signals x, $-x$, y, $-y$. The lateral tip displacements results in $2x$ and $2y$. b) The displacements are plotted exemplarily over time. The three dotted vertical lines illustrate the phase shift of lateral displacement and the changing height. Adapted from Ref. [59] licensed under a Creative Commons Attribution (CC BY) license.

the fast spiral scan images acquired at the position indicated by the orange circles. The spiral images have a scan diameter of 22 nm and are acquired with different scan speeds. Figure 6.5d was acquired in 5 s, which corresponds to a frame rate of 20 Hz. For this relatively slow scan speed, the constant current mode was applied. The characteristic step edge configuration from Figure 6.5a is clearly resolved. For higher scan speeds in Figures 6.5e,f, the quasi-constant height mode is used. With this mode the STM resolved the step edge configurations in 0.5 or even 0.025 s, which corresponds to a frame rate of 40 Hz.

The question arises whether or not the spiral scan can also resolve finer structures, such as the herringbone reconstruction on the Au(111) surface. Figure 6.6a shows an overview image acquired in UHV with the raster motion within 214 s. The herringone reconstruction is resolved on the upper and lower terrace. The area marked with the blue square is magnified in Figure 6.6b. Characteristic angles of 120° are visible. Figure 6.6c shows the same area acquired with the spiral scan within 50 ms. This is 1500 times faster than the raster scan in Figure 6.6b. The same structural features are observed.

Spiral scans can resolve the atomic step edges and the herringbone reconstruction on the Au(111) surface with time resolutions that are more than thousand times higher than in conventional STM. Up to this point, only CAV spiral scans have been investigated. In principle numerous spiral geometries and tip velocities are possible, CAV and CLV scans representing two extremes. To analyze the advantages of the two spiral modes, CAV and CLV Archimedean spiral scans are applied to resolve the hexagonal structure of the 3O(2×2) structure on Ru(0001).

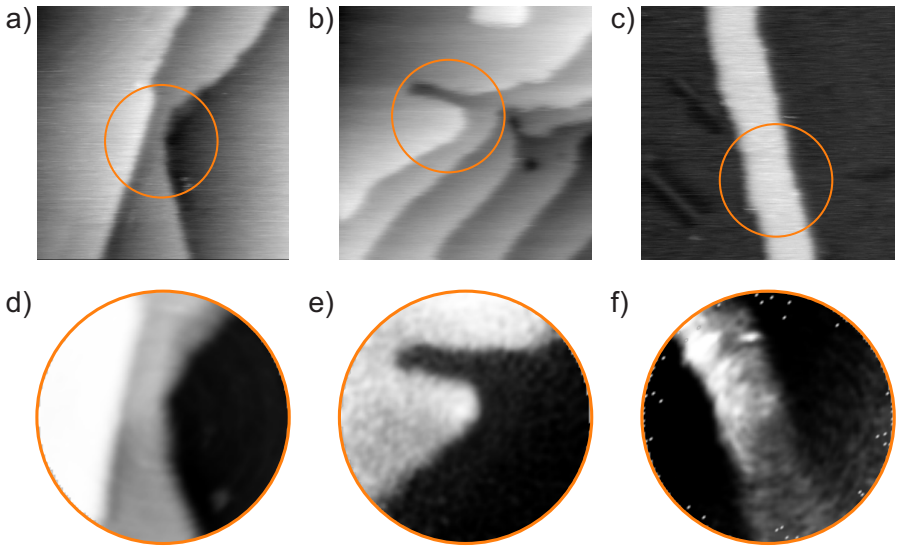

Figure 6.5: Atomic steps on the Au(111) surface resolved by conventional raster scan and spiral scan STM measurements. a-c) Conventional raster scan images of 50×50 nm^2, acquired in 130 s. d-f) Spiral scan STM images acquired in 5 s, 0.5 s, and 0.025 s, respectively. a,d) constant current images (V_S = 0.1 V, I_T = 1 nA). b) constant current, e) quasi-constant height image (V_S = 0.1 V, I_T = 0.2 nA). c) constant current, f) quasi-constant height image (V_S = 0.1 V, I_T = 0.5 nA).

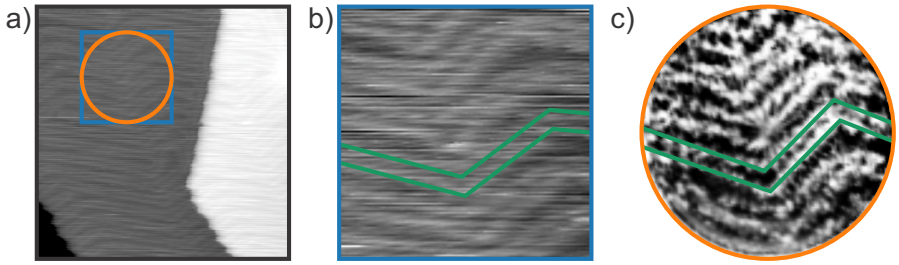

Figure 6.6: Resolved herringbone reconstruction on the Au(111) surface by conventional and spiral STM. a) Conventional raster scan image (90×90 nm^2). b) Magnified region of 32×32 nm^2 marked in a), acquired in 214 s. c) Spiral scan STM image of the area marked with orange in a). The image was acquired in 50 ms (scan diameter = 32 nm). The herringbone structure is marked exemplary with green lines in b) and c). Scan parameters for all images: V_S = 1 V, I_T = 1 nA.

Figures 6.7a-c show the schematic tip trajectories of the raster scan, the CLV spiral scan, and the CAV spiral scan in analogy to Figure 6.3. Below the trajectories, the corresponding STM images are shown. The raster scan is acquired with commercial hardware and software. Oxygen atoms appear bright and form the hexagonal structure. The CLV scan exhibits equidistant points along the scan trajectory. The homogeneous point distribution seems favorable for image acquisi-

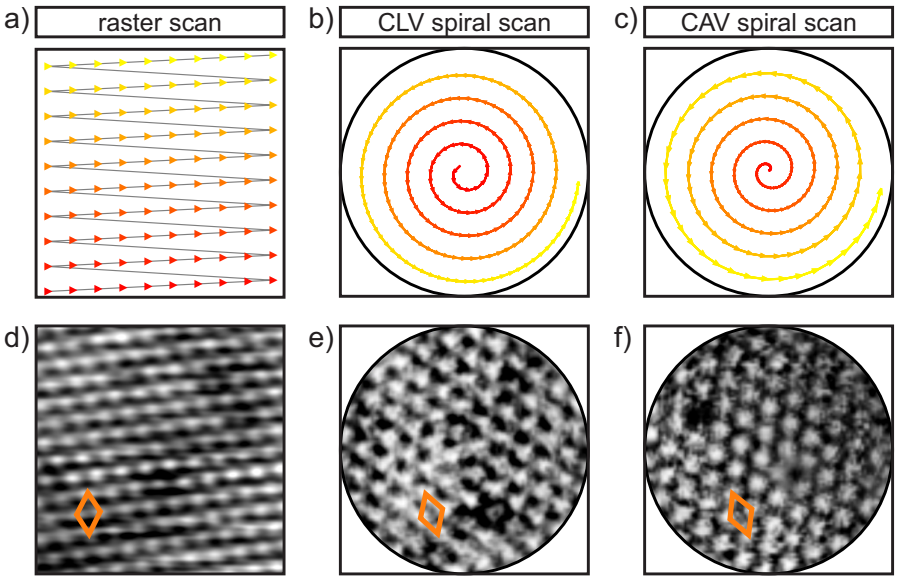

Figure 6.7: 3O(2×2) structure on Ru(0001) resolved by raster, CLV, and CAV scans. a-c) Schematic illustration of scan patterns. Red and yellow triangles along the trajectory indicate data acquisition points and the tip propagation direction. d-f) Atomically resolved STM images of the 3O(2×2) adlayer on Ru(0001) (V_S=1 V, I_T=1 nA, 5×5 nm^2). a,d) Conventional raster scan. b,e) CLV spiral scan. c,f) CAV spiral scan. The unit cells are drawn in orange. Adapted from Ref. [59] licensed under a Creative Commons Attribution (CC BY) license.

tion. However, in the CLV mode, the tip rotates very fast in the center, which results in sharper input signals. The corresponding STM image in Figure 6.7e reveals the hexagonal structure of the 3O(2×2) layer. However, especially the center of the image, lacks clear atomic resolution. The CAV scan, in contrast, shows clearly resolved atomic sites with high spatial resolution in the center. The high resolution is due to the increased point density in the center of the CAV scan. The STM tip rotates with constant speed. Therefore, the tip moves linearly very slow, which in turn increases the point density along its trajectory when scanning with a constant data sampling rate. In general, the increased spatial resolution in the central region of the STM image is desirable. Therefore, the CAV scan is preferred for spiral STM scans.

In this section, two exemplary modes to perform spiral scans were demonstrated. As mentioned above, the spiral geometry and the tip velocity are fully customizable, especially by tuning parameters a and b. Studies with time dependent parameters were also considered and prepared. However, the high spatial resolution and the absence of image distortions promoted the CAV scan.

6.4 DATA PROCESSING

The data acquisition points of unconventional scan patterns do not necessarily coincide with a 2D grid that represents an image. Different methods exist to reconstruct images from the acquired point cloud. In the following, three approaches are presented that are implemented in our purely Python-based program, which is freely accessible [121]. The program enables visualization, processing, and analysis of the acquired image sequences independent of the scan pattern. Besides customizable image reconstruction methods, we implemented 1D and 2D image filters. The real time timestamps are displayed and can be used for further analysis.

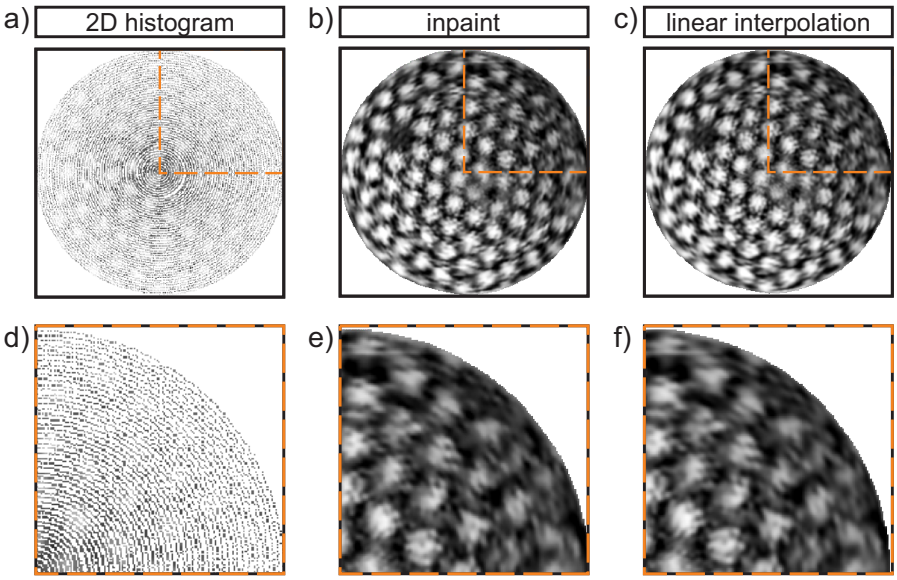

Figure 6.8: Image reconstruction of CAV spiral STM scans. The image reconstruction are performed with the scan presented in Figure 6.7f. a) 2D histogram with 300×300 bins. b) Image a) reconstructed with the inpaint algorithm. c) Linearly interpolated point cloud on the 300×300 grid. a)-c) Scan parameters: V_S = 1 V, I_T = 1 nA, scan diameter = 5 nm. d)-f) show the zoomed areas from a)-c), respectively. Adapted from Ref. [59] licensed under a Creative Commons Attribution (CC BY) license.

Figure 6.8 shows the CAV spiral STM image from Figure 6.7f reconstructed with three different methods to display the point cloud as 2D images. All images in Figures 6.8a-c are reconstructed to a 300×300 bin grid. Figures 6.8a shows the 2D histogram. 2D histograms are computationally most feasible. The point cloud is binned by the equidistant 2D grid. Inside every grid point, the intensity values are averaged. The average intensity value serves as brightness indicator in the image representation. As obvious from Figure 6.8d, for large 2D histogram grids empty grid points result. Empty grid points are avoided by using grids with less than $\frac{\omega}{2}$ points, where ω is the frequency of sine and

cosine functions. This approach was successfully applied to generate live scan displays. More details and examples of 2D histograms with atomic resolution are provided in Section 6.5.

The inpaint algorithm allows to reconstruct the data point cloud on larger 2D grids. The reconstruction is based on the 2D histogram shown in Figure 6.8a and the algorithm is implemented in the scikit-image python package. [122] The atomic resolution is emphasized and the image contrast is very pleasant for the human eye, as obvious from the zoomed section in Figure 6.8e.

Interpolating the point cloud and mapping it on a 300×300 pixels 2D raster image results in Figure 6.8c. For interpolation and mapping, the scipy python package is used. [123] The resulting image is very similar to the inpainted image, as obvious from the zoomed section in Figures 6.8e and f.

As mentioned above, larger images with more pixels are very pleasant for the human eye. However, the inpaint and the interpolation algorithms are computationally expensive - especially for a large number of images. Therefore, these reconstruction methods are only applicable for post-processing routines of high-speed scans.

6.5 LIVE DISPLAY

To monitor the high-speed scan images live, fast routines for the data acquisition and the image reconstruction are necessary.

As mentioned in Section 6.4, a fast routine to reconstruct the point data cloud on 2D image grids is the 2D histogram. The code snippet illustrates how the 2D histogram is generated using the numpy python package. [120] An independent thread on a local computer subscribes to the high-speed scan PV similarly as described in Section 6.2 and processes the data quickly to generate a plane flattened 2D histogram. The generated images for the live display are handled in a separate PV to avoid interference with the data acquisition.

```
1         import numpy as np
2         import import pvaccess as pva
3         from epics import caget
4         from plane_flattening import plane_flatten
5
6         channel = pva.Channel("live_display")
7         x, y, z, I = np.squeeze(np.hsplit(data,4))
8         binsize = caget("live_display:binsize")
9         H, xedges, yedges = np.histogram2d(
10                y, x, bins=binsize, weights=I, normed=False)
11        H_notweighted, xedges, yedges = np.histogram2d(
12                y, x, bins=binsize)
13        H_scale = H / H_notweighted
```

```
        H_scale_flatten = plane_flatten(H_scale)
        channel.put(list(np.ndarray.flatten(H_scale_flatten)),
                    'field(image)')
```

The resulting images are displayed in the Phoebus interface [117], as shown in Figure 6.2. The user can specify the image resolution in terms of the bin size of the 2D histogram interactively within the graphical user interface. Thanks to the fast processing of the 2D histogram, the resolution is then adjusted while measuring and without causing delay in the live display.

First test measurements are performed on the system that was first studied by video STM, i.e. chemisorbed oxygen atoms on the Ru(0001) surface. [31] Figure 6.9 compares unfiltered and filtered spiral scans at different frame rates. It becomes obvious that the acquired raw data already provides atomically resolved images. The unfiltered images resemble images that are displayed in the live monitor during the scan.

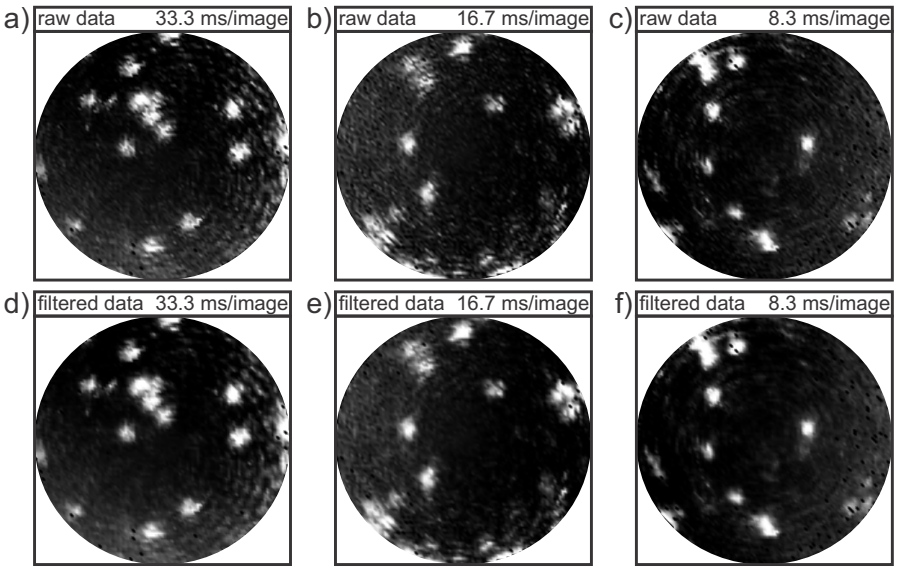

Figure 6.9: Comparison of unfiltered and filtered high-speed spiral STM images. a-c) show the 2D histogram with 100×100 bins based on the unfiltered raw data of the tunneling current deviation. Adsorbed oxygen atoms on the Ru(0001) surface can be identified. For comparison, d-f) show the data filtered with a 2D Gaussian filter. The acquisition times of 33.3 ms, 16.7 ms, and 8.3 ms, respectively, are displayed at to the top of each image (V_S = 0.9 V, I_T = 2.0 nA, T = 300 K, scan diameter = 5 nm). Adapted from Ref. [9] licensed under a Creative Commons Attribution (CC BY) license.

At frame rates as high as 120 Hz dynamic events in consecutive images can be identified at the atomic scale. Figure 6.10 provides an example of migrating oxygen atoms that can be tracked. Within the first 8.3 ms no change in the atomic arrangement is detected. At

t=33.3 ms in Figure 6.10c, an atomic jump is detected, as indicated by the white arrow. In the consecutive 8.3 ms, the oxygen atom jumps to another site. This process is magnified in Figures 6.10e,f.

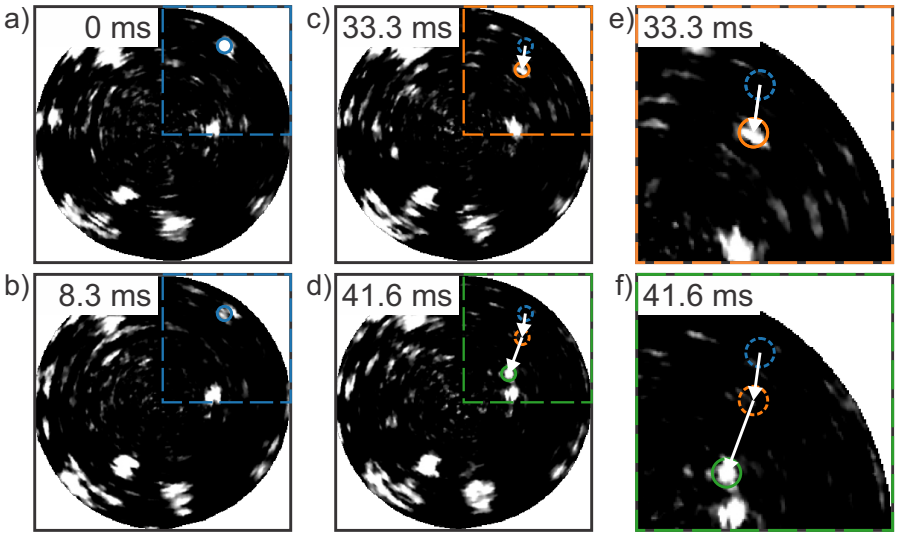

Figure 6.10: Captured dynamics with spiral STM images acquired in 8.3 ms. a-d) Atomically resolved spiral STM images, acquired in 8.3 ms (V_S = 0.9 V, I_T = 2.0 nA, T = 300 K, scan diameter = 5 nm). e-f) show the magnified region highlighted in c,d), respectively. The trajectory of the oxygen atom is indicated with white arrows. The current oxygen atom position is marked with colored circles, previous positions are marked with dotted circles. Adapted from Ref. [59] licensed under a Creative Commons Attribution (CC BY) license.

As discussed in Section 2.2, chemisorbed oxygen was studied in the last decades. The mobility of oxygen atoms at low coverage was studied by Wintterlin et al. [31] Since denser oxygen adlayers are of great importance for the growth of ultrathin oxide films, the mobility within the O(2×2), the O(2×1), and the 3O(2×2) phases are studied in Chapter 7.

Part IV

RESULTS AND DISCUSSION

7

DYNAMICS IN OXYGEN ADLAYERS ON RU(0001)

Oxygen adlayers are present at the interface between oxide thin films and the underlying metal support. They play an important role for these thin film systems. In this chapter we present the analysis of oxygen diffusion within dense adlayers on the Ru(0001) surface at room temperature. The spiral scan is applied in quasi-constant height mode using Archimedean spirals at CAV. The shown high-speed STM images are supported by DFT calculations performed by Joachim Paier from the Department of Quantum Chemistry at Humboldt University, Berlin, Germany.

In Section 7.1, the diffusion within the slightly reduced O(2×2) adlayer on Ru(0001) is presented. The successful observation of the occupied intermediate state along the oxygen diffusion pathway is reported. The majority of the data presented in Section 7.1 is published in Physical Review B in Ref. [60].

At higher oxygen coverage, the slightly reduced O(2×1) becomes stable at room temperature. Section 7.2 discusses the diffusion processes and the dynamic phenomena observed within the O(2×1) adlayer on Ru(0001). Besides mobile oxygen species that lead to structural rearrangements within the O(2×1) layer, fast flipping events of 1D line features are observed. The majority of the data presented in Section 7.2 is published in Physical Chemistry Chemical Physics in Ref. [61].

In Section 7.3, dynamic events in the 3O(2×2) structure are reported. The observed dynamics are reversible over time.

7.1 DIFFUSION IN O(2×2)/RU(0001)

In this section, the mobility within the slightly reduced O(2×2) adlayer on Ru(0001) at room temperature is discussed. First, the energy barriers for diffusing oxygen species is evaluated by DFT calculations. Then, spiral high-speed STM image sequences are used to determine jump rates and to analyze the oxygen diffusion pathway.

7.1.1 *Evaluation of Energy Barriers by DFT*

To investigate dynamics in the O(2×2) adlayer, vacant sites are necessary enabling diffusion processes to occur. Figure 7.1a shows the structure used for DFT calculations to model the reduced oxygen layer. The unit cell is drawn with continuous black lines. It exhibits an oxygen vacancy on one hcp site, resembling the 3O(4×4) structure. The

vacant site enables the study of moving oxygen atoms. The possible diffusion pathway of the oxygen atom is sketched in Figure 7.1a with colored lines. The pathway includes fcc sites, hcp sites on the (2×2) grid, and hcp sites on the (1×1) grid. The corresponding free-energy diagram is shown in Figure 7.1b. The (2×2) hcp sites represent global minima, the fcc sites and the (1×1) hcp site resemble local minima on the energy surface. As evident from the energy diagram, the limiting free-energy barriers are 0.93 eV. This energy difference is based on strongly-constrained-and-appropriately-normed (SCAN) calculations. To assess the rate determining barriers more accurately, the random phase approximation (RPA) is used, as discussed in Ref. [60]. The RPA correction results in free-energy barriers that are 0.14 eV smaller. The resulting limiting barrier of 0.79 eV are in good agreement with literature values. [31, 124] After RPA-correction, the overall free-energy barrier is 0.99 eV.

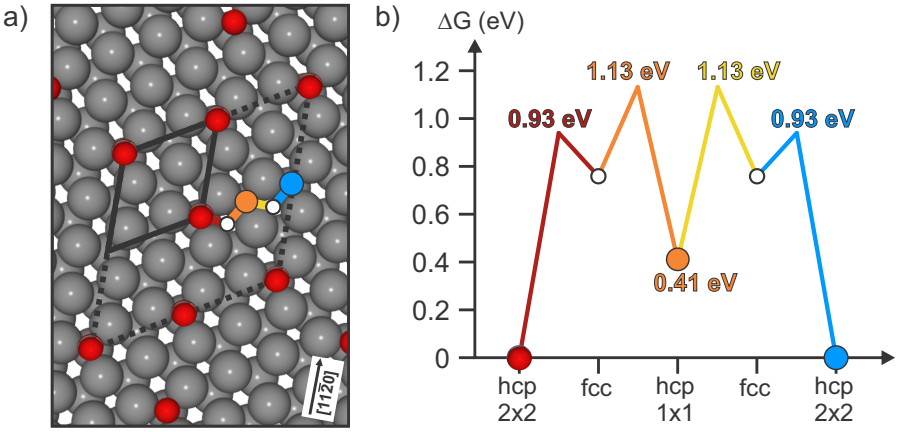

Figure 7.1: Possible migration path of diffusing oxygen on Ru(0001). a) Structure used for DFT calculations, i.e. $3O(4\times4)/Ru(0001)$. The solid black line marks the (2×2)-unit cell. The dotted black line marks the unit cell for DFT calculations. Colored line segments highlight the oxygen migration path. b) Corresponding color coded free-energy diagram. Oxygen atoms are drawn with red circles, oxygen vacancies with blue circles. Reproduced from Ref. [60].

To evaluate the mobility of the oxygen species at room temperature, the free-energy barrier must be related to the jump rate. For diffusion processes that include metastable states, two approaches are reported in the literature to asses the jump rate based on the energy profile. Approach (a) accounts for the highest saddle point [125] and approach (b) accounts for the highest barrier along the migration pathway. [126]

To evaluate the jump rates based on the free-energy barriers, a rate constant according to Eyring's transition state theory is defined. [127]

The rate constant k_1^0 of first order depends on the temperature T and the difference of Gibbs free-energy $\Delta G_0^{\neq}$, as given in equation 7.1.

$$k_1^0 = \frac{k_B T}{h} e^{\left(-\frac{\Delta G_0^{\neq}}{k_B T}\right)}. \tag{7.1}$$

k_B is the Boltzmann's constant and h is the Planck's constant. The residence time τ is defined as the inverse rate constant, as given in equation 7.2.

$$\tau = \frac{1}{k_1^0} \tag{7.2}$$

At 300 K, according to approach (a) that considers the highest saddle point at 0.99 eV, the oxygen species within the O(2 × 2) adlayer would jump every 10,000 s. This corresponds to a jump rate in the order of 0.0001 Hz. Following approach (b), on the other hand, the limiting free-energy barrier of 0.79 eV results in jump rates of 0.33 Hz, i.e. an average residence time of 3 s.

7.1.2 *Imaging with Conventional and Spiral High-Speed STM*

To observe jumping oxygen species in real space and to evaluate their mobility, STM measurements are performed. Figure 7.2a shows the conventional raster STM image acquired in constant current mode. The bright areas are attributed to oxygen atoms, exemplarily indicated with red dots. The resulting unit cell of the O(2 × 2) structure is drawn in orange. Dark areas that break the hexagonal symmetry are attributed to oxygen vacancies, exemplarily indicated with blue dots. The coverage of the chemisorbed oxygen layer on Ru(0001)is approximately θ = 0.23.

As obvious from Figure 7.2a, the dark areas show line features in the fast scan direction of the STM tip. These lines indicate mobile surface species. To observe the hopping events, the frame rate was increased using the high-speed capabilities of the spiral scan. The resulting spiral STM image is shown in Figure 7.2b. The image size is similar to Figure 7.2a and the image contrast is comparable. Atomic sites, i.e. oxygen atoms and oxygen vacancies, can be identified. As obvious from the undistorted unit cell, the spiral image does not show great image distortions. The dark areas attributed to oxygen vacancies do not show line features indicating that the used frame rate of 20 Hz is sufficiently high to resolve the dynamics in separately acquired frames. For illustration, Figure 7.2c shows the structural model of the O(2 × 2) structure on Ru(0001).

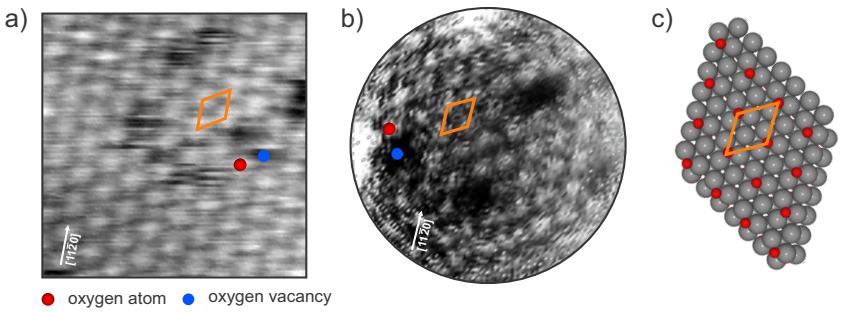

Figure 7.2: Atomic resolution STM images of the O(2×2) adlayer on Ru(0001). a) Constant current raster scan STM image, acquired in 100 s. b) Quasi-constant height spiral high-speed STM image, acquired in 50 ms. Oxygen atoms are exemplarily marked in red and oxygen vacancies are marked in blue. For comparison, the defect free structure is shown in c). The unit cell of the (2×2) grid is drawn in orange. Scan parameters for both raster and spiral scans: V_S = 1 V, I_T = 1.4 nA, T = 300 K, scan area = 5 nm × 5 nm. Adapted from Ref. [60].

7.1.3 *Analysis of Jump Rates*

To analyze whether changes in the local structural arrangement can be detected, consecutive frames are compared. Figures 7.3a,b show consecutive frames acquired in 50 ms. Oxygen atoms are overlaid with red dots and oxygen vacancies with blue dots. Atomic species that changed their position within the 50 ms are highlighted with white outlines. As obvious from Figures 7.3, two jump events occurred. One oxygen atom occupied the adjacent vacant site close to the center of the scan. Another independent jump event is observed close to the rim of the scan. An oxygen atom jumps in anticlockwise direction to an adjacent vacant site. This is against the propagation direction of the STM tip, which scans in clockwise direction.

In general jumps in all directions and throughout the scan area are observed. These observations and the small tunneling current compared to measurements reported in the literature [31] affirm that the observed dynamics are not tip induced.

Figures 7.3c provides an example, where the trajectories of individual oxygen vacancies are drawn. The color code for the acquisition time, which exceeds 50 s, is provided on the right.

While the vacancy located at position 1, does not move within the acquisition time, the vacancy at position 2 jumps in alternating manner between three adjacent positions, as indicated by the colored trajectories. The vacancy at position 3 covers longer distances. Its trajectory, however, is not uniform over time. In the fist 16.7 s, the vacancy jumps from position 3 to 4. During this time, its average jump rate is 0.54 Hz. At position 4 it rests for 14 s before it continues to change its location.

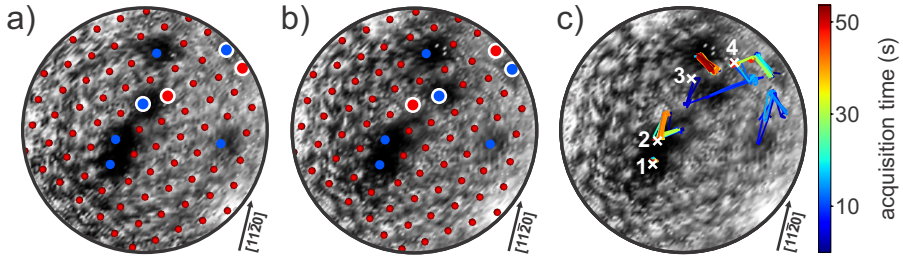

Figure 7.3: Resolved atomic jumps in the O(2×2) layer on Ru(0001). a,b) Atomically resolved spiral STM images, acquired in 50 ms (V_S = 1 V, I_T = 1.4 nA, T = 300 K, scan diameter = 5 nm). Moving species are outlined with white circles. c) STM image with overlaid oxygen vacancy trajectories color coded with respect to the acquisition time. Reproduced from Ref. [60].

To determine the jump rate, consecutive frames of several scans are analyzed. The average oxygen vacancy jump rate is in the order of 0.1 to 1 Hz.

Due to the stochastic nature, a broad distribution of individual jump processes is expected. In addition, the underlying substrate, which is not accessible to STM, and related defects might influence the oxygen vacancy mobility locally. As obvious in Figures 7.3, vacancies can be adjacent to other oxygen vacancies. To evaluate whether the vicinity of these vacancies and the changed chemical surrounding affect the jump rate, as well, Figure 7.4 plots the evolution of the nearest neighborhood of two independent vacancies.

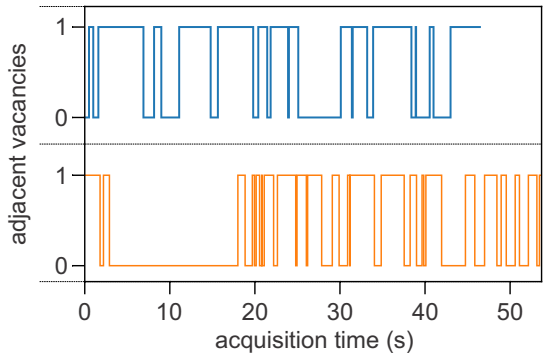

Figure 7.4: Evolution of the oxygen vacancy nearest neighborhood. Two individual vacancies (blue and orange line) are tracked and their nearest neighborhood is plotted. They have either 0 adjacent vacancies, which corresponds to, six neighboring oxygen atoms, or they have 1 adjacent vacancy, which corresponds to five nearest oxygen atoms. Reproduced from Ref. [60].

Their configurations change between 0 adjacent vacancies, i.e. the vacancy is surrounded by six oxygen atoms, and 1 adjacent vacancy. The upper blue line is shorter because the tracked vacancy jumped out of the scan area. In both cases, jumps towards and away from another vacancy are observed. In total, the two vacancies remain 45-65% of

the time in a configuration where they have 1 adjacent vacancy. The probability that two vacancies are adjacent p_{VV} is given by equation 7.3, where c_V is the concentration of oxygen vacancies.

$$p_{VV} = 6c_V \tag{7.3}$$

The oxygen vacancy concentration at a coverage θ of 0.23 is 0.08. Hence, the probability of two adjacent vacancies in the here investigated oxygen adlayer case is 48%. The very good agreement of theoretical and experimental values indicate that there is no preferred configuration. The fact that the configuration of the individual vacancies changes frequently between 0 and 1 adjacent vacancies in Figure 7.4 affirms this conclusion. Adjacent vacancies do not seem to have an influence on the vacancy mobility. More studies on the influence of the nearest neighborhood on the vacancy mobility are interesting for future experiments.

At higher frame rates of 40 Hz, the oxygen vacancies are still detectable, as shown in Figure 7.5. Individual jump events can be identified. In analogy to Figure 7.3c, Figure 7.5c shows the color coded trajectories of individual oxygen vacancies.

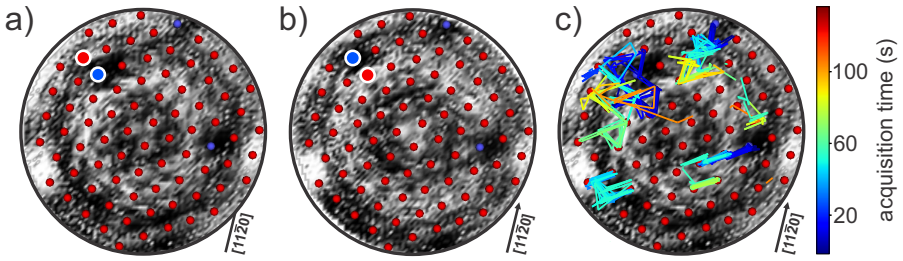

Figure 7.5: Resolved atomic jumps in the O(2×2) layer at 40 Hz. a,b) Atomically resolved spiral STM images, acquired in 25 ms (V_S = 1 V, I_T = 1.4 nA, T = 300 K, scan diameter = 5 nm). Moving species are outlined with white circles. Adapted from Ref. [60]. c) STM image with overlaid oxygen vacancy trajectories color coded with respect to the acquisition time.

The resulting jump frequency is similar to the one determined from 20 Hz scans and is in the order of 0.1 to 1 Hz. Figure 7.6 plots the distribution of determined rates from several tracked vacancies in scans of 20 Hz and 40 Hz. The rates are weighted with respect to the time the vacancies have been tracked.

7.1.4 *Observation of Occupied Intermediate State*

For the diffusion of chemisorbed oxygen on Ru(0001), discrete hopping events are considered. However, the pathway suggested in Figure 7.1 includes intermediate states. Most prominent is the state at the hcp site on the (1 × 1) grid with free-energy barriers of 0.72 eV. To answer

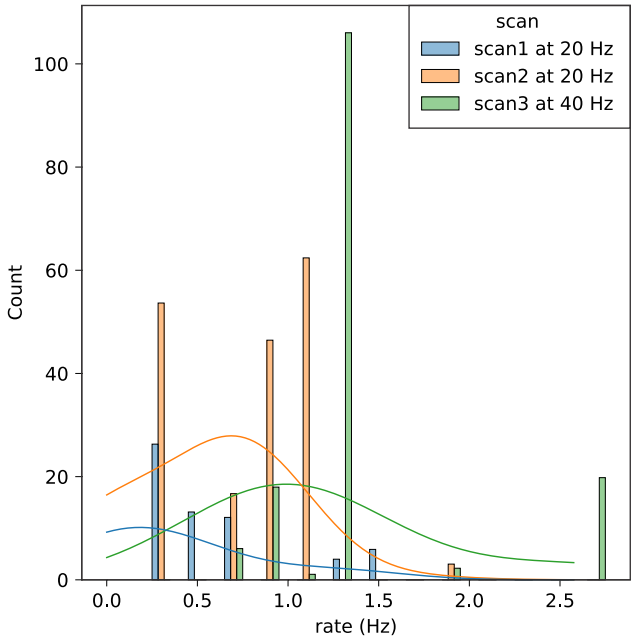

Figure 7.6: Jump rates of oxygen vacancies in the O(2×2) layer. The jump rates are weighted with respect to the time time the vacancies have been tracked. Reproduced from Ref. [60].

the question whether this intermediate state is also occupied during the diffusion process, the centers of spiral STM images are analyzed. As pointed out in Section 6.3, the spatial resolution in the central region of CAV spiral scans is increased due to the high data point density and the slower lateral tip velocity. In addition, in the center of the spiral, the time resolution is increased compared to the overall frame rate due to consecutive inward and outward scans. Figure 7.7 shows three consecutive spiral scans acquired in 50 ms. The region of interest marked with white circles in Figures 7.7a-c is acquired in 16 ms. Because Figure 7.7a is an inward scan and Figure 7.7b is an outward scan, the time difference between these two acquired regions of interest is only 16 ms. The magnified areas are shown in the second row of Figure 7.7.

In the third row, the atomic positions are overlaid. It becomes obvious that the oxygen atom marked with a white outline migrates towards the vacant site. In Figure 7.7h, it is located at an intermediate position between the two hcp sites on the (2×2) grid until it finally reaches the vacant hcp site in Figure 7.7i.

For visualization, the structure model from Figure 7.1a is shown in Figures 7.7j-l. The direct comparison reveals that the experimentally observed occupied intermediate state agrees very well with the intermediate state along the diffusion pathway that is predicted theoretically, i.e. the hcp site on the (1×1) grid.

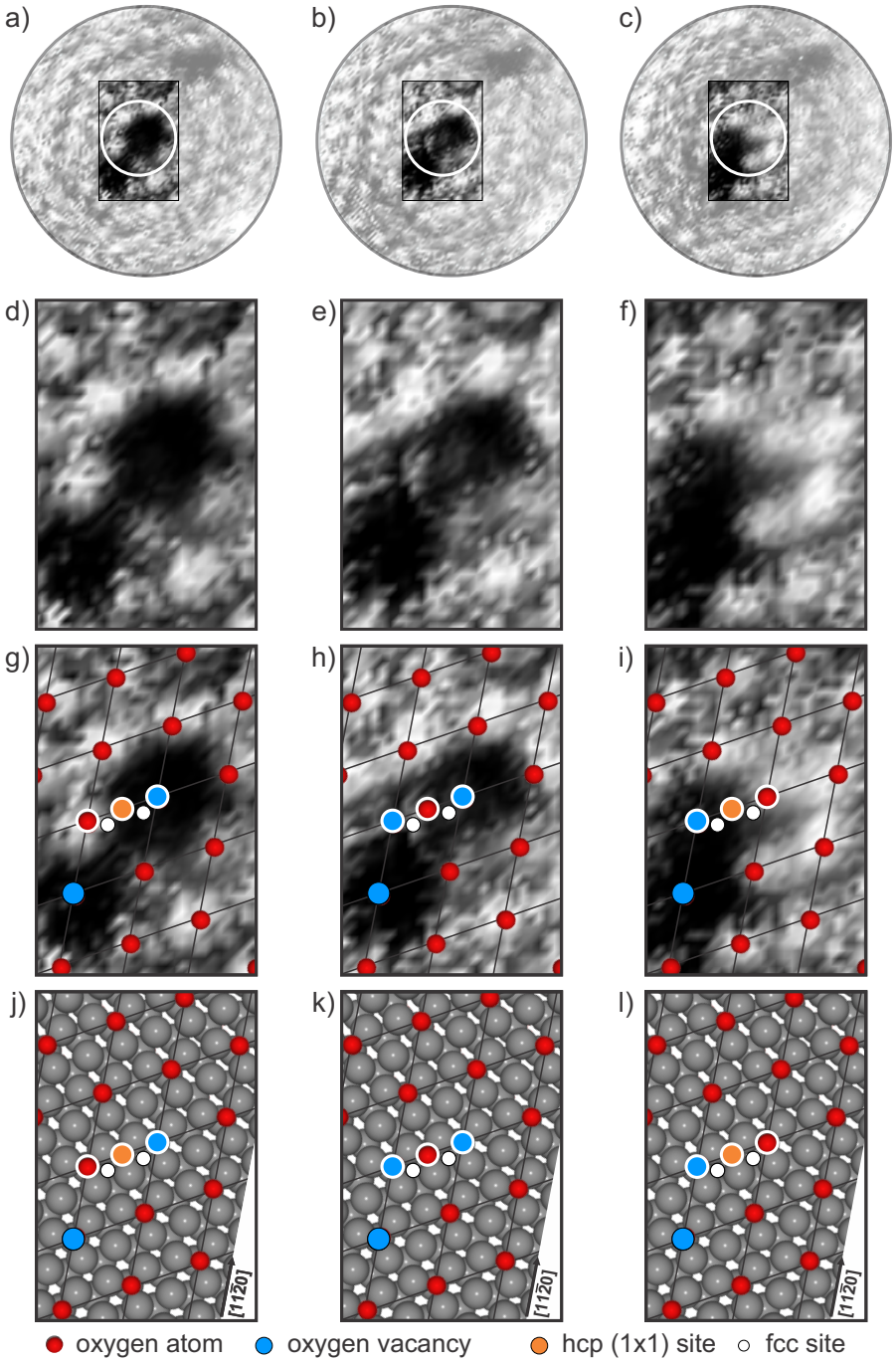

Figure 7.7: Resolved occupied intermediate state along the oxygen diffusion pathway. a-c) Consecutive atomically resolved spiral STM images, acquired in 50 ms. a) Inward, b) outward, c) inward scan (V_S = 1 V, I_T = 1.4 nA, T = 300 K, scan diameter = 5 nm) The central regions marked with white circles are acquired in 16 ms. d-f) Magnified scan areas highlighted in a-c), respectively (area = 2.2 nm × 1.4 nm). g-i) Images from d-f) with overlaid atomic structure models. j-l) Aligned structural models in analogy to Figure 7.1a. Reproduced from Ref. [60].

The phenomenon was experimentally observed for several distinct configurations in the central region of the spiral scan that exhibits enhanced temporal resolution.

In conclusion, mobile oxygen species are resolved in the oxygen deficient O(2 × 2) adlayer on Ru(0001). Beyond the discrete individual hopping events, experimental evidence is provided of an occupied intermediate state along the oxygen diffusion pathway. To answer the question if oxygen species are also mobile in denser oxygen adlayers, Section 7.2 discusses the dynamics within the O(2 × 1) layer on Ru(0001).

7.2 DYNAMICS IN O(2×1)/RU(0001)

In this section, the mobility within the O(2 × 1) adlayer on Ru(0001) at room temperature is discussed. The structure of this section is similar to the on of Section 7.1. First, the energy barriers for diffusing oxygen species is evaluated by DFT calculations. Then, spiral high-speed STM image sequences are used to study the dynamics of the sample system experimentally.

7.2.1 *Evaluation of Energy Barriers by DFT*

In analogy to the studies on the O(2 × 2) adlayer on Ru(0001) described in Section 7.1, DFT calculations are performed by Joachim Paier to evaluate the energy barriers for oxygen diffusion within the O(2 × 1) layer. Figure 7.8a shows the structure used for the theoretical calculations. The suggested diffusion pathway for the oxygen atom (red circles) towards the vacant site (blue circles) is sketched by colored line segments. The energy diagram on the right is directly related to the color coded pathway. The energy barriers are in the range of 0.69 to 0.73 eV. Based on these energy differences, at room temperature jump rates of 3 to 16 Hz are expected using equation 7.1, according to Eyring's transition state theory. [127] We found that the pathway drawn with the dotted black arrow is not feasible due to the very unstable fcc site along this path. [61] Therefore, the trajectory is only drawn for the migration to the vacant hcp site on the (1 × 1) grid.

Figure 7.8b shows several unit cells. The adsorbed oxygen atoms form characteristic 1D stripes, as indicated by the green lines. Due to the periodically arranged oxygen vacancies, every second line is less dense. Considering the jump event towards the hcp site on the (1 × 1) grid in several unit cells, the structure in Figure 7.8c results. The orientation of the 1D stripes changes. The blue lines indicate the new stripe orientation, which is rotated by 120° compared to the stripe orientation in Figure 7.8b.

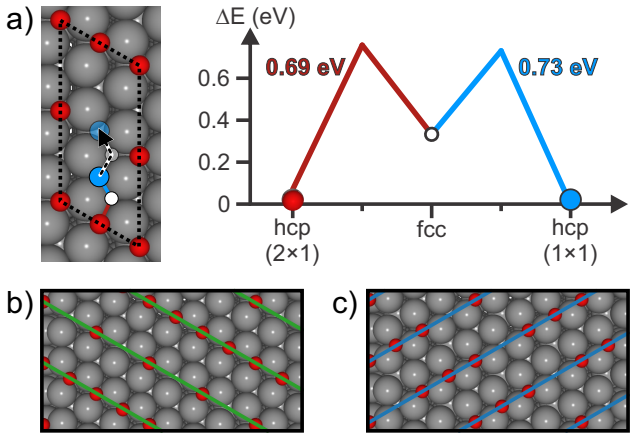

Figure 7.8: Theoretical considerations of dynamics in the O(2 × 1) layer on Ru(0001). a) Unit cell of the 3O(4 × 2) structure for theoretical calculations. The possible migration path for oxygen vacancies to vacant sites is drawn with colored line segments. The corresponding energy diagram calculated with SCAN is shown on the right. b) Several neighboring unit cells of the 3O(4 × 2) structure (2.3 nm × 1.3 nm). The characteristic 1D stripes are marked with green lines. c) The same section as in b) after the oxygen diffusion events from hcp sites on the (2 × 1) grid to the hcp sites on the (1 × 1) grid. Reproduced from Ref. [61] with permission from the Royal Society of Chemistry.

7.2.2 *Imaging with Conventional and Spiral High-Speed STM*

To study experimentally whether the oxygen atoms in the O(2 × 1) layer are mobile at room temperature, we performed STM measurements. Figure 7.9a shows the conventional STM image of the O(2 × 1) adlayer on Ru(0001), acquired in constant current mode in 100 s. On the left, three of the characteristic 1D lines are drawn in green and the unit cell is drawn in black. From this image, it becomes obvious that the layer exhibits domains with different stripe orientations rotated by 120°. In the literature, larger scale images can be found showing STM images with domain sizes ranging from below 1 nm to above 10 nm. [54, 57] In Figure 7.9a, the surface is not entirely covered with oxygen but rather shows some depleted areas close to the O(2 × 1) domains and within individual 1D stripes. The image contrast is in agreement with reported oxygen vacancies in O(2 × 1) domains. [56]

Figure 7.9b shows the spiral STM image of the same image size, acquired in 33 ms. The image contrast of the spiral scan images in this section is enhanced by histogram equalization. Gaussian filters are applied to slightly smoothen the STM images. The 1D lines in the spiral scan can be identified, similar to Figure 7.9a. For comparison, the structure without oxygen vacancies is shown in Figure 7.9c.

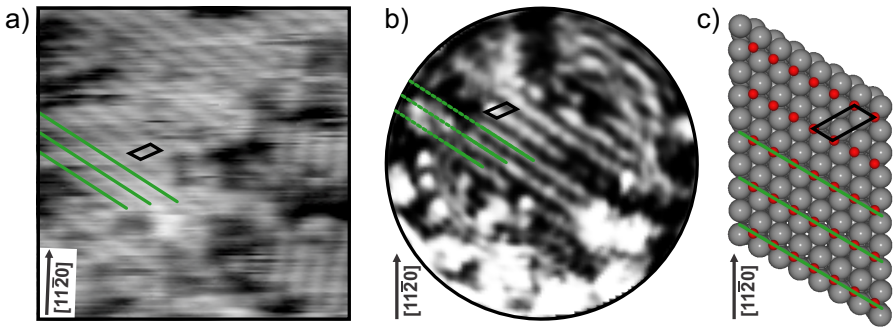

Figure 7.9: Atomic resolution STM images of the O(2×1) adlayer on Ru(0001). a) Constant current raster scan STM image, acquired in 100 s. b) Quasi-constant height spiral high-speed STM image, acquired in 33 ms. For comparison, the defect free structure is shown in c). Characteristic 1D lines are drawn in green and the unit cell of the (2×1) grid is drawn in black. Scan parameters for both raster and spiral scans: V_S = 0.6 V, I_T = 1.4 nA, T = 300 K, scan area = 9 nm × 9 nm. Reproduced from Ref. [61] with permission from the Royal Society of Chemistry.

7.2.3 *Analysis of Experimentally Observed Dynamics*

To detect individual jump events, consecutive frames of the spiral high-speed scans are analyzed. Figure 7.10 shows two consecutive frames from a longer image series, acquired with 30 Hz. The dashed white rectangle highlights the region of interest. The inset in Figure 7.10a shows the characteristic 1D stripe pattern of one domain. Within this domain a depression is detected, circled in green. This depression is attributed to an oxygen vacancy. In the literature similar contrasts of vacancies in the O(2 × 1) phase on Ru(0001) are reported. [56] In the consecutive frame in Figure 7.10b, the vacancy changed its position, as indicated by the white arrow. Tracking different vacancies, jump rates in the order of 0.1 to 1 Hz are determined.

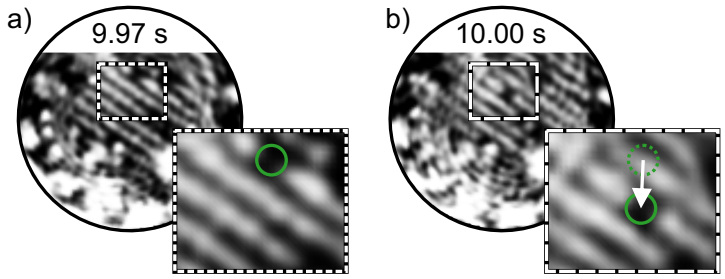

Figure 7.10: Resolved atomic jumps in the O(2×1) layer on Ru(0001). Atomically resolved spiral STM images, acquired in 33 ms (V_S = 0.6 V, I_T = 1.4 nA, T = 300 K, scan diameter = 9 nm). a) The detected oxygen vacancy position is marked with a green circle. b) The oxygen position changed as indicated by the white arrow. Reproduced from Ref. [61] with permission from the Royal Society of Chemistry.

Figure 7.11 focuses on the dynamics in a single 1D line of one domain. The STM images are extracted from a longer scan series at constantly high frame rates of 20 Hz. For visualization, the regions marked with white dashed rectangles in Figures 7.11a and b are magnified in Figures 7.11c and d. Within 50 ms, the atom configuration changes, as indicated by the orange circles. In the consecutive frames, the configuration of the 1D line changes frequently. No configuration seems to be preferred and similar arrangements recur. For instance, the configuration in Figures 7.11e and f is the same for the highlighted 1D line.

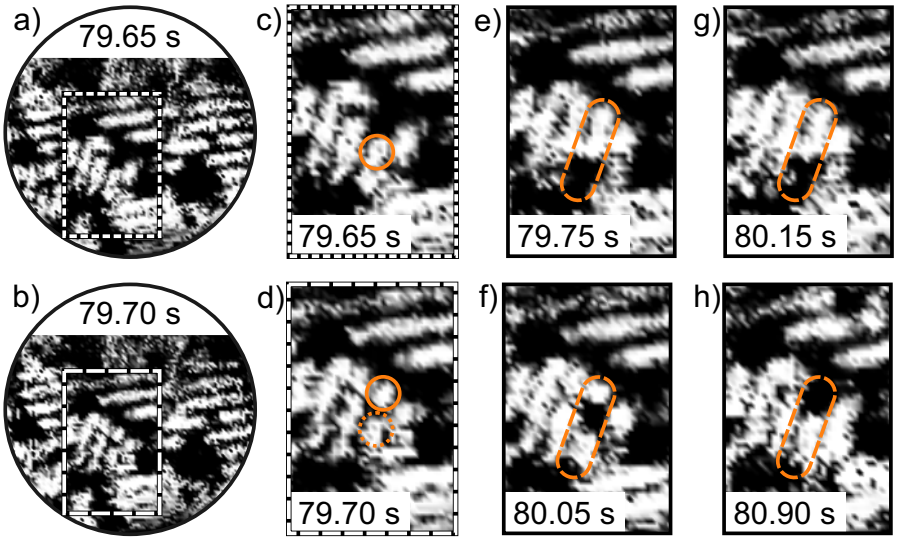

Figure 7.11: Atomically resolved jump events inside O(2×1) 1D lines. a,b) Spiral STM images extracted from a longer scan series, acquired in 50 ms (V_S = 1 V, I_T = 1 nA, T = 300 K, scan diameter = 9 nm) c,d) magnify the regions highlighted with dashed white frames in a) and b), respectively (area = 3.4 nm × 5.1 nm). Dynamics in the 1D line are highlighted in orange. e-h) show the same magnified section at different times. The atomic configuration in the orange frame changes reversibly. Reproduced from Ref. [61] with permission from the Royal Society of Chemistry.

The question arises whether the dynamic events only occur within individual domains or if the domain sizes and their configuration also changes over time. To answer this question, areas that include several domains are analyzed over longer times, exceeding minutes. Figure 7.12 shows spiral STM images of such a scan series acquired with 20 Hz. The domains with different stripe orientations change in size. Figures 7.12c and f highlight the 1D line orientations. The normalized line length, which corresponds to the fraction of 1 monolayer (ML) of the O(2 × 1) adlayer, is plotted in Figure 7.12g for the three different domain orientations as a function of time.

The single domains increase and decrease over time without following a clear trend. First, the orange (vertical) lines grow. Comparing

the blue and orange line in Figure 7.12g, it becomes obvious that one domain orientation grows at the expense of the other. Later, the process is inverted and the blue (horizontal) domain grows at the expense of the orange (vertical) domain. The blue and orange line in Figure 7.12g appear almost mirrored. At the end of the acquisition time, the blue domain dominates after several reversible changes in size. The comparison of the images in Figures 7.12c and f, reveals the stripe reorientation by 120° over more than 20 s. This effect is comparable to the theoretical reorientation of 1D lines, as shown in Figure 7.8.

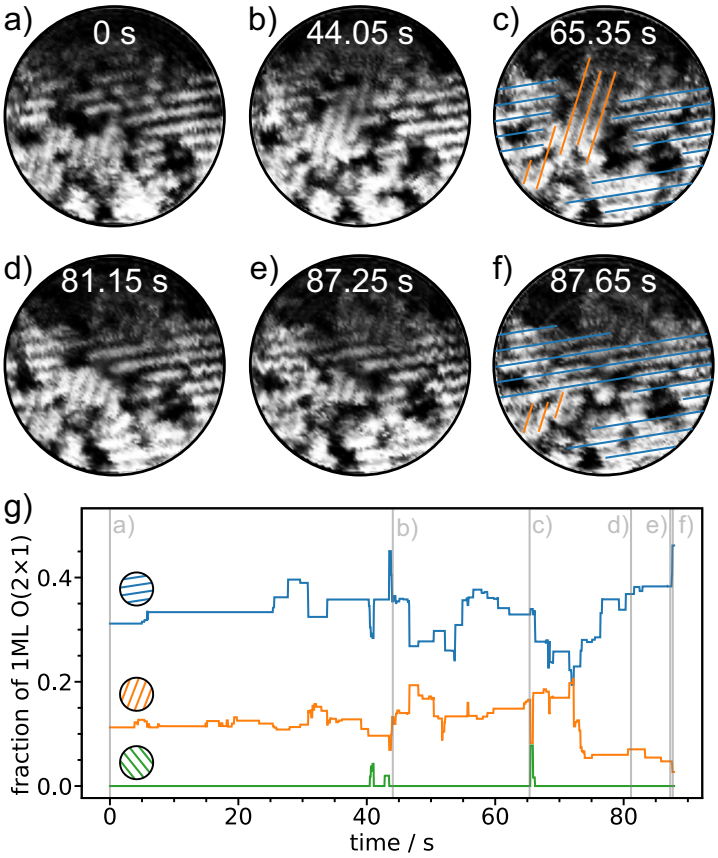

Figure 7.12: Evolution of O(2×1) domain orientations. a-f) Spiral STM images extracted the same scan series as Figure 7.11 (V_S = 1 V, I_T = 1 nA, T = 300 K, scan diameter = 9 nm). The 1D line orientation are highlighted in c) and f). g) plots the summed 1D line length of each domain orientation normalized to the line length of 1 ML O(2×1). The times of the image acquisition of a-f) are marked with vertical gray lines. Reproduced from Ref. [61] with permission from the Royal Society of Chemistry.

To focus on this phenomenon that one domain grows at the expense of the other, consecutive frames are investigated in detail. The upper row of Figure 7.13 shows two consecutive frames, acquired within 50 ms. The time stamps directly relate to Figure 7.12. The central regions marked with dashed white circles in Figures 7.13a and b, are magnified in c and d. The color coded 1D lines illustrate that the

orientation changes quickly within the time difference of 50 ms. The fast flipping of stripe orientations relates to the "long-term" reorientation in Figure 7.12 and shows the same behavior as the theoretical reorientation considering collective diffusion events in Figure 7.8. The lower row in Figure 7.13 focuses on the time after t = 65.35 s. The 1D line orientation changes from orange to blue from Figure 7.13e to g. In Figure 7.13h, the lines flip back and the orange domain is dominant again.

Figure 7.13i zooms into the plot from Figure 7.12g after t = 65.35 s. The trend of competing domain sizes is clearly visible in the gray shaded region. The blue and the orange line are almost mirrored. This behavior on the millisecond scale is comparable to the "long-term" process observed in Figure 7.12 and directly relates to the restructuring that spans beyond minutes.

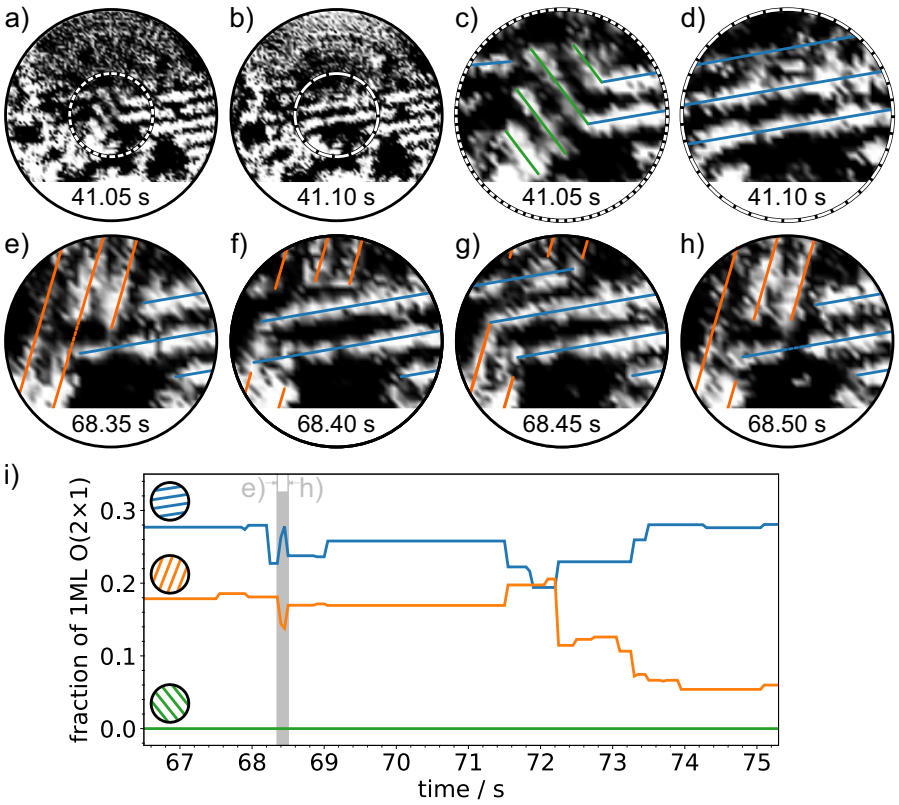

Figure 7.13: Fast flip events of 1D line orientations. a,b) Spiral STM images extracted the same scan series as Figures 7.11 and 7.12 (V_S = 1 V, I_T = 1 nA, T = 300 K, scan diameter = 9 nm). c,d) magnify the regions highlighted with dashed white circles in a) and b), respectively (diameter = 3.5 nm). e-h) show the same magnified section at different times. Fast flipping events of the 1D lines are observed occurring within 50 to 100 ms. i) Zoom of Figure 7.12g with indicated times of frames e-h). Reproduced from Ref. [61] with permission from the Royal Society of Chemistry.

In some cases, the total amount of oriented 1D lines seems to change as well, i.e. the sum of all three ML fractions increases or decreases slightly.

To analyze if the total amount of 1D lines increases or decreases as a function of time, scan areas showing little to no 1D structures are considered. Figure 7.14 shows spiral STM images of another scan sequence, acquired with 20 Hz. In the first frame in Figure 7.14a, the oxygen atoms are not well ordered and the identification of 1D lines is ambiguous. In the following frames, 1D lines appear and disappear. In Figure 7.14b, for instance, two small domains can be identified. This is one example where the summed length of detected lines increases. Towards Figure 7.14c, the orange domain grows on the expense of the green domain. The size of the now dominating orange domain fluctuates but the domain is still detected after minutes. Comparing the rather unstructured atomic configuration in Figure 7.14a and the structured domains in Figure 7.14d, it becomes obvious that the 1D line segments grow over time. The growth process, however, consists of fluctuations and reversible processes, e.g. the formation of differently oriented domains, as shown in Figure 7.14b.

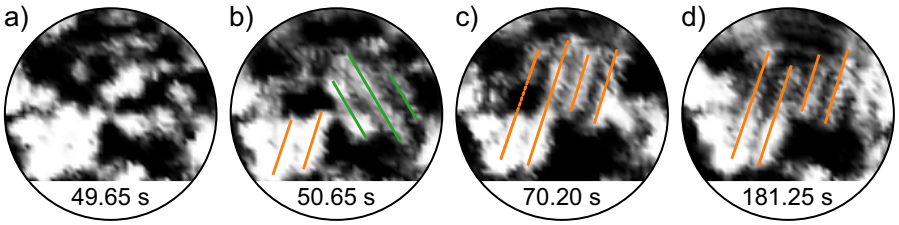

Figure 7.14: Growing O(2×1) domains. Spiral STM images extracted from a longer scan series, acquired in 50 ms (V_S = 1 V, I_T = 1 nA, T = 300 K, scan diameter = 4.6 nm). Oxygen atoms arranged with small degree of order in a) form 1D lines of different orientation in b). The line orientations change dynamically until the resulting domain is observed for longer times in c) and d).

In summary, spiral high-speed STM measurements revealed the dynamics in the oxygen adlayer at room temperature. The phenomena observed within minutes could be related to the fast dynamics at the millisecond timescale. The observed fast flips of the 1D stripe orientations and the gradually restructuring of individual domains on the nanometer scale are similar to theoretical considerations of structural 1D stripe reorientations.

7.3 DYNAMICS IN 3O(2×2)/RU(0001)

In this section, experimentally observed dynamic changes within the 3O(2 × 2) adlayer on Ru(0001) at room temperature are discussed. Spiral high-speed STM image sequences are shown that illustrate dynamic changes in the image contrast over time.

7.3.1 *Imaging with Conventional and Spiral High-Speed STM*

The 3O(2 × 2) adlayer is prepared prior to the growth of a variety of ultrathin oxide film systems on Ru(0001) crystals. The image contrast of the 3O(2 × 2) structure on Ru(0001) is known to exhibit round or triangular shapes based on the STM tip condition. [54, 93] Figure 7.15a shows the conventional STM image exhibiting hexagonally arranged protrusions. The protrusions are assigned to three adjacent oxygen atoms.

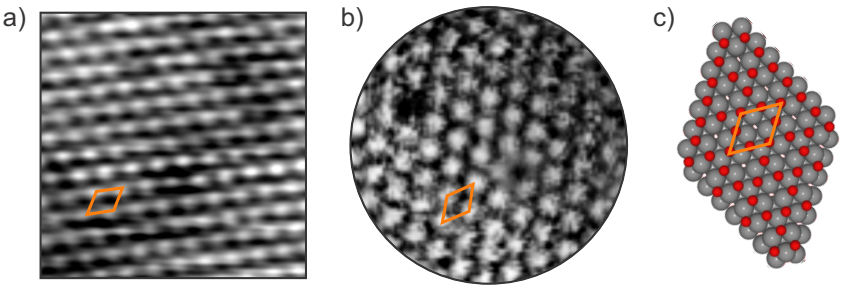

Figure 7.15: Atomic resolution STM images of the 3O(2×2) adlayer on Ru(0001). a) Constant current raster scan STM image, acquired in 160 s. b) Quasi-constant height spiral high-speed STM image, acquired in 50 ms. For comparison, the defect free structure is shown in c). Scan parameters for both raster and spiral scans: V_S = 1 V, I_T = 1 nA, T = 300 K, scan area = 5 nm × 5 nm. Adapted from Ref. [59] licensed under a Creative Commons Attribution (CC BY) license.

The spiral image in Figure 7.15b shows a similar contrast that is also reported in the literature. [54] Due to this image contrast, individual oxygen atoms cannot be assigned. However, in 7.15a dark regions can be identified. These darker areas indicate local defects such as local oxygen deficiencies in the adlayer. Also the spiral image in Figure 7.15b shows one dark area in the upper left corner. To answer the question whether these local structural features change as a function of time, spiral STM sequences are analyzed in the following section.

7.3.2 *Experimentally Observed Dynamics*

Figure 7.16 shows the 3O(2 × 2) layer over a time span of approximately 10 s. To analyze differences in the image contrast, the raw data is shown without applied filters.

Figure 7.16a is very similar to the image shown in Figure 7.15b. In the consecutive frames, the region circled in orange changes its contrast several times. Depressions become detectable that are very pronounced in Figure 7.16f. In Figure 7.16g, a protrusion is detected in the upper half of the orange circle that coincides with the hexagonal grid. In the following frames in Figures 7.16h-k, the protrusion changes

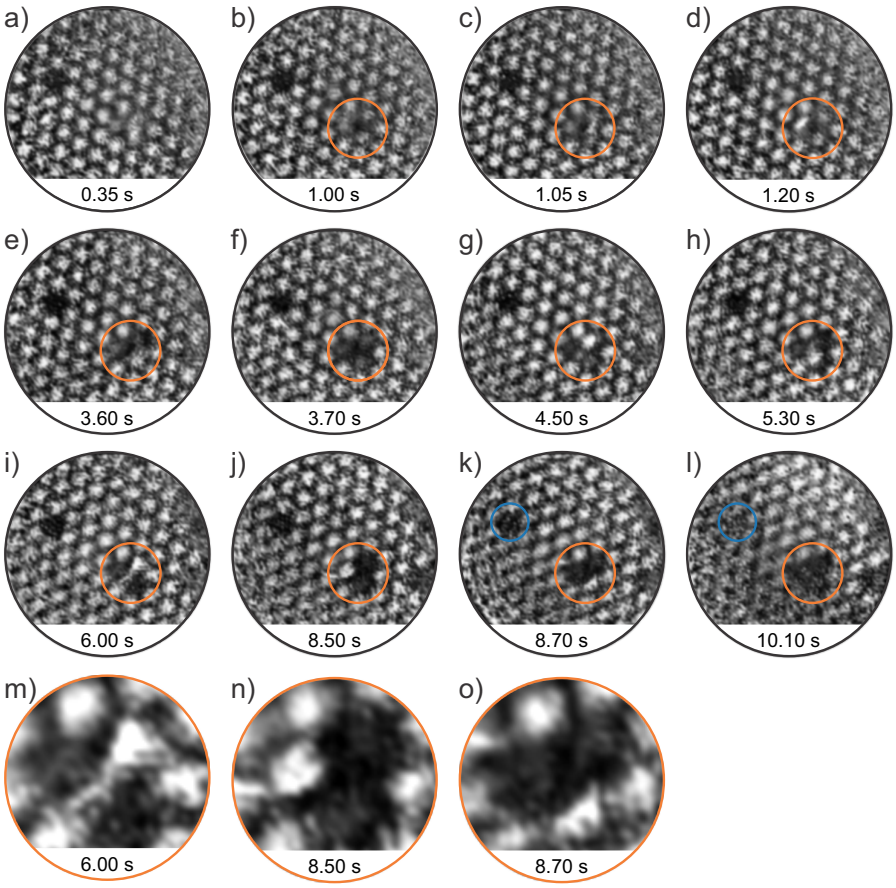

Figure 7.16: Resolved dynamics in the 3O(2 × 2) structure on Ru(0001). a-l) Spiral STM images show local changes in the contrast highlighted by colored circles (V_S = 1 V, I_T = 1 nA, T = 300 K, scan diameter = 5 nm). m-o) Magnified regions marked in orange in i-k), respectively (diameter = 1.5 nm).

its position several times to other grid sites. This effect becomes very obvious in the magnified images in Figures 7.16m-o.

Throughout the scan sequence, the the dark area in the upper left of the spiral images changes its position slightly. From Figure 7.16k to Figure 7.16l, the image contrast changes significantly in this area and the depression can no longer be detected.

The dynamic processes, especially the changes of the occupied grid sites in Figures 7.16h-k, are clearly visible. However, as mentioned above, the image contrast does not allow to track individual atomic oxygen atoms. The question of the underlying atomic processes is subject to future studies.

The spiral STM measurements revealed the dynamic processes in the dense 3O(2 × 2) adlayer on Ru(0001) at room temperature. The observed dynamics may affect the film growth of ultrathin oxide films. Especially films prepared on oxygen precovered metal crystals may show characteristics that depend on the interfacial oxygen layer and the dynamics therein.

8

STRUCTURAL ANALYSIS OF THIN OXIDE FILMS

In this chapter, software tools are introduced that enable the structural analysis of large data sets of STM images on thin oxide films. We developed a semi-automated network detection tool, which is implemented in the spiral scan analysis python software. [128]

In Section 8.1, the working principle of the network detection is explained on static STM images. Thanks to the network detection, the structural evolution of a silica bilayer across a supporting metal step edge could be studied. The results reveal the continuous coverage of the vitreous silica film across the metal step edge. The experimental findings are complemented with DFT calculations performed by Sergio Tosoni and Gianfranco Pacchioni from the Department of Materials Science at Università di Milano-Bicocca, Italy. The majority of the data presented in Section 8.1 is published in Physical Review Materials. [129] The data shown in Section 8.3 is part of an ongoing article. [140]

8.1 CONTINUOUS COVERAGE OF VITREOUS SILICA ACROSS A METAL STEP EDGE

In this section, the semi-automated network detection is presented on the example of a silica bilayer across a supporting metal step edge. Detected structural features are compared to theoretical DFT calculations.

8.1.1 *Semi-Automated Network Detection*

Previous studies on thin oxide film systems have demonstrated the importance of structural analysis. [75, 79, 81, 83, 84, 130–134] To enable the thorough analysis of larger data sets, we developed a semi-automated network detection that reveals structures on different length scales. [128]

Figure 8.1 illustrates the process of network detection. Figure 8.1a shows the STM image of a silica bilayer supported on Ru(0001) with an underlying substrate step edge. First, the ring center positions of the film are identified by an intensity minimum detection, as shown in Figure 8.1b. The detected positions can be adjusted interactively in the graphical user interface (GUI) of the program. Subsequently, the image is segmented taking the ring center positions as starting point and using the random walker algorithm. [135] The resulting segmented image is shown in Figure 8.1c. The colors represent unique labels of the individual segments. Based on the information which

segments are adjacent, a region adjacency graph (RAG) is created. The nodes of this graph represent the ring centers and the edges represent the connections between adjacent rings, drawn in black in Figure 8.1d. Based on geometric considerations, the oxygen (red) and silicon atom (green) positions are calculated. Additional mathematical graphs are created that represent the atom networks and allow for versatile structural analysis. Figure 8.1e shows the silicon atom network, which is superimposed on the STM image in Figure 8.1f.

As obvious from the overlaid structure, the network agrees coincides with the STM image contrast. Most importantly, the network is continuous across the underlying metal step edge.

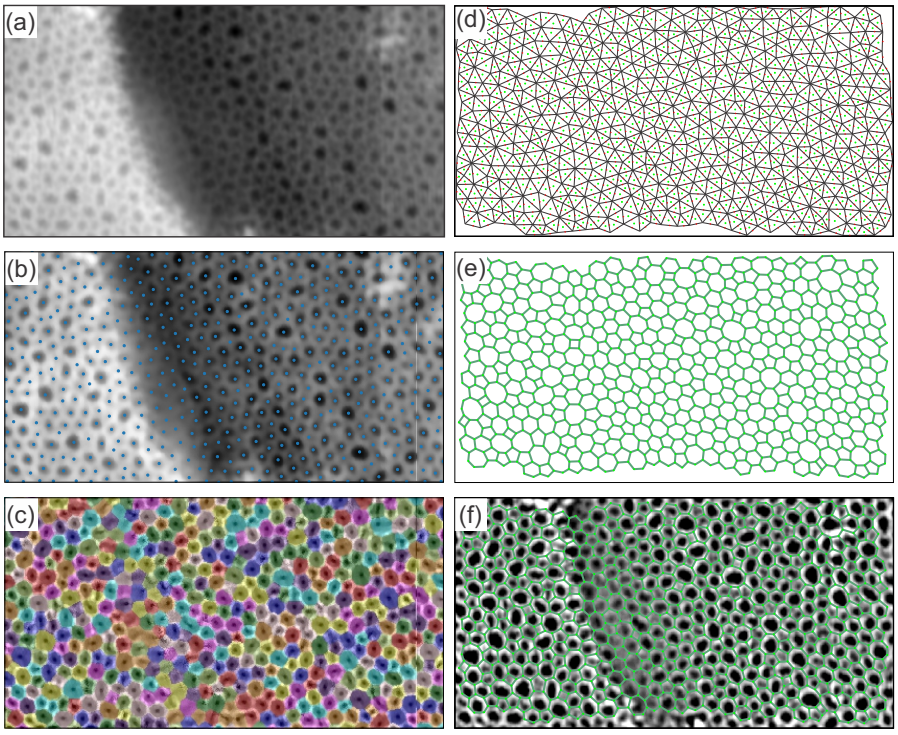

Figure 8.1: Network detection on the silica bilayer across a metal step edge. a) STM image of the silica bilayer across a single Ru(0001) step edge (V_S = 2 V, I_T = 0.4 nA, T = 295 K, scan area = 15.3 nm × 8.1 nm). b) Filtered STM image (denoise, adapthist, equalize) with superimposed detected ring center positions (blue dots). c) Segmented image. d) Deduced RAG edges and calculated atomic positions (silicon: green, oxygen:red). e) Resulting silicon atom network that is superimposed on the STM image in f). Adapted from Ref. [129].

8.1.2 *Structural Analysis Across the Step Edge*

Based on the RAG, the ring size distribution can be extracted by looking at the degree of the nodes, which represents the number of nearest ring neighbors. The resulting ring size distribution is shown in Figure 8.2.

The silica bilayer exhibits 4- to 9-membered rings. The lower graph in Figure 8.2 shows the evolution of ring size distribution across the metal step edge. The white shaded region slides across the image parallel to the substrate step edge. The fraction of the summed areas of every ring size and the total area of rings under the white shaded region are plotted for every position along the perpendicular coordinate x. The fraction of six membered rings (green) represents the crystallinity of the 2D film, as defined in Ref. [79]. Slight deviations in the crystallinity are observed in the vicinity of the step edge.

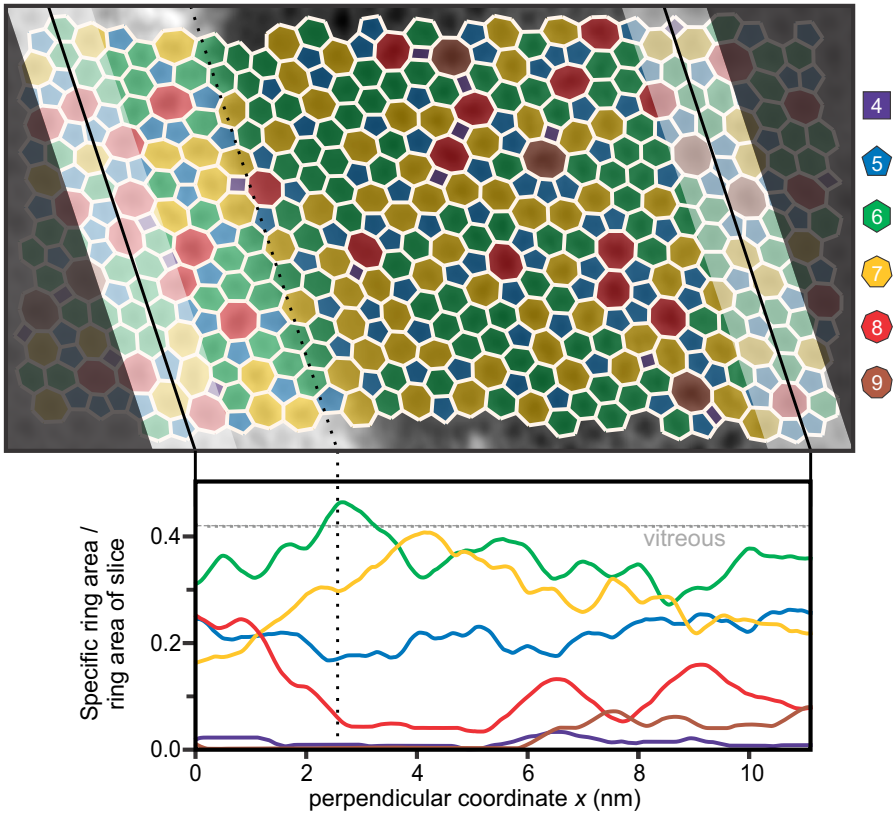

Figure 8.2: Ring size distribution analysis. The detected network is overlaid on the STM image of Figure 8.1a. The rings are color coded according to the ring sizes as provided on the right. The plot at the bottom shows the normalized ring areas of each ring size under the sliding white shaded area. The fraction of 6-membered rings represents the definition of crystallinity in Ref. [79]. The average vitreous crystallinity reported in the literature is indicated with a gray line. [79] Adapted from Ref. [129].

The ring-ring distance analysis is another powerful tool to investigate the structure of the silica film. [81] Figure 8.3 plots the color coded ring-ring distances on top of the STM image and the evolution of ring-ring distances along the perpendicular coordinate x. The determined distances are in agreement with the average ring-ring distance of 0.54 nm in crystalline and vitreous films as reported in literature. [81] The light red area marks the standard deviation of a Gaussian fit

of the ring-ring distances. As obvious from the distance plot, small deviations from the average distance are detected close to the step edge region. On the upper terrace, the ring-ring distances increase slightly, while on the lower terrace they tend to decrease. Compared to the standard deviation this change is minor. However, the change could also be resolved in distance analyses using larger sliding areas and in Si-Si distance analyses. [129]

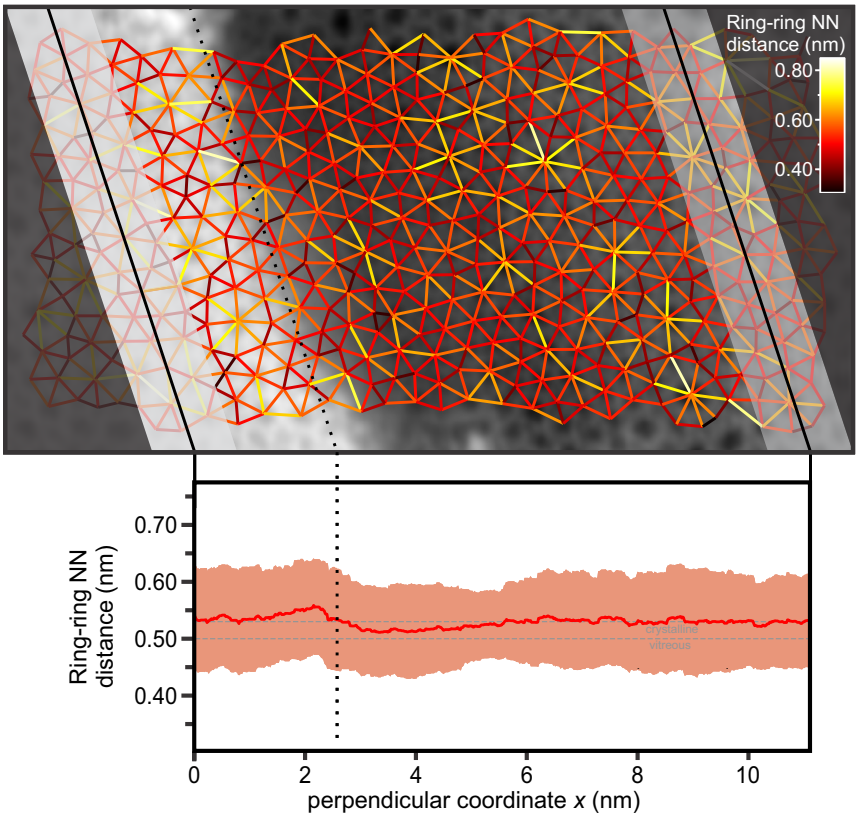

Figure 8.3: Ring-ring distance analysis. The detected ring-ring connections are overlaid on the STM image of Figure 8.1a. The ring-ring distances are color coded according to the color map provided in the right inset. The plot at the bottom shows the evolution of ring-ring distances across the metal step edge. Adapted from Ref. [129].

DFT calculations proposed three models that cover the underlying ruthenium step edge and exhibit unbroken top silica layers. The models include structures that pin to the substrate and carpetlike modes, as discussed in detail in Ref. [129]. Figure 8.4a shows one of the carpetlike mode models. The silica bilayer covers the substrate step edges continuously. We applied the same network tools to analyze the theoretical model and determined the ring-ring distances, as shown in Figure 8.4b. Figure 8.4c plots the ring-ring distances as a function of the perpendicular coordinate x. The scale is the same as in Figure 8.3. At this scale, no deviations can be detected. In the zoomed inset in Figure 8.4c, however, the distances increase on the upper terrace

in the vicinity of the step at 7 nm and decrease at the lower terrace. While further studies are necessary to confirm the observed structural evolution across underlying step edges, we conclude that the crystalline model shows the same qualitative behavior as the vitreous film in Figure 8.3.

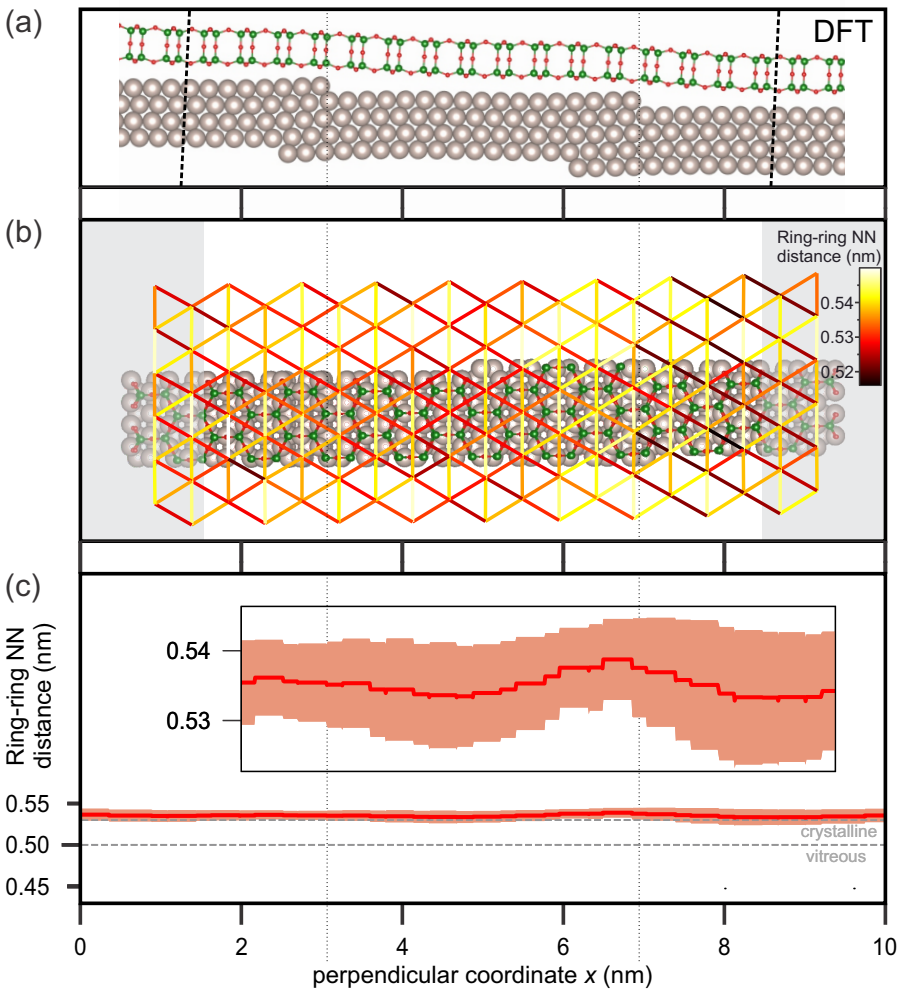

Figure 8.4: Structural analysis of the DFT model. a) Carpetlike mode of the crystalline silica bilayer across the underlying metal step edge. b) Top view of the model with superimposed color coded ring-ring distances. c) Evolution of ring-ring distances as a function of the perpendicular coordinate x. The zoomed inset shows the same qualitative trend as the experimental data in Figure 8.3. Adapted from Ref. [129].

The developed semi-automated network detection revealed the first reported continuous coverage of a vitreous film across a substrate step edge. It enabled the thorough structural analysis of the film crystallinity and of characteristic distances as a function of space. In further studies, it enabled the analysis of larger datasets to study the network structures in the vicinity of mesoscopic scale features. [82, 129] In addition, we successfully applied the network detection tools

to elucidate atomic structures of utrathin germania and silica films. [82, 132, 133]

The network tools have proven to be suitable to detect changes of oxide network structures of large data sets. Large data sets are also created when scanning at high frame rates. In the following sections, the semi-automated network detection is applied to high-speed spiral STM images on thin oxide film systems.

8.2 SPIRAL SCANS ON THIN GERMANIA FILMS

In this section, the spiral scan is applied to an oxide network former that exhibits apart from its crystalline structure, local structural deviations in the form of domain boundaries. In literature, the germania monolayer on Ru(0001) has been studied by DFT, LEED-I/V, and STM. [131] The reported complex boundary structures provide the possibility to evaluate the spiral scan resolution and to apply the semi-automated network detection presented in Section 8.1 to spiral STM images.

8.2.1 *Mesoscopic Features in GeO_2/Ru(0001)*

The germania monolayer film is prepared as described in Chapter 4. The STM image in Figure 8.5a shows the almost completely closed monolayer film. The dark areas are holes that expose the underlying Ru(0001) surface. In connection with these holes, domain boundaries are detected that exhibit deviations of the crystalline hexagonal structure. As discussed in Ref. [131], the boundaries exhibit medium range order and consist of complex ring size combinations.

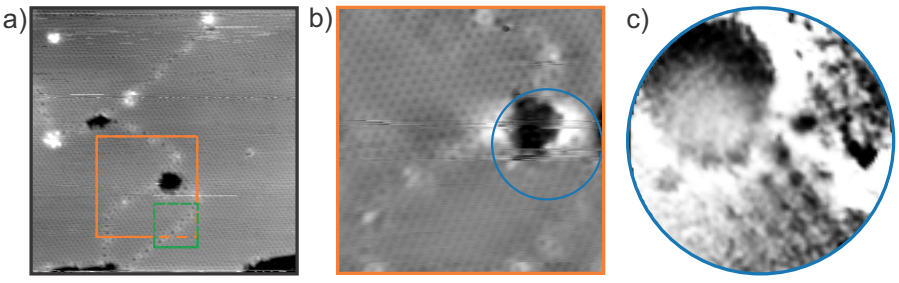

Figure 8.5: STM images of the hexagonal germania monolayer on Ru(0001). a) Conventional large scale STM image revealing mesoscopic holes and domain boundaries, acquired in 153 s (V_S = 1 V, I_T = 1 nA, T = 300 K, scan area = 30 nm × 30 nm). b) Close-up STM image showing the region marked with the orange rectangle in a), acquired in 202 s (V_S = 0.5 V, I_T = 1 nA, T = 300 K, scan area = 12 nm × 12 nm). c) Spiral STM image of the region marked with the blue circle in b), acquired in 50 ms (V_S = 1 V, I_T = 1 nA, T = 300 K, scan diameter = 5 nm).

The area marked with the orange rectangle is shown in the close-up STM image in Figure 8.5b. The hole in the film impedes high resolution STM images. The image contrast is partly blurred. Nevertheless, the hexagonal structure of the film with its line-shaped boundary structures can be identified. The spiral STM image in Figure 8.5c is acquired in 50 ms and shows the area marked with the blue circle in Figure 8.5b. The mesoscopic hole in the monolayer is revealed. On the right and at the bottom of the frame, also the ring structure can be identified. The observed structural features coincide with the conventional scan in Figure 8.5b, which was acquired in 202 s. The fast spiral scan reveals parts of the atomic network structure of the film despite the mesoscopic hole. The clear structural determination of larger areas is, however, not possible based on the current image contrast.

8.2.2 *Domain Boundary Structure of GeO_2/Ru(0001)*

The atomically flat monolayer is now investigated, shifting the scan area slightly as indicated by the green rectangle in Figure 8.5a. Figure 8.6a shows the close-up STM image with the resolved domain boundary, acquired in 113 s. The network analysis in Figure 8.6e reveals a configuration of 5-, 6-, 7-, and 8-membered rings in the lower left of the image. This configuration is reported in the literature as the 5678 complex boundary. [131]

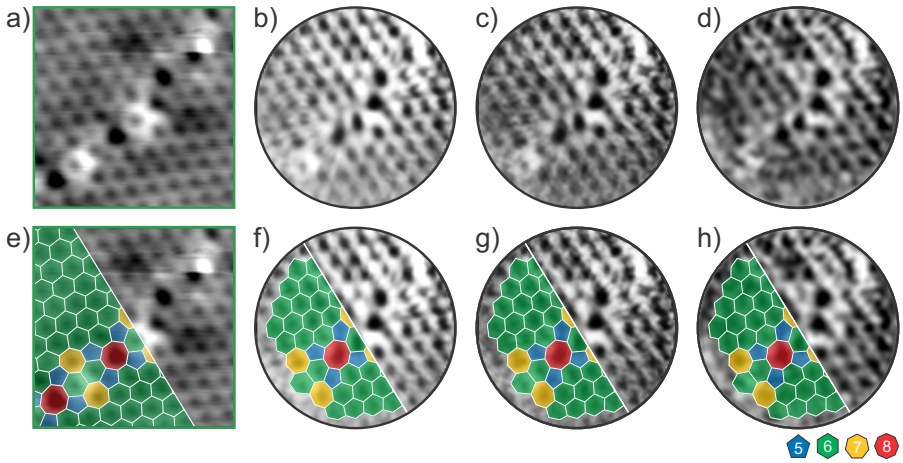

Figure 8.6: Network detection of germania domain boundaries. a) Conventional STM image revealing complex domain boundaries, acquired in 113 s (V_S = 1 V, I_T = 1 nA, T = 300 K, scan area = 5 nm × 5 nm). b) Average of 600 consecutive spiral STM images, acquired in total 30 s. c) Average of 10 consecutive spiral STM images, acquired in total 0.5 s. d) Spiral STM image, acquired in 50 ms, slightly smoothened with a Gaussian filter (V_S = 1 V, I_T = 1 nA, T = 300 K, scan area = 5 nm × 5 nm). The determined ring structures of a-d) are overlaid in e-h), receptively. A complex 5678 domain boundary structure is detected in the lower left of all images.

To investigate the ring structure of the spiral scan, we follow the approach to average consecutive high-speed frames, as introduced in Figure 2.3 in Section 2.1. [26] Figure 8.6b shows the result of 600 averaged spiral scans. Each frame was acquired in 50 ms, resulting in a total acquisition time of 30 s. The images are not corrected for drift nor distortion. Remarkably, the average of 600 images is free of creep and drift artifacts. Figures 8.6a and b show the same scan area with similar image contrast allowing for clear ring identification. The detected ring networks in Figures 8.6e and f exhibit identical ring configurations. Figure 8.6c shows the average of ten consecutive frames of the same data set and Figure 8.6d shows a single frame acquired in 50 ms. For visualization, the single frame in Figure 8.6d is slightly smoothened with a Gaussian filter. All images show the same scan area with similar resolved features. However, for the single frame the network detection is challenging, especially close to the rim. In the central region, on the other hand, the apparent larger rings of the domain boundary can be easily identified. The overlaid network structure in Figures 8.6f,g, and h show that for both averaged and single frames the ring assignment is the same.

While the detection of atomic positions in oxygen adlayers was possible throughout the whole scan area as described in Chapter 7, a clear assignment of the oxide network ring structures towards the rim region shown in Fig. 8.6d is challenging. The reduced image contrast towards the rim of the image is most likely due to the decreased data point density towards the rim of the CAV Archimedean spiral geometry, as discussed in Section 6.3. Figure 8.6 shows that this low point density can be compensated by averaging a small number of individual frames. Individual frames still exhibit a high resolution in the center and are favorable compared to the CLV mode, as discussed in Section 6.3. Therefore, in this work the CAV Archmiedean spiral is applied to investigate oxide network structures.

Complex domain boundaries are resolved in short time with the spiral scan. To verify that the high-speed scan provides a reliable image contrast of these ring structures and that changes in the configuration can be detected, the position of the STM tip was changed intentionally during the high-speed scan. The resulting images before and after the tip displacement are shown in Figures 8.7a,b, respectively. Characteristic ring formations are detectable and the bright ring feature highlighted with the dotted orange circle can be used as reference point to determine the shift of the scan area. The resulting displacement vector is drawn as orange arrow in Figure 8.7c. Since the tip was moved intentionally in this direction, this lateral displacement was expected. It is worth noting that the images after the tip displacement are free of creep and drift artifacts. The scan area changed abruptly while displacing the STM tip without affecting the image resolution.

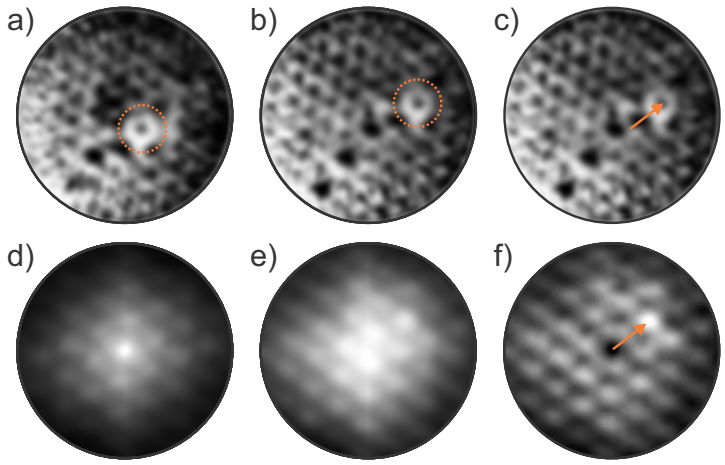

Figure 8.7: Detection of lateral displacement of the scan area. a-c) Spiral STM images, acquired in 50 ms (V_S = 1 V, I_T = 1 nA, T = 300 K, scan area = 5 nm × 5 nm). The STM tip was moved intentionally between a) and b). The bright ring highlighted in orange serves as reference point to determine the displacement vector, which is represented by the orange arrow in c). d) Self-correlation of a) before the tip was moved. e) Cross correlation of a) and b). f) Difference of d) and e). The displacement vector (orange arrow) can be clearly identified and agrees with the vector in c).

Another approach to determine the displacement vector is to look at the intensity maximum of the cross correlation of the two images. Figure 8.7d shows the self-correlation of Figure 8.7a. The resulting pattern shows the hexagonal structure of the germania ML with the maximum intensity in the origin. Figure 8.7e shows the cross correlation of frames a and b. Due to the hexagonal structure in the images, the identification of the intensity maximum that determines the displacement vector is ambiguous. To compensate for the periodic structure, the self-correlation of Figure 8.7d is subtracted from the cross correlation in Figure 8.7e. The resulting image in Figure 8.7f shows a clear intensity maximum. The displacement vector represented by the orange arrow agrees with the one in Figure 8.7c.

The experiment of intentionally displacing the scanning STM tip during high-speed measurements showed that the image contrast of the ring structures is reliable and that changes in the network structure can be identified. In the presented case, the change consists of a lateral displacement.

The experiment of artificially displacing the tip is similar to thermal drift artifacts that may occur during high temperature measurements. We provided two exemplary methods how these artifacts could be corrected in high-speed spiral STM measurements.

8.2.3 *Changing Image Contrast in Spiral Scans on GeO_2/Ru(0001)*

The examples above show that single frames and images averaged over several frames resemble the image contrast of conventional STM measurements on the germania ML on Ru(0001). The question arises, whether individual frames acquired in short times of 50 ms also deviate from this image contrast. Figure 8.8 shows examples of the same scan sequence that was used to extract Figures 8.6 and 8.7. The displayed time is the acquisition time extracted from the real time operating system.

Figures 8.8a-c are acquired at the same position as Figure 8.7a. In the central region marked with the orange circle, the same ring configuration is observed for all three frames. From Figure 8.8a to b, the local image contrast inside the orange circle changes. The ring structure in the top right of the circled area is resolved more clearly and the apparent bright ring is more extended. The change in image contrast might be related to small fluctuations in or underneath the film system. However, the changes are very small and can also be caused by minor instabilities of the scan setup, e.g. by variations of the tip apex.

Figures 8.8d-i are acquired at the same position as Figure 8.7b. The blue circle highlights the region of interest. For visualization, the image contrast is adjusted in the magnified insets. In the inset of Figure 8.8e, a protrusion on the upper right corner becomes visible. This protrusion increases its intensity in Figure 8.8f and changes its position towards the bottom of the blue circle. In the inset of Figure 8.8g, only at the bottom a region of slightly increased intensity can be detected, while the upper region is dark. In the consecutive frame in Figure 8.8h, the protrusion vanished almost completely and the image contrast is similar to the one in Figure 8.8d. Remarkably, a few seconds later in Figure 8.8i the dynamically appearing protrusion is detected at the same lateral position as in Figures 8.8e,f. This observation indicates that the change in image contrast can relate to the germania film and its local structure. The effect of bright ring features can stem from electronic contributions or local deviations in the network structure. [131] In the case of Figure 8.8 reversible changes over time of this effect are observed. The observed feature propagates from Figure 8.8e to Figure 8.8g in the counter scan direction. Therefore, this effect is not related to tip artifacts but may be caused by dynamics inside, underneath or on top of the film. In Chapter 7, dynamic oxygen species in various adlayer formations on Ru(0001) are reported at room temperature. These species may also be mobile to a certain extent between the film and the substrate causing the observed change in the image contrast. Further possible explanations include adsorbate dynamics on top of the monolayer film. STM studies of diffusing species, such as oxygen, on other oxide surfaces are reported in literature. [136–138]

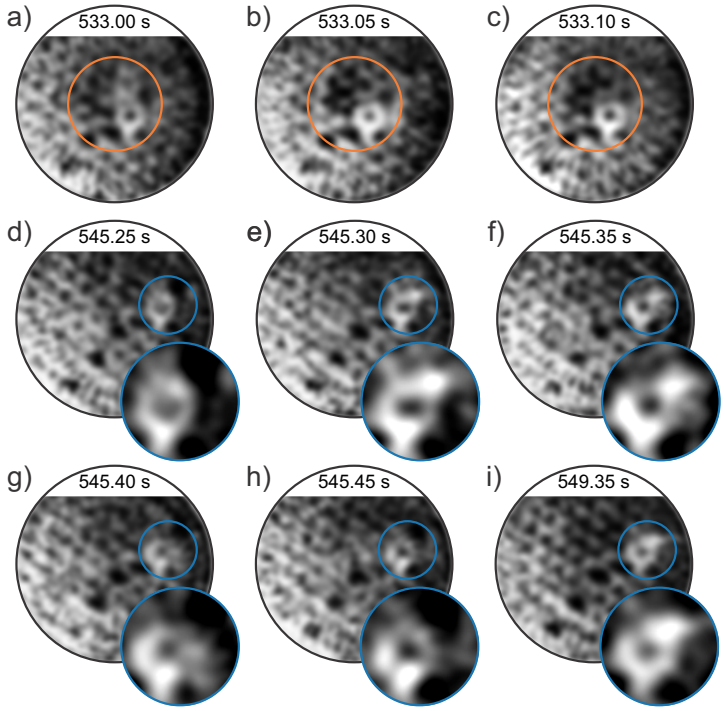

Figure 8.8: Dynamic changes of the image contrast on the germania monolayer. Spiral STM images, acquired in 50 ms (V_S = 1 V, I_T = 1 nA, T = 300 K, scan area = 5 nm × 5 nm). a-c) Same scan area as in Figure 8.7a. The image contrast in the central region marked with the orange circle changes over time. d-i) Same scan area as in Figure 8.7b. The image contrast in the blue circle changes over time. An evolving protrusion can be identified in e) in the upper right section of the blue circle. This protrusion moves to the bottom in g) and shows a decreased intensity in h). A few seconds later in i), a protrusion is detected at the same lateral position as in e,f).

The field of adsorbate dynamics on oxide surfaces is an important field and future studies may include the investigation of different adsorbates and their dynamics on ultrathin oxide film systems.

8.3 HIGH-SPEED STM MEASUREMENTS ON SILICA ON RU(0001)

The thin oxide film system SiO_2/Ru(0001) exhibits versatile polymorphs, namely the monolayer phase, the zigzag phase, and the bilayer phase. The silica bilayer can be crystalline or vitreous. The atomic structure of these phases has been studied intensively during the last decade making the silica film supported on ruthenium the most thoroughly investigated thin oxide network system.

In this section, the silica bilayer on Ru(0001) is investigated using high-speed spiral STM. At the end of this section, high-speed STM measurements at elevated temperatures are presented that provide an outlook for future studies.

8.3.1 *Silica Polymorphs on Ru(0001)*

In Section 8.2 the monolayer phase of germanina on Ru(0001) is discussed. Silica exhibits in addition to this hexagonal monolayer phase other polymorphs that are stable at room temperature on Ru(0001), namely the zigzag phase and the bilayer phase, which can be crystalline or vitreous.

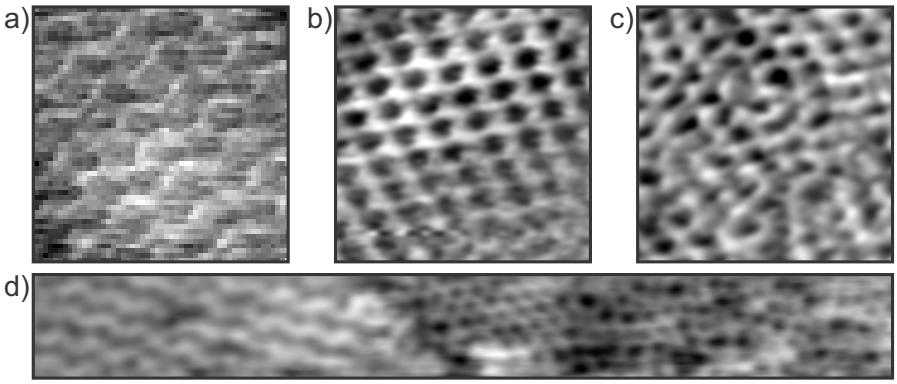

Figure 8.9: STM images of zigzag and bilayer phases on Ru(0001). a) STM image on the silica zigzag phase (V_S = 1 V, I_T = 1.2 nA, T = 300 K, scan area = 4 nm × 4 nm). b) STM image on the crystalline silica bilayer (V_S = 1.5 V, I_T = 1.2 nA, T = 300 K, scan area = 4 nm × 4 nm). c) STM image on the vitreous silica bilayer (V_S = 1 V, I_T = 1.2 nA, T = 300 K, scan area = 4 nm × 4 nm). d) STM image of the coexisting phases shown in a-c). (V_S = 1 V, I_T = 1.2 nA, T = 300 K, scan area = 3 nm × 25 nm).

Figure 8.9a shows a room temperature STM image of the zigzag phase, which is considered as an intermediate phase during the growth process of the silica bilayer. [83] Figures 8.9b,c show the bilayer in its crystalline and vitreous form, respectively. As obvious from Figure 8.9d, these three phases can coexist on the same sample. Those regions of coexisting phases are interesting due to their atomic structural arrangement. [82] These interfaces may play an important role for dynamic processes within the film system, underneath the film, or on top of the film. In the following sections, the silica bilayer of this preparation is analyzed with high-speed spiral STM.

8.3.2 *Spiral Scans on the Silica Bilayer*

The silica bilayer in Figure 8.10a shows coexisting crystalline and vitreous domains. First, crystalline patches of the silica bilayer on Ru(0001) are studied. Figure 8.10b shows the magnified region marked with the blue square in Figure 8.10b. With the network detection tool presented in Section 8.1, six-membered rings are identified that form the periodic hexagonal lattice as drawn with green hexagons. Figures 8.10c,d show corresponding spiral STM images of crystalline silica

bilayer patches. In analogy to Figure 8.6c in Section 8.2, Figure 8.10c is the averaged image of ten consecutive frames, each acquired in 50 ms. Figures 8.10d shows an individual frame. In both images, especially in the center of the images, the resolution allows us to assign individual rings and to identify the hexagonal oxide network structure.

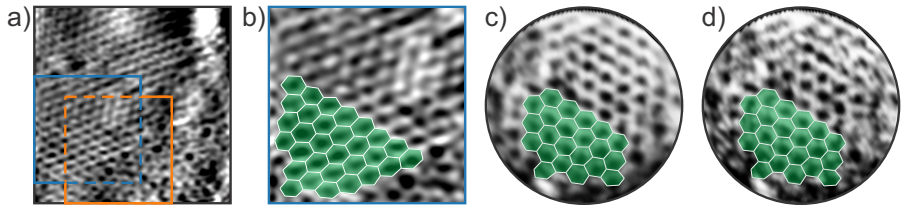

Figure 8.10: STM images of crystalline silica bilayer patches on Ru(0001). a) Conventional STM image, acquired in 262 s (V_S = 1.6 V, I_T = 1 nA, T = 300 K, scan area = 9.2 nm × 9.2 nm). b) Magnified region of 5 nm × 5 nm marked with the blue square in a). c) Average of 10 consecutive spiral STM images, acquired in total 0.5 s. d) Spiral STM image, acquired in 50 ms (V_S = 1.6 V, I_T = 1 nA, T = 300 K, scan area = 5 nm × 5 nm). Detected six-membered rings are overlaid with green hexagons in b-c). b,c) Adapted from Ref. [139] licensed under a Creative Commons Attribution (CC BY) license.

The region highlighted with the orange square in Figure 8.10a contains a more vitreous area of the silica film. Figure 8.11a shows the magnified scan field. As indicated by the white dotted and dashed lines, two crystalline domains with different orientations, rotated by 30° are identified. Different orientations of the bilayer film with respect to the substrate are reported in literature. [130] Figure 8.11b shows the averaged image of 20 consecutive spiral frames. As indicated by the dotted and dashed white lines, the same orientations of the crystalline domains are identified. However, the identification of the local ring configurations between these two domains is ambiguous. Despite averaging 20 consecutive frames, which results in a summed acquisition time of 1 s, the image contrast in Figure 8.11b is slightly fuzzy in certain areas. The question arises why achieving ring resolution in these areas is so challenging.

Figures 8.11c and d show individual consecutive spiral frames acquired in 50 ms. They allow to identify a great number of individual rings, as highlighted with white dotted ellipses. Comparing these highlighted areas in the two frames, it becomes obvious that the great majority of resolved rings remains constant over time. However, the image contrast of the ring marked in green changes significantly from Figure 8.11c to d.

Changes in the image contrast resulting in varying ring resolutions are observed frequently in high-speed scans on the silica bilayer on Ru(0001). Figure 8.12 provides two additional examples of this effect. The dotted white ellipses illustrate that the same ring features can

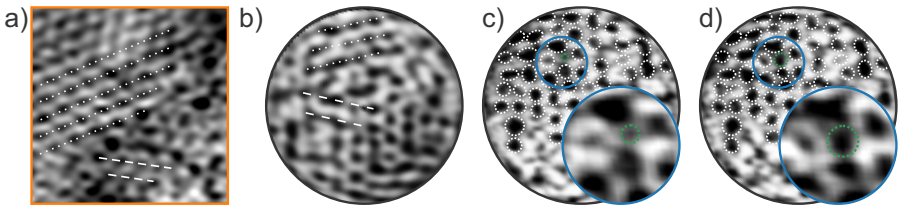

Figure 8.11: STM images of vitreous silica bilayer patches on Ru(0001). a) Magnified region of 5 nm × 5 nm marked with the orange square in Figure 8.10 a). Vitreous and crystalline regions are detected. The orientation of two crystalline domains is highlighted exemplarily. b) Average of 20 consecutive spiral STM images, acquired in total 1 s. The same domain orientations as in a) are highlighted with white lines. c,d) Consecutive spiral STM image, acquired in 50 ms (V_S = 1.6 V, I_T = 1 nA, T = 300 K, scan area = 5 nm × 5 nm). Similar ring configurations in c) and d) are highlighted exemplarily with white dotted ellipses. The magnified insets in the blue frames show a change in the ring contrast, as indicated with green dotted circles. a,b) Adapted from Ref. [139] licensed under a Creative Commons Attribution (CC BY) license.

be identified in the consecutive spiral STM images. Small changes in the imaging contrast are marked with black arrows. Images without overlaid features are provided in the Appendix. The areas marked with blue circles are magnified in Figures 8.12e-h. For visualization, the image contrast is adjusted. Three adjacent rings are identified labeled with 1, 2, and 3. In Figure 8.12f, ring 2 exhibits a triangular-like shape facing to the lower left and the connection to ring 3 is faint. in contrast to this, Figure 8.12g shows that the triangular shape of ring 2 faces to the top left and the connection to ring 3 at the lower left is more pronounced. At the same time, ring 1 appears more elongated and the interconnection between ring 1 and ring 3 is less pronounced. In the consecutive frame in Figure 8.12h, the image contrast is again similar to the one in Figure 8.12e. The appearance of individual rings and of their interconnections changes from frame to frame.

The image sequence in Figures 8.12i-l provides another example of dynamic contrast changes during high-speed STM measurements. The ring of interest is marked with the dotted green ellipse. For visualization, the regions of interest are magnified in Figures 8.12m-p. From Figure 8.12m to n, the apparent ring size increases. In Figure 8.12, the apparent size of the ring shrinks considerably and the right part of the ring that was faint in the previous frames is now more pronounced. Then, in Figure 8.12p the apparent shape of the ring is similar to the one in Figure 8.12n. The ring shows frequent variations in its apparent ring size as a function of time.

Throughout the scans, the effects of dynamic contrast changes are frequently observed. These changes are more pronounced than the local fluctuations observed on the germania monolayer described in Section 8.2. Two effects are reported in literature that may relate

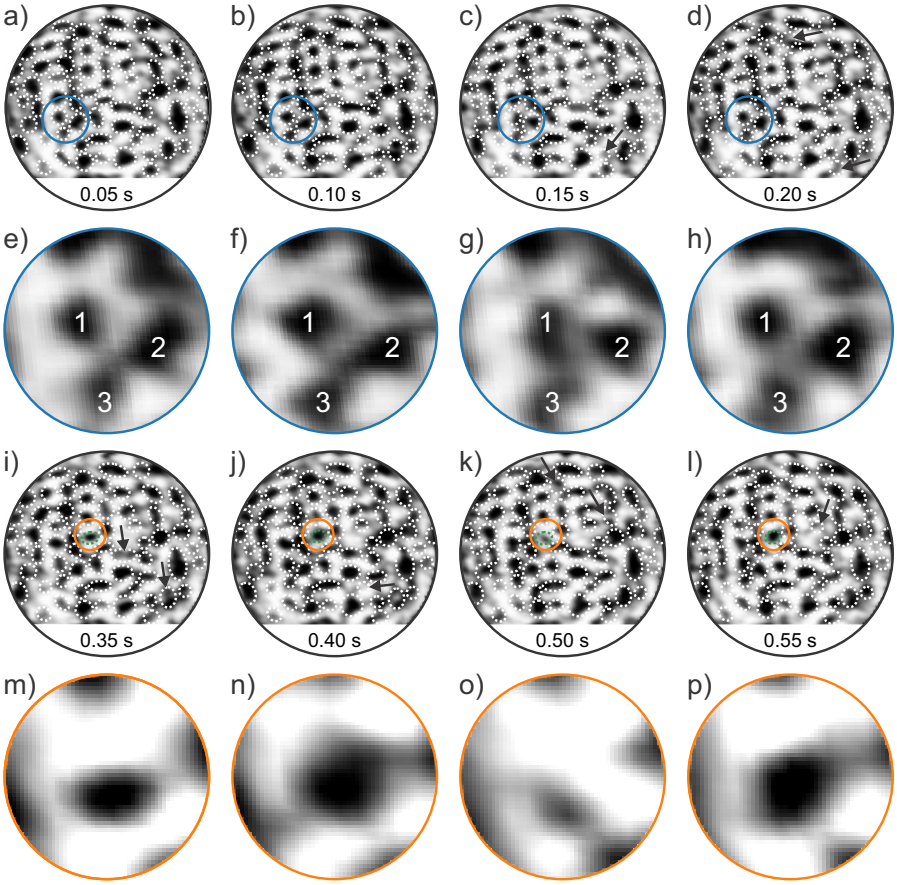

Figure 8.12: Dynamic changes in the image contrast on silica on Ru(0001). a-d), i-l) Spiral STM images on the silica bilayer on Ru(0001), acquired in 50 ms (V_S = 0.8 V, I_T = 1 nA, T = 300 K, scan area = 5 nm × 5 nm). The time is indicated at the bottom of each frame. Rings detected in every frame are overlaid with dotted white ellipses. Black arrows indicate small local changes in the image contrast. Regions of interest highlighted in blue and orange are magnified in e-h) and m-p), respectively. e-h) Dynamic changes of the appearance of the rings labeled with 1, 2, 3 and of their interconnections are resolved. m-p) Dynamic changes of the apparent ring size are resolved. Adapted from Ref. [140].

to the observed effects. Changes in the local image contrast are reported by Altman et al. [141]. The silica bilayer on Pt shows differently pronounced ring features depending on the applied sample voltage. Figure 8.13 shows that the bond between the two adjacent rings in the yellow frame varies in intensity as a function of the sample voltage. Other areas that show similar behavior are indicated with white arrows. It is worth noting that the effect is not observed for every ring configuration in the image. Furthermore, it is reported that in the tunneling current range between 0.1 and 0.55 nA the image contrast did not change noticeably. [141]

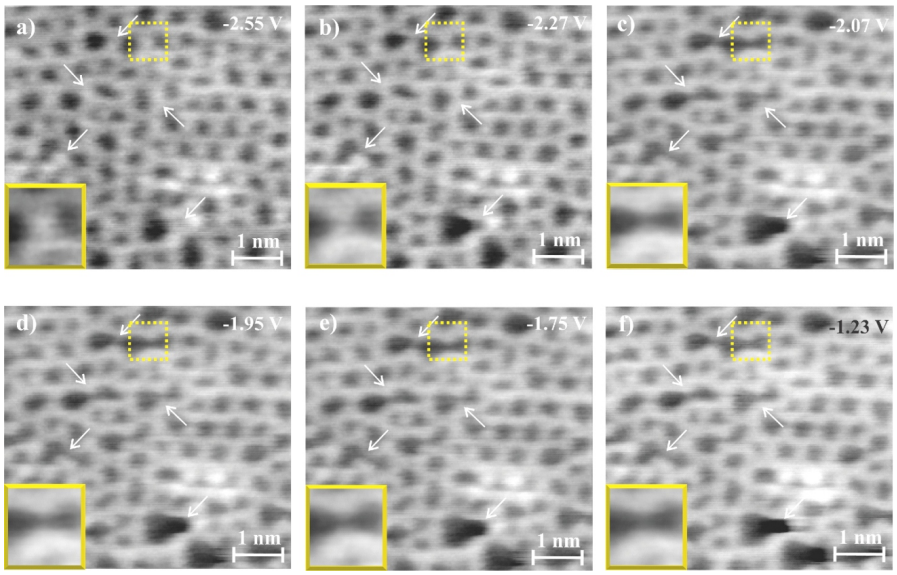

Figure 8.13: Sample voltage affects STM image contrast on silica. STM image series of the vitreous silica bilayer, each acquired in 6.7 s. The sample voltage was varied as shown in the upper right of the images. Arrows highlight locations with local image contrast changes. The yellow outlined insets show the magnified region of a fading connection between two adjacent rings. Reproduced from Ref. [141]. Copyright 2014 Wiley-VCH Verlag GmbH & Co. KGaA, Weinheim.

The reported phenomena of intensity variations in Figure 8.13 are similar to the observed dynamic changes of apparent ring sizes and ring interconnections shown in Figures 8.11 and 8.12. While the measurements shown in Figure 8.13 are recorded with a tungsten tip on silica on platinum in constant current mode, we measure with a PtIr tip on silica on ruthenium in quasi-constant height mode with the spiral STM. In the quasi-constant height mode, the tip-sample distance may vary to a certain extent resulting in similar changes of the local electric field as variations of the sample voltage can cause.

As a result of the frequently changing image contrast, the averaged images exhibit blurred regions as shown in Figure 8.11b. The second effect reported in literature that shows changes of local image contrast is in the context of structural changes induced by the electron beam of high-resolution TEM measurements. [91] During the TEM measurements, local atom displacements are detected. The direction and the length of the displacement vectors of the atoms depend on their lateral spatial coordinates. As indicated with white ellipses in Figure 8.14, blurry regions are observed. While the blurred regions in the TEM measurements in Figure 8.14 are related to beam induced structural changes in the silica network, we would not expect structural changes at room temperature of the van der Waals bound silica film on Ru(0001) when measuring with STM since experimentally and

theoretically determined activation barriers for structural changes in the silica bilayer are 4.2 and 4.3 eV, respectively. [90]

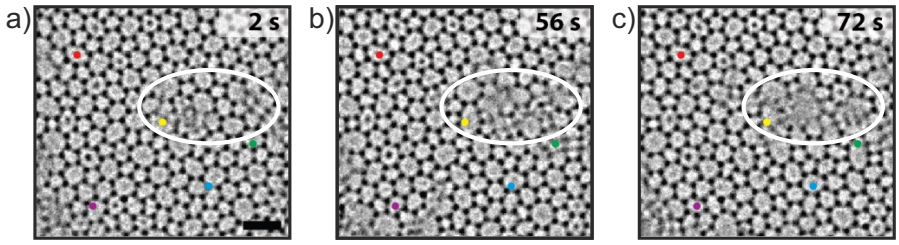

Figure 8.14: High-resolution TEM images on silica. The images show the silica bilayer film at a) t=2 s, b), t=56 s, c) t=72 s (recalibrated image size = 5 nm × 5.5 nm). The area of interest that shows a blurred image contrast is outlined in white. From Ref. [91]. Reprinted with permission from AAAS.

At room temperature, supported oxide thin films can be subject to other dynamic processes such as adsorbate diffusion or mobile interfacial species, as discussed in Section 8.2. Therefore, the high-speed scans on the silica bilayer are analyzed with the focus on dynamic changes of the local image contrast that are consistent over time. The upper row of Figure 8.15 shows four consecutive spiral STM images, each acquired in 50 ms. As indicated by the dotted white ellipses, the same ring features are identified in the images. The region circled in blue is magnified in Figures 8.15e-h. In Figures 8.15e,f, the ring circled in orange appears very bright. The same area appears less intense in the consecutive frames in Figures 8.15g,h. At the same time when the intensity of the orange area decreases, the ring circled in green appears very bright. The bright area changes its lateral position from Figure 8.15f to g within 50 ms. The lateral displacement of this bright area is only observed in this direction. The frames before and after this displacement show consistently similar image contrasts in this particular region. This evolution of the image contrast over time is comparable to the oxygen diffusion processes described in Chapter 7. For insulating bilayer and trilayer films, contributions from the underlying metal substrate to the STM image contrast are reported in literature. [142, 143] Therefore, the observed lateral displacement of the bright feature may be related to mobile interfacial oxygen atoms.

Looking at the bright rings circled in orange and green in Figure 8.15, it becomes obvious that they exhibit rather a crescent shape. This characteristic crescent shape was observed in studies of metal atom adsorption on silica films supported on Ru(0001). [144] The studies suggested that metal species are not fixed at the measurement temperature of 5 K and that they adsorb below the atomic surface of the film. At room temperature, adsorbed species are more mobile and a diffusion event on, in or under the film system can explain the observed lateral displacement of the bright feature in Figure 8.15.

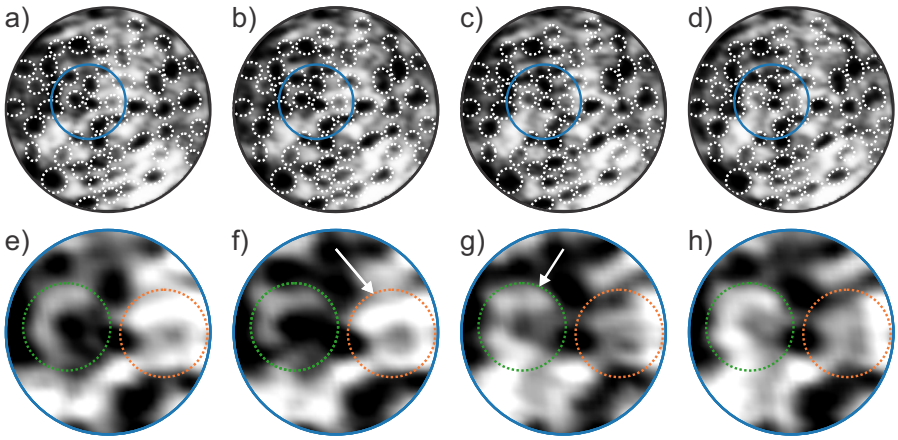

Figure 8.15: Dynamic lateral displacement of a bright ring feature. a-d) Consecutive spiral STM images on the silica bilayer on Ru(0001), acquired in 50 ms (V_S = 0.8 V, I_T = 1 nA, T = 300 K, scan area = 5 nm × 5 nm). Consistent ring features are marked with dotted white ellipses. The lateral displacement of a region with bright image contrast is detected, as shown in the zoomed images in e-h) (1.8 nm × 1.8 nm). The region of interest is highlighted in orange in f) and in green in g).

In the following example, we focus on how apparent ring shapes change over time. The images in 8.16 are extracted from the same measurement as Figure 8.12 and the displayed times in the two Figures relate to each other. White dotted ellipses mark the ring features that can be consistently detected in all frames. The ring configuration magnified in Figure 8.16e is clearly resolved. The apparent ring arrangement changes from Figure 8.16e to f. As obvious from Figure 8.16g, this changed ring contrast is also detected in the consecutive frame. This consistency and the fact that other ring features in the individual images remain unchanged provide evidence that the observed image contrast is not related to noise artifacts during the measurement. These observations indicate that the change in ring contrast is most likely based on effects related to the sample system.

As discussed above, mobile oxygen species at the interface may contribute to dynamic contrast changes. In a recent publication, the presence of defect Si particles in silica is discussed. [145] In this context, dangling O particles are also considered. The presence of such defects and dangling bonds that can interact with interfacial oxygen or the underlying metal substrate may have similar effects on the STM imaging contrast as observed in Figure 8.16.

The zigzag silica polymorph exhibits Si-O bonds to the metal substrate. In fact, Figures 8.16f,g are comparable to the characteristic STM image contrast of this zigzag phase. [83] Proposed intermediate structures with elongated rings in one of the layers formed during structural changes in the silica film could also explain the observed image contrast. [90] To form the zigzag phase and the metastable

structures proposed in Ref. [90], breaking and making of Si-O bonds would be required. As discussed above, the activation barrier for complete structural changes is too high to expect them to occur at room temperature. [90] However, as obvious from the theoretical calculations in Ref. [90], intermediate structures resulting from the vitreous state exhibit lower activation barriers in the order of 1 to 2 eV. The lower activation barriers for breaking the Si-O bond is explained with an electron transfer between the silica bilayer and the Ru substrate. [90] Considering the lower activation energies based on charge redistribution and that due to electron tunneling in STM measurements, an electron exchange between film and substrate may be promoted, certain structural reformations in the supported silica film might be possible at room temperature.

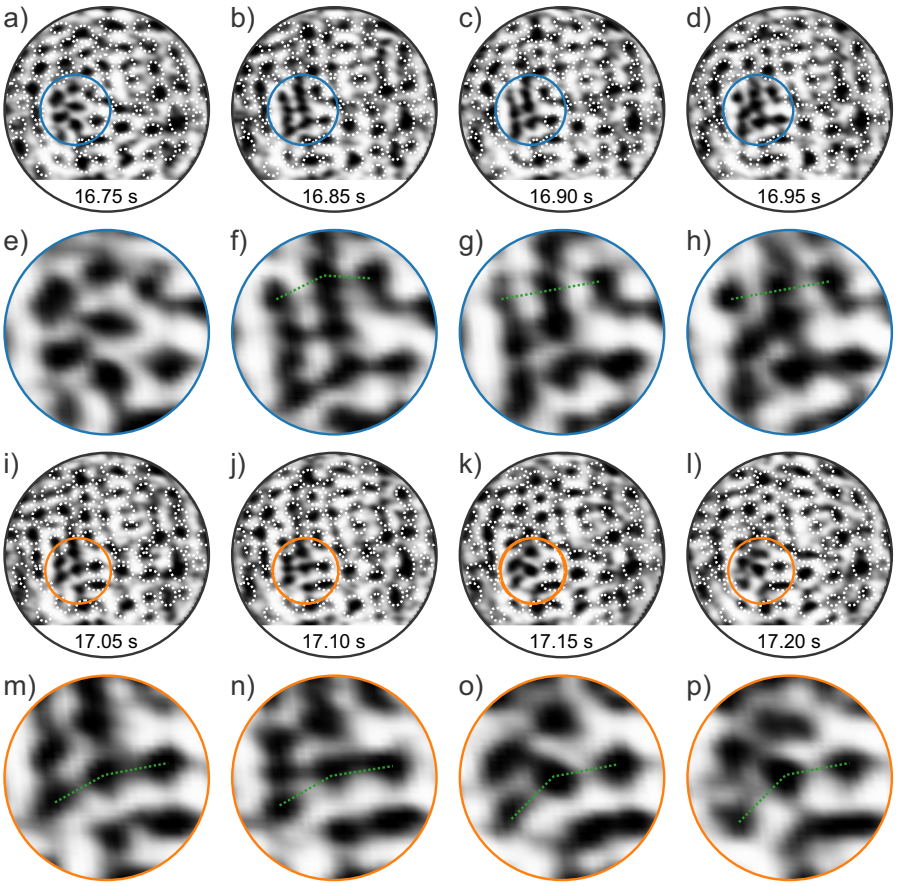

Figure 8.16: Dynamic changes of the ring contrast. a-d), i-l) Spiral STM images on the silica bilayer on Ru(0001), acquired in 50 ms (V_S = 0.8 V, I_T = 1 nA, T = 300 K, scan area = 5 nm × 5 nm). The time is indicated at the bottom of each frame. Rings detected in every frame are overlaid with dotted white ellipses. Regions of interest highlighted in blue and orange are magnified in e-h) and m-p), respectively. Consistent changes of the apparent ring configuration are detected. The dotted green lines serve as guide to the eye to evaluate the ring alignment. Adapted from Ref. [140].

In conventional STM measurements shown in Figures 8.9, 8.10, and 8.11, the tip scans across a silica ring in 0.03 s to 0.12 s. The time required to image an entire silica ring is in the order of 10 to 100 s. In the high-speed spiral STM images presented in Figure 8.16, the time to scan across an individual ring is 0.02 ms and the entire ring is imaged in approximately 5 ms. Comparing these timescales, the potential of high-speed measurements to capture events that are averaged in conventional STM measurements becomes obvious.

In Figure 8.16h, the ring contrast is partly reversed and resembles rather the one in Figure 8.16e. Comparing these two frames in Figures 8.16e,h, a similar overall ring arrangement is detected. On closer inspection, it becomes obvious that the ring interconnections in Figure 8.16h are less pronounced than in Figure 8.16e. In addition, the ring alignment indicated with the dotted green line is straight in Figure 8.16h, while the rings are aligned in an angle of approximately 130° in Figure 8.16e. The alignment of the rings seems to change over time.

Similar effects of changing apparent ring arrangements are observed shortly after, as shown in Figures 8.16m-p. The ring contrast changes significantly from Figure 8.16m to n. In the consecutive frames in Figures 8.16o and p, the position of the lower left ring changes slightly towards the bottom. This change results in a different ring alignment in analogy to Figures 8.16e-h, as indicated by the dotted green lines. In these examples, not only the apparent ring sizes and ring shapes vary over time, but the ring contrast is subject to significant dynamic changes.

In summary, high-speed STM revealed versatile dynamic effects on the silica bilayer on Ru(0001). Dynamic processes on top of the film system or underneath the film can contribute to these phenomena. Dynamic processes underneath the silica film are closely related to the observed mobile oxygen species in dense oxygen adlayers discussed in Chapter 7. Although breaking and making of chemical Si-O bonds is only expected at elevated temperatures, dynamic processes inside the film systems should be considered to explain the observed effects at room temperature.

Interesting future studies to investigate the behavior of these thermally activated processes will consist of high-speed measurements at elevated temperatures. The following Section 8.3.3 provides first STM measurements on the silica film on Ru(0001) at elevated temperatures and concludes with an outlook on future research.

8.3.3 *First Attempts: High-Speed STM on Silica at Elevated Temperatures*

As shown in Section 8.3.2, the image contrast during high-speed scans on the silica bilayer varies over time. At elevated temperatures, rapid changes of the imaging conditions, especially the condition of the tip apex, are expected. In preparation for these circumstances, room

temperature measurements are performed with imaging conditions that are not ideal. Figure 8.17a shows the resulting STM image of such a measurement. Silica bilayer film patches can be identified. However, the conventional STM image shows numerous protrusions and line artifacts in the fast scan direction impeding atomic network resolution.

The high-speed spiral STM images in Figures 8.17b-d are acquired with the same imaging conditions and reveal the network structure of the silica bilayer. It is worth noting that this improved image contrast occurred temporarily many times during the data acquisition. The improved image contrast was observed for image sequences in the order of 2 to 20 frames, which corresponds to 0.13 - 1.3 s. For instance, Figures 8.17c,d show two consecutive frames that reveal the network structure. As indicated with white ellipses in Figure 8.17d, the film exhibits dark mesoscopic features that measure approximately 1.5 nm in diameter.

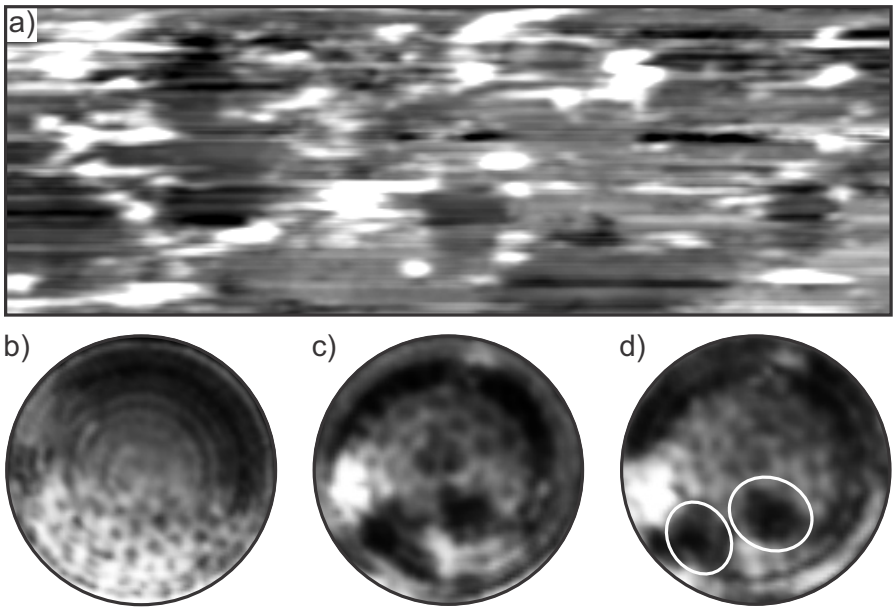

Figure 8.17: Temporary improvement of image contrast in high-speed scans. a) Conventional STM image acquired in constant current mode on the silica bilayer on Ru(0001) (scan area = 130 nm × 130 nm, acquisition time = 7 min). The imaging conditions, i.e. the tip condition is not ideal. b) Spiral STM image in quasi-constant height mode revealing the oxide network structure (scan diameter = 6 nm, acquisition time = 57 ms). c,d) Consecutive spiral STM images in quasi-constant height mode revealing the oxide network structure and mesoscopic dark features marked with white ellipses (scan diameter = 5 nm, acquisition time = 46 ms) Scan parameters for all images: V_S = 2.6 V, I_T = 0.7 nA, T = 300 K.

Figure 8.17 shows the potential of the high-speed scans to resolve atomic structures with poorly conditioned tips. In addition to rapidly changing imaging conditions, at elevated temperatures, thermal drift

is expected to be a major challenge. As discussed in Chapter 5, the STM body and the sample holder are designed rigid, compact, and highly symmetric to ensure low thermal drift. The uncorrected room temperature measurements presented in Chapters 6 and 7 prove how effective the mechanical design is in terms of thermal stability.

Figure 8.18 shows the same silica bilayer film as shown in Figure 8.9, measured at 600 K. The overview area in Figure 8.18a was scanned for more than 7 hours without correcting the lateral position of the STM tip. The area highlighted with the white dotted rectangle is shown in a closeup view in Figures 8.18b,d,f. The characteristic shape of the silica film patch can be identified in all three images that are acquired over several hours.

The vertical line artifacts in the images and the side-by-side comparison of the STM images reveal that the imaging contrast changes frequently over time. Especially from Figure 8.18b to Figure 8.18d the change in image contrast is very pronounced. Figure 8.18b shows a fine structure that was observed several times during scanning. A supplementary figure in the Appendix shows scans at additional acquisition times. For visualization, the fine structure in the dashed white rectangle is magnified in Figure 8.18c. Within this fine structure, dark areas are identified as highlighted with black circles. The diameters range from 1 to 6 nm. The fine structure is not observed in Figures 8.18d-g.

Additional changes in the image contrast are observed comparing Figures 8.18b and d. The features marked with white ellipses appear as depressions in Figure 8.18b while they appear as protrusions in Figure 8.18d. The overall silica terrace still appears bright. The contrast inversion is only observed locally in the two discrete regions marked with white ellipses. This local contrast inversion and the resolved fine structure can indicate that not only the top silica layer is imaged. In literature, STM measurements are reported that reveal sublayer structures of oxide films depending on the scan parameters and sample temperatures [22, 146]. Contributions from the metal substrate to the STM image contrast are observed for graphene [147] and insulating bi- and trilayer films. [142, 143] In Figure 8.18 contributions from the Ru metal substrate and the interfacial oxygen layers may be the reason for the observed fine structure. Future parameter studies at different sample voltages and tunneling currents are necessary to fully understand the observed effects of local image contrast inversion and the resolved fine structure.

Figure 8.18 demonstrates that the microscope can be operated at elevated temperatures without drift and distortion corrections. To evaluate the dynamics of the sample system at elevated temperature, the consecutive conventional STM images in Figure 8.18 with similar image contrasts are compared. The overall shape of the silica film patch does not change over time. However, from Figure 8.18d to

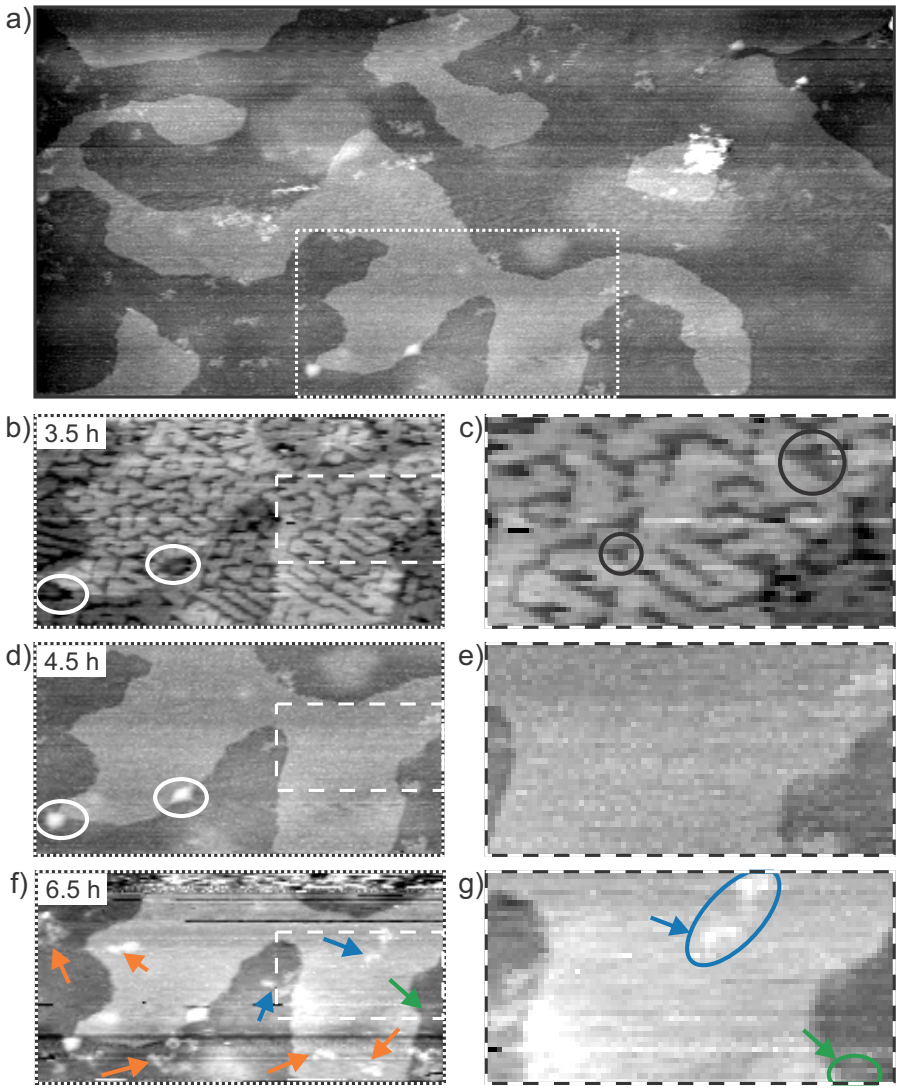

Figure 8.18: Overview images of the silica bilayer at elevated temperature. a) Conventional STM image acquired in constant current mode on the silica bilayer on Ru(0001) at 600 K (scan area = 300 nm × 135 nm, acquisition time = 15 min). b,d,f) Closeup views of the area highlighted with the white dotted rectangle in a) over several hours (scan area = 110 nm × 60 nm, acquisition time = 7 min). The acquisition time of each image is displayed in the upper left corner. The images are not drift or distortion corrected. Different image contrasts are observed. For visualization, c,e,g) show closeup views of the area highlighted with dashed rectangles in b,d,f), respectively (scan area = 45 nm × 24 nm). Areas that exhibit local contrast inversion are marked in b) and d) with white ellipses. Dark features in the resolved fine structure in c) are exemplarily marked with black circles. Scan parameters for all images: V_S = 1.6 V, I_T = 0.9 nA, T = 600 K.

Figure 8.18f, local changes of bright features are detected, as indicated by the colored arrows. Protrusions change their position (blue arrows), appear (orange arrows), or disappear (green arrows). The observation of mobile species on the surface and the fact that imaging conditions change rapidly, indicate that considerable dynamic processes occur at the sample surface at 600 K.

In addition to mobile species, dynamics in the film system should be considered at elevated temperatures. The network structure is not stiff, but exhibits a certain flexibility of the Si-O-Si bonds. Figure 8.19 shows snapshots of a molecular dynamics simulation at 300 K based on a machine learned force field. The simulation on the (6×x6) unit cell of SiO_2/Ru(0001) was performed by Joachim Paier. [148] The projected bond angles show variations over time as indicated exemplarily in top silica layer with dotted white ellipses. The relative oxygen atom position changes dynamically on short time scales of femtoseconds. In addition, it was shown that lateral displacements of the film are theoretically feasible at room temperature and that the mobility depends on the oxygen coverage at the interface. [148] At elevated temperatures, these dynamics are expected to have a great influence. Depending on the interfacial oxygen concentration, atomic network resolution in STM measurements can be hindered at elevated temperatures.

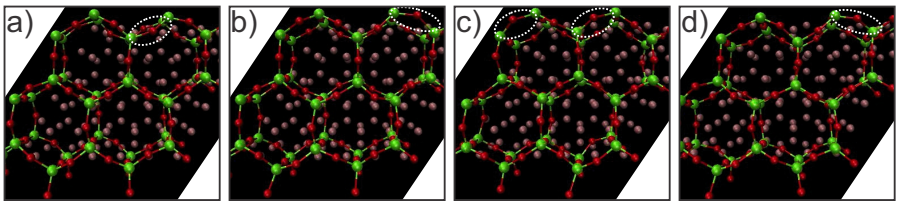

Figure 8.19: Molecular dynamics simulation of the silica bilayer on Ru(0001) at room temperature. Top view of the (6×6) cell containing the Ru support (gray), Si (green), and oxygen atoms (red balls). Snapshots of the system are shown at a) 4.35 ps, b) 4.40 ps, c) 4.60 ps, d) 4.95 ps. Changing bond angle orientations are exemplarily highlighted with dotted white ellipses. Adapted from Ref. [148].

High-speed measurements at elevated temperatures are challenging due to the increased mobility in the silica film system and due to generally increased noise level. Figure 8.20 shows the conventional STM image of the silica bilayer on Ru(0001) at 600 K in comparison to spiral STM images. The conventional STM image in Figure 8.20a shows the silica film with mesoscopic holes. The bright features are attributed to species adsorbed on the silica film.

The spiral images show a scan field of 60 nm in diameter. In these large scan areas, silica terraces are identified as marked with the orange line. To verify that the observed features are not related to scan artifacts and to monitor different regions of the sample surface, the

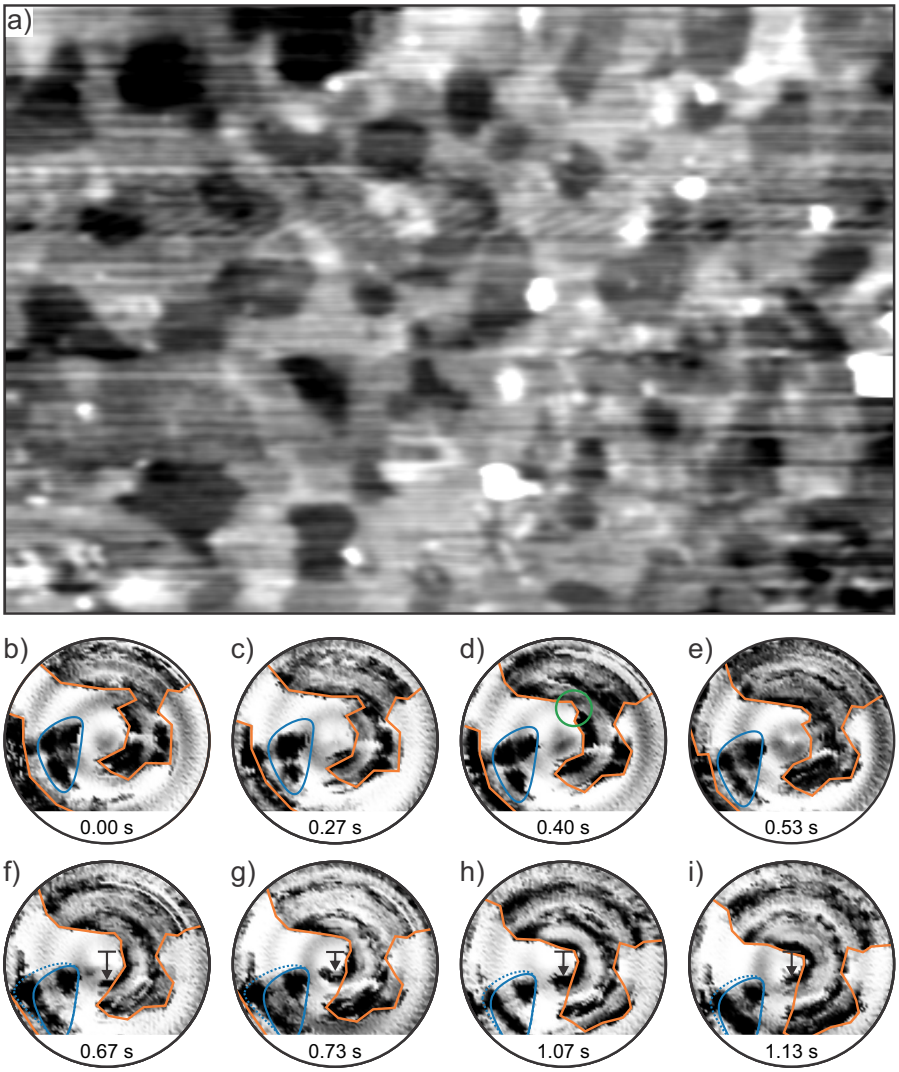

Figure 8.20: High-speed scans on the silica bilayer at elevated temperature. a) Conventional STM image acquired in constant current mode on the silica bilayer on Ru(0001) at 600 K (scan area = 260 nm × 180 nm, acquisition time = 13 min). b-i) Spiral STM image in quasi-constant height mode showing the silica film as outlined with orange lines (scan diameter = 60 nm, acquisition time = 67 ms). Within the area outlined in blue mesoscopic dark features are detected that change their configuration over time. The green circle in d) marks a change in the detected outline of the silica film. Scan parameters for all images: V_S = 4 V, I_T = 0.9 nA, T = 600 K.

tip was moved intentionally during the scan at a speed of 8.5 nm/s. This displacement of the tip at constant speed results in a shift of the observed features to the bottom of the frame. As indicated by the orange line, the coarse outline of the terrace does change over time. However, the protuberance present in Figures 8.20b,c is smoothed in the consecutive frame in Figure 8.20d. This subtle change of the terrace borders is highlighted with the green circle in Figure 8.20d.

An apparent feature arises in Figure 8.20f, as marked with the black arrow. The dark area is also detected in the consecutive frames in Figures 8.20g-i. It is detected at slightly varying positions in the scan field, as indicated by the black arrows of different lengths in Figures 8.20f-i. In contrast to the detected film edges, this feature does not shift to the bottom of the frame over time as expected due to the applied shift to the STM tip. Due to this observation and the curved shape of the depression, this local image contrast is attributed to scan artifacts.

In contrast to this, the dark area in the upper right of the region outlined in blue follows the imposed shift of the scan field and remains in the same position with respect to the film edge. Within the region outlined in blue in Figure 8.20b additional dark areas of approximately 4 to 9 nm in diameter are detected. While in Figure 8.20b, the dark areas are located within the region outlined in blue, they are separated in Figure 8.20f and extend to the dotted blue line. This observation indicates that the formation of these mesoscopic features changes over time.

To study potential dynamic processes of mesoscopic scale features, scans on single silica terrace are performed using smaller diameters of 30 nm, as shown in Figure 8.21. Mesoscopic dark features are detected as exemplarily outlined with white ellipses. They vary in size from 1 to 4 nm in diameter. With this diameter distribution they are approximately half of the size of the mobile features observed in Figure 8.20. They are comparable in size to the mesoscopic dark feature detected in Figure 8.17 and to the dark features within the fine structure resolved in Figure 8.18c. Furthermore the dimensions agree with the blurred areas reported in TEM images in connection with structural changes in the oxide network structure as marked with the white ellipse in Figure 8.14. [91]

Figure 8.21 shows the same scan area over several seconds. As mentioned above, characteristic mesoscopic dark features are marked with white outlines. The local image contrast is compared to the first frame in Figure 8.21a. Dark features that are less pronounced in Figures 8.21b-h than in Figure 8.21a are marked with an additional superimposed dotted blue ellipse. Figure 8.21b hows that several dark features are less pronounced. Either the feature size is decreased or the local image contrast is fainter. Also the reverse effect of features appearing more pronounced than in the previous frame is observed. In the consecutive frame in Figure 8.21c, the features showing this reversible change in image contrast resulting in a similar contrast as in Figure 8.21a are marked with a white outline only. Dark features that are not observed in Figure 8.21a but are detected in consecutive frames are highlighted with dotted orange lines. From the changing outlines from frame to frame it becomes obvious that the local image contrast changes frequently and reversibly.

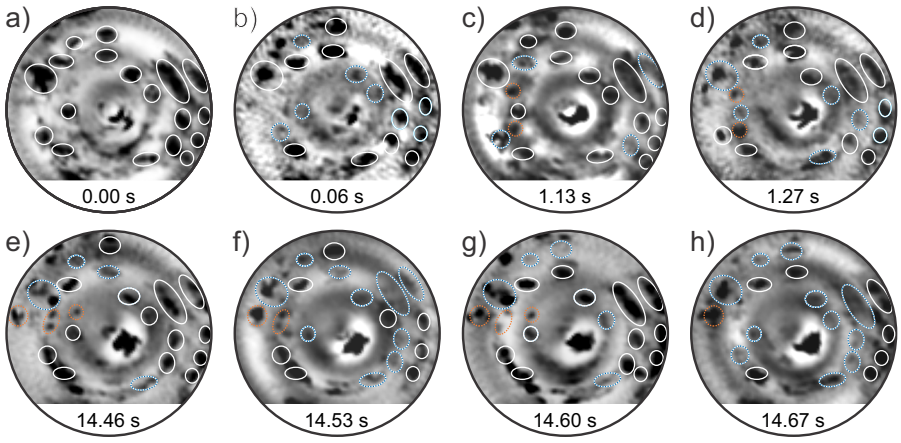

Figure 8.21: High-speed scans on a flat silica terrace at elevated temperature. a-h) Spiral STM image in quasi-constant height mode showing the silica film with mesoscopic dark features highlighted with white ellipses. Changes in the local image contrast with respect to the STM image in a) are highlighted with colored dotted ellipses. Blue and orange dotted ellipses mark less and more pronounced features in comparison to a), respectively. Scan parameters for all images: V_S = 4 V, I_T = 0.9 nA, scan diameter = 30 nm, acquisition time = 67 ms, T = 600 K.

It is worth noting that the lateral positions of the detected features changes slightly from frame to frame. This effect has not been observed in room temperature measurements presented in Sections 6.3, 6.4, 6.5, 7.1, 7.2, 7.3, 8.2, and 8.3.2. The spiral images are free of drift and distortions. Therefore, the changing lateral positions are not attributed to scan artifacts but they seem to be caused by the elevated temperature. As discussed above, at elevated temperatures the dynamics in the silica film are expected to have a great influence. Additional calculations show that the center of mass of the bilayer oscillates in the order of 0.02 nm at room temperature. [148] DFT calculations provide activation barriers for the lateral displacement of the silica bilayer film in the order of 0.7 eV. [148] Hence, at elevated temperatures, it can be expected that the film can show a certain mobility parallel to the substrate surface. This mobility of the film system itself could explain the observed slight changes in the lateral positions of the dark features in Figure 8.21.

As discussed above, also the interfacial oxygen layer can have an influence on the imaging contrast and is expected to exhibit an increased mobility at elevated temperatures. To fully answer the question which effect is responsible for the observed changing feature intensities and the slight lateral displacement of the mesoscopic features, future studies will focus on high-speed STM measurements at elevated temperatures of differently prepared oxide thin film systems.

In this Section, we set the stage for future studies at elevated temperatures. It was shown that the microscope can operate at elevated

temperatures and that scanning over long times of several hours is possible with minimal thermal drift. High-speed spiral scans on the silica bilayer on oxygen covered Ru(0001) at elevated temperatures of 600 K revealed film patches and mobile mesoscopic features. The observed mobility form the basis for future studies. On the one hand, further statistical analysis of the observed effects as a function of scan parameters and sample temperature is interesting. On the other hand, a possible pathway to resolve dynamics on top or inside the film system at elevated temperatures is to select sample systems without mobile interfacial species. One possibility is to expose the silica film on Ru(0001) to reducing conditions, such as thermal treatments in hydrogen atmosphere to remove the interfacial oxygen. Another possibility is to consider different oxide-substrate combinations that can be prepared without oxygen pre-coverages to reduce the impact of mobile species at the film-substrate interface.

Part V

SUMMARY

9 CONCLUSION AND OUTLOOK

A high-speed STM was designed and built that can operate at variable temperatures. The microscope assesses dynamic processes at the atomic scale in real space and in real time.

Chapters 1-4 provided literature reviews and described the underlying concepts that were considered for the design of the home built STM.

In Chapters 5 and 6, the design and working principle of the microscope was presented. Besides the mechanical design, the realization of high-speed scans was described. For the high-speed STM measurements, we successfully implemented innovative spiral scan patterns. For the first time, spiral geometries were used to realize high-speed STM scans. The successful implementation was demonstrated by repeating the breakthrough experiment of the first video STM measurements by Joost Wintterlin et al., who monitored diffusing oxygen atoms on the Ru(0001) surface with frame rates of approximately 10 Hz. With the spiral scan geometry, we achieved frame rates of 120 Hz. To realize the unconventional scan geometry, highly customizable python software was developed. The software was essential to generate the scan input signals, to acquire, to store, and to process the data, and to analyze the resulting images. We made the program for image reconstruction and data analysis free to access to facilitate the implementation of unconventional scan patterns.

In Chapter 7, we investigated dynamics within dense oxygen adlayers on Ru(0001) at room temperature. These adlayers are relevant for catalytic reactions and they are present as interfacial layers between thin oxide films and the underlying metal substrate.

We revealed dynamics within the O(2×2) layer on Ru(0001) that exceed the reported jump rates based on conventional STM measurements reported in literature. The observed jump rates are in agreement with DFT calculations (provided by Joachim Paier). Due to the increased lateral and temporal resolution in the center of the spiral scan, the occupied intermediate state along the oxygen diffusion pathway could be resolved. DFT calculations confirm the presence of an intermediate state at this spatial position.

In the oxygen deficient O(2×1) layer on Ru(0001), DFT calculations propose that oxygen atoms occupy the adjacent hcp site that coincides with the (1×1) grid. Considering the diffusion in several unit cells, this results in a reorientation of the characteristic 1D stripe pattern. With our high-speed spiral STM, we resolved individual hopping events of oxygen atoms within the O(2×1) layer at room temperature. Scans

of areas showing differently oriented domains revealed reversible structural changes, i.e. growing and shrinking of domains at the expense of adjacent domains. This phenomenon was observed in the range of minutes. At the millisecond timescale similar processes were observed that can be described as fast flipping events. These fast flipping events relate to the long term restructuring over minutes and agree with the theoretical considerations of structural reorientation of the 1D stripe pattern.

The dense 3O(2×2) layer on Ru(0001) was investigated at room temperature. The STM contrast shows the characteristic hexagonal structure that does not reveal individual atomic oxygen atoms, which is in agreement with results reported in literature. With this image contrast, dynamic processes were detected in the 3O(2×2) layer by high-speed spiral STM at room temperature. The occupation of different sites on the hexagonal grid was resolved. The dynamic processes are reversible over time.

In Chapter 8, the preparation for the structural analysis of large data sets was presented. A semi-automated network detection tool was developed and a graphical user interface was implemented to facilitate interactive modifications of the detected network structure. The working principle has been successfully demonstrated exemplarily for a vitreous silica bilayer across a Ru(0001) step edge. The network detection tool enabled advanced structural analysis of characteristic film properties, such as the evolution of the film crystallinity and of the silica ring-ring distances across the metal step edge. The analysis revealed the continuous coverage of the vitreous silica bilayer across the Ru(0001) step edge. The experimental results are supported by DFT calculations (provided by Sergio Tosoni and Gianfranco Pacchioni). The theoretical models include structures where the bottom silica layer is pinned to the substrate step and carpet-like coverages of the silica bilayer across the step. Based on the structural analysis of the evolution of silica ring-ring distances across the step edge region, a qualitative agreement of the carpet-like model and the experimental data was found. The semi-automated network detection tool is applicable to images recorded with any arbitrary technique and exhibiting different length scales making it transferable to other disciplines.

The mesoscopic and the atomic network structure of a germania monolayer on Ru(0001) could be resolved with high-speed spiral STM. The semi-automated network detection tool revealed a complex domain boundary in both conventional and spiral STM images. This successful network detection proved that the developed tool is suitable to analyze large datasets of spiral STM images. Local contrast changes were observed on a prominent domain boundary feature. These dynamic contrast changes may relate to mobile species, such as the interfacial oxygen atoms.

Both the crystalline and the vitreous silica bilayer were recorded at high speed with the spiral STM at room temperature. Blurred regions in the images of the vitreous phase are detected making the ring assignment challenging. Nevertheless, by comparing consecutive frames, consistent ring features could be identified. Distinct changes of the local image contrast on the silica bilayer were detected. The changes consisted of fluctuations in the apparent shape and size of silica rings and their interconnections. In addition, lateral displacements of regions with bright image contrasts were resolved indicating dynamics on, in, or under the silica film. The observed dynamics may relate to the interfacial oxygen layer. More dynamic changes in the local image contrast were observed regarding the silica network structure. Silica ring configurations appeared differently over time. We provided examples, where the image contrast of ring formations changed significantly in several consecutive frames.

At the end of Chapter 8 we performed STM measurements on the silica bilayer at elevated temperatures of 600 K, which was part of an outlook for future studies. Large areas could be measured without drift or distortion corrections and the scan area was stable for more than seven hours. Using the same scan parameters, different image contrasts were observed over time. For instance, local contrast inversion and temporarily resolved fine structures that may relate to the interfacial oxygen layer were observed. Comparing consecutive conventional STM images of the same scan area, changing image features were detected that were attributed to mobile species on or under the film, such as oxygen.

Mesoscopic features of the silica bilayer film were resolved with high-speed spiral STM at 600 K. The outline of the silica film terrace could be identified and used as reference to track mesoscopic dark features in the film. The features showed a certain mobility. Measurements on the flat silica terrace revealed dynamic changes of both the image contrast of mesoscopic dark features and of their lateral position. Future studies will focus on the mobility of these mesoscopic features. Interesting experiments include variations of the scan parameters and of the sample temperature.

We revealed dynamic processes in the sample system of silica on Ru(0001) at elevated temperatures of 600 K. Future studies may consider removing the oxygen interfacial layer and therefore preventing dynamics caused by mobile oxygen atoms at the interface. The interfacial oxygen can be removed by exposing the film system to reducing conditions, such as thermal annealing in hydrogen atmosphere. The interfacial oxygen layer, on the other hand may play a crucial role in the context of structural transformations. During the transformation, the formation of dangling bonds in the lower layer is proposed by DFT, as outlined in Section 2.3. These dangling bonds can chemically bond

to the underlying bare metal substrate. Since the interplay between substrate, interfacial layer, and oxide network former plays a crucial role for these structural transformations, different sample systems, i.e. oxide-metal combinations, may be considered for future studies.

The advances in high-speed STM using unconventional scan pattern may constitute the beginning of a paradigm shift of how to perform STM measurements. Until now, we operated our microscope below its capacity limits and therefore we are confident that with our approach sub-millisecond resolution is in reach.

The revealed dynamics in the dense oxygen adlayers on Ru(0001) that are present underneath metal supported thin oxide film systems and the observed dynamic changes in the local imaging contrast on oxide networks pave the way for future dynamic studies considering sample systems of different metal-oxide combinations. With the high-speed capabilities at variable temperatures, the opportunity to study dynamic processes of thin oxide films is opened. In the long-term, this new high speed spiral STM has the capability to unravel structural dynamics in oxide thin films that may result in transformations between crystalline and vitreous phases.

Part VI

APPENDIX

a

APPENDIX

A.1 HIGH-SPEED SPIRAL STM IMAGES ON SILICA ON RU(0001)

In Section 8.3.2, high-speed spiral STM images are provided with overlaid dashed rings highlighting consistent ring features. In this section, the figures are shown without overlaid rings.

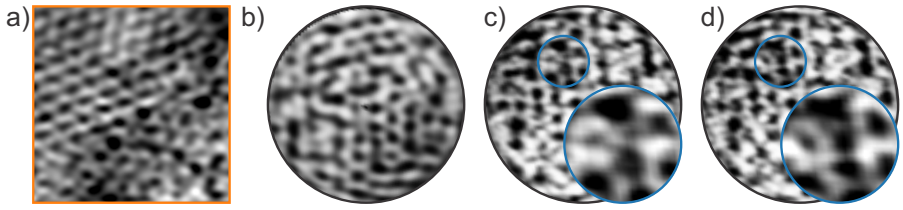

Figure a.1: Figure 8.11 without overlaid features. STM images of vitreous silica bilayer patches on Ru(0001). a) Magnified region of 5 nm × 5 nm marked with the orange square in Figure 8.10 a). Vitreous and crystalline regions are detected. b) Average of 20 consecutive spiral STM images, acquired in total 1 s. c,d) Consecutive spiral STM image, acquired in 50 ms (V_S = 1.6 V, I_T = 1 nA, T = 300 K, scan area = 5 nm × 5 nm).

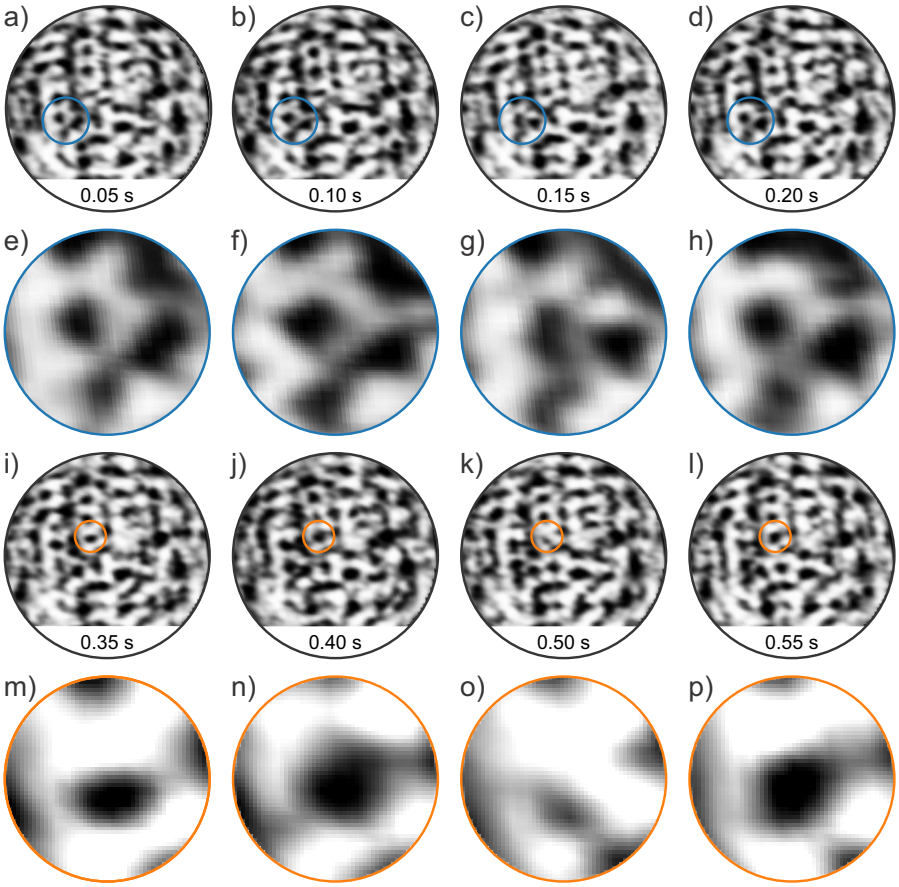

Figure a.2: Figure 8.12 without overlaid features. Dynamic changes in the image contrast on silica on Ru(0001). a-d), i-l) Spiral STM images on the silica bilayer on Ru(0001), acquired in 50 ms (V_S = 0.8 V, I_T = 1 nA, T = 300 K, scan area = 5 nm × 5 nm). The time is indicated at the bottom of each frame. Regions of interest highlighted in blue and orange are magnified in e-h) and m-p), respectively. e-h) Dynamic changes of the appearance of the rings and of their interconnections are resolved. m-p) Dynamic changes of the apparent ring size are resolved.

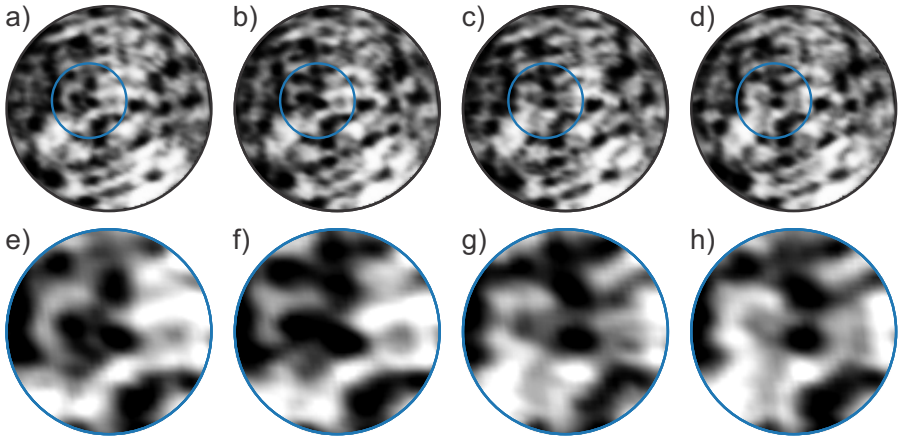

Figure a.3: Figure 8.15 without overlaid features. Dynamic lateral displacement of a bright ring feature. a-d) Consecutive spiral STM images on the silica bilayer on Ru(0001), acquired in 50 ms (V_S = 0.8 V, I_T = 1 nA, T = 300 K, scan area = 5 nm × 5 nm). The lateral displacement of a region with bright image contrast is detected, as shown in the zoomed images in e-h) (1.8 nm × 1.8 nm).

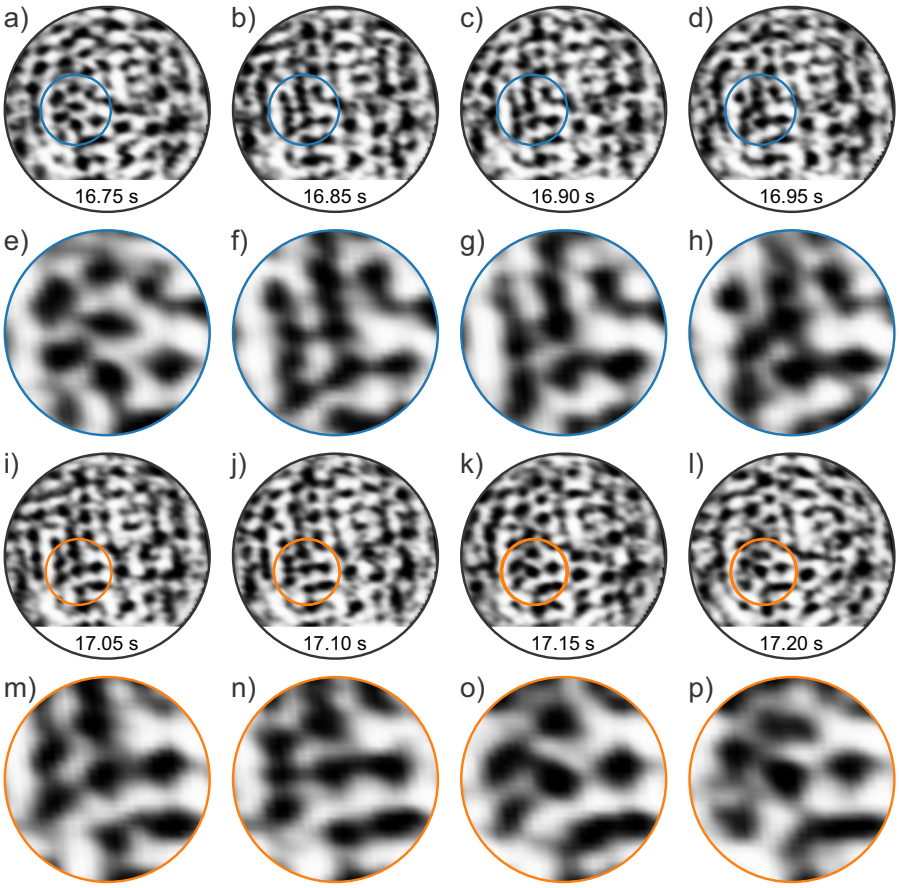

Figure a.4: Figure 8.16 without overlaid features. Dynamic changes of the ring contrast. a-d), i-l) Spiral STM images on the silica bilayer on Ru(0001), acquired in 50 ms (V_S = 0.8 V, I_T = 1 nA, T = 300 K, scan area = 5 nm × 5 nm). The time is indicated at the bottom of each frame. Regions of interest highlighted in blue and orange are magnified in e-h) and m-p), respectively. Consistent changes of the apparent ring configuration are detected.

A.2 TIP DISPLACEMENT EXPERIMENT ON SILICA ON RU(0001)

Given the partly blurred image contrast of high-speed scans on the silica bilayer, the question arises whether changes in the ring network can be detected reliably. The consistently overlaid ring features in Figures 8.11 and 8.12 already indicate that consecutive frames can be related to each other accurately. To verify that changes can also be detected quantitatively we performed the same experiment as presented in Figure 8.7 in Section 8.2. Averaged images of 100 frames are shown and the image contrast allows us to identify local ring configurations, as exemplarily indicated by dashed circles.

In analogy to Figure 8.7 in Section 8.2, the STM tip was displaced intentionally while scanning. The averaged image in Figure a.5a is recorded before and the averaged image in Figure a.5b is recorded after the tip displacement, respectively. The expected result is a lateral shift of the scan area. To verify that the detection of the local ring configurations allows us to quantify the changes of the imaged silica bilayer network, the displacement vector is determined. For the determination the two methods presented in Section 8.2 are applied. The position of the characteristic ring highlighted in orange is tracked over time. The resulting displacement vector is drawn in orange in Figure a.5c. Figure a.5d shows the difference between the self-correlation of Figure a.5a and the cross correlation of Figures a.5a and b. The intensity maximum determines the displacement vector, which is in very good agreement with Figure a.5c.

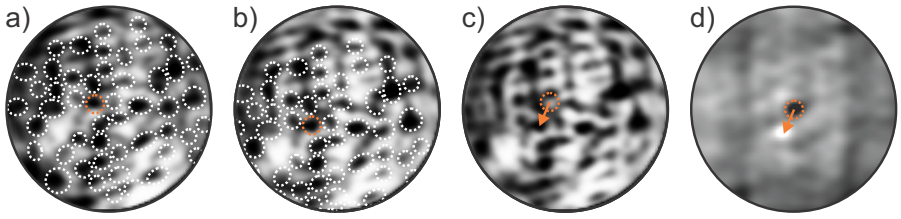

Figure a.5: Lateral displacement of the scan area on the silica bilayer. a-c) Averaged images of 100 consecutive spiral STM images, acquired in total 5 s (V_S = 0.8 V, I_T = 1 nA, T = 300 K, scan area = 5 nm × 5 nm). The STM tip was moved intentionally between a) and b). The displacement is detected looking at characteristic ring features as highlighted with dashed circles. The ring marked in orange serves as the reference to determine the displacement vector, as shown with the orange arrow in c). d) In analogy to Figure 8.7, the difference of self-correlation and cross correlation is shown. The displacement vector (orange arrow) can be clearly identified and agrees with the vector in c).

As described in Section 8.2, the averaged images and the fact that they show comparable ring features are a proof for the absence of image distortions and thermal drift artifacts in the high-speed STM frames.

A.3 STM MEASUREMENTS ON SILICA ON RU(0001) AT ELEVATED TEMPERATURE

Figure a.6 shows the image sequence of conventional STM images on the silica bilayer on Ru(0001) at 600 K. It complements Figure 8.18 and illustrates that the home built STM can be operated in stable conditions at elevated temperatures over hours or even days. The scan field remains the same without the need for drift correction.

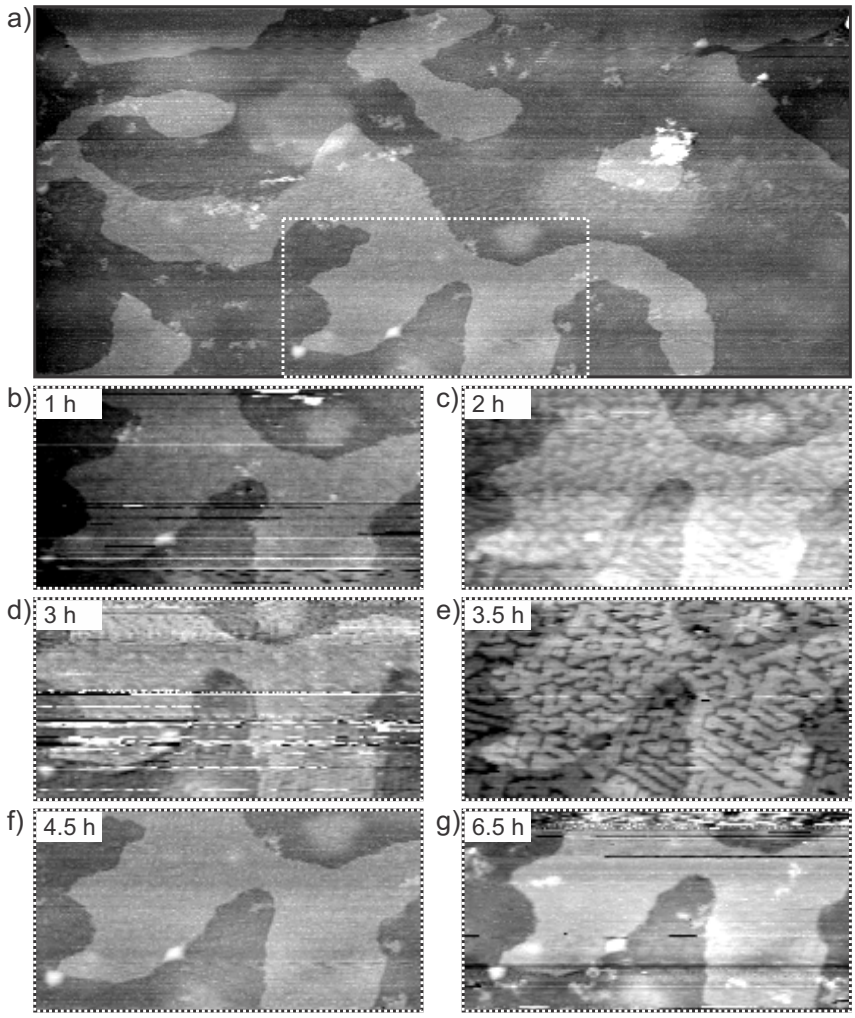

Figure a.6: Supplement to Figure 8.18. a) Conventional STM image acquired in constant current mode on the silica bilayer on Ru(0001) at 600 K (scan area = 300 nm × 135 nm, acquisition time = 15 min). b-g) Closeup views of the area highlighted with the white dashed rectangle in a) over several hours (scan area = 110 nm × 60 nm, acquisition time = 7 min). The acquisition time of each image is displayed in the upper left corner. The images are not drift or distortion corrected. Different image contrasts are observed. Scan parameters for all images: V_S = 1.6 V, I_T = 0.9 nA, T = 600 K.

BIBLIOGRAPHY

[1] G. Ertl. *Reactions at solid surfaces*. John Wiley & Sons, 2010.

[2] O. M. Magnussen. "Atomic-Scale Insights into Electrode Surface Dynamics by High-Speed Scanning Probe Microscopy." In: *Chem. Eur. J.* 25.56 (2019), pp. 12865–12883.

[3] G. Ertl. "Reactions at Surfaces: From Atoms to Complexity (Nobel Lecture)." In: *Angewandte Chemie International Edition* 47.19 (2008), pp. 3524–3535.

[4] A. Kapoor, R. T. Yang, and C. Wong. "Surface diffusion." In: *Catalysis Reviews-Science and Engineering* 31.1-2 (1989), pp. 129–214.

[5] D. A. King and D. Woodruff. *Growth and properties of ultrathin epitaxial layers*. Vol. 8. Elsevier, 1997. Chap. 3.

[6] M. Volmer and I. Estermann. "Über den Mechanismus der Molekülabscheidung an Kristallen." In: *Zeitschrift für Physik* 7.1 (1921), pp. 13–17.

[7] E. W. Müller. "Das Feldionenmikroskop." In: *Zeitschrift für Physik* 131.1 (1951), pp. 136–142.

[8] W. R. Graham and G. Ehrlich. "Surface Self-Diffusion of Atoms and Atom Pairs." In: *Phys. Rev. Lett.* 31 (1973), pp. 1407–1408.

[9] Z. Yang et al. "A high-speed variable-temperature ultrahigh vacuum scanning tunneling microscope with spiral scan capabilities." In: *Review of Scientific Instruments* 93.5 (2022), p. 053704.

[10] A. H. Zewail. "Femtochemistry: Atomic-Scale Dynamics of the Chemical Bond Using Ultrafast Lasers (Nobel Lecture)." In: *Angewandte Chemie International Edition* 39.15 (2000), pp. 2586–2631.

[11] S. Loth, M. Etzkorn, C. P. Lutz, D. M. Eigler, and A. J. Heinrich. "Measurement of Fast Electron Spin Relaxation Times with Atomic Resolution." In: *Science* 329.5999 (2010), pp. 1628–1630.

[12] M. Morgenstern. "STM Ready for the Time Domain." In: *Science* 329.5999 (2010), pp. 1609–1610.

[13] Y. Terada, S. Yoshida, O. Takeuchi, and H. Shigekawa. "Real-space imaging of transient carrier dynamics by nanoscale pump-probe microscopy." In: *Nature Photonics* 4.12 (2010), pp. 869–874.

[14] T. L. Cocker, V. Jelic, M. Gupta, S. J. Molesky, J. A. J. Burgess, G. D. L. Reyes, L. V. Titova, Y. Y. Tsui, M. R. Freeman, and F. A. Hegmann. "An ultrafast terahertz scanning tunnelling microscope." In: *Nature Photonics* 7.8 (2013), pp. 620–625.

[15] T. L. Cocker, D. Peller, P. Yu, J. Repp, and R. Huber. "Tracking the ultrafast motion of a single molecule by femtosecond orbital imaging." In: *Nature* 539.7628 (2016), pp. 263–267.

[16] B. C. Stipe, M. A. Rezaei, and W. Ho. "Single-Molecule Vibrational Spectroscopy and Microscopy." In: *Science* 280.5370 (1998), pp. 1732–1735.

[17] J. Guo et al. "Nuclear quantum effects of hydrogen bonds probed by tip-enhanced inelastic electron tunneling." In: *Science* 352.6283 (2016), pp. 321–325.

[18] S. You, J.-T. Lü, J. Guo, and Y. Jiang. "Recent advances in inelastic electron tunneling spectroscopy." In: *Advances in Physics: X* 2.3 (2017), pp. 907–936.

[19] G. Binnig, H. Rohrer, C. Gerber, and E. Weibel. "Surface Studies by Scanning Tunneling Microscopy." In: *Phys. Rev. Lett.* 49 (1982), pp. 57–61.

[20] G. Binnig, H. Rohrer, C. Gerber, and E. Weibel. "7×7 Reconstruction on Si(111) Resolved in Real Space." In: *Phys. Rev. Lett.* 50 (1983), pp. 120–123.

[21] M. van Hove, J. Cerda, P. Sautet, M.-L. Bocquet, and M. Salmeron. "Surface Structure Determination by STM vs LEED." In: *Progress in Surface Science* 54.3 (1997), pp. 315–329.

[22] G. Kresse, M. Schmid, E. Napetschnig, M. Shishkin, L. Köhler, and P. Varga. "Structure of the Ultrathin Aluminum Oxide Film on NiAl(110)." In: *Science* 308.5727 (2005), pp. 1440–1442.

[23] M. F. Crommie, C. P. Lutz, and D. M. Eigler. "Imaging standing waves in a two-dimensional electron gas." In: *Nature* 363.6429 (1993), pp. 524–527.

[24] M. F. Crommie, C. P. Lutz, and D. M. Eigler. "Confinement of Electrons to Quantum Corrals on a Metal Surface." In: *Science* 262.5131 (1993), pp. 218–220.

[25] L. Gura, Z. Yang, H. Junkes, M. Heyde, and H.-J. Freund. *Going fast with STM imaging*. Ed. by K. Wandelt. Elsevier, in press. Chap. 40095.

[26] A. Bryant, D. P. E. Smith, and C. F. Quate. "Imaging in real time with the tunneling microscope." In: *Appl. Phys. Lett.* 48.13 (1986), pp. 832–834.

[27] S. Park and C. F. Quate. "Tunneling microscopy of graphite in air." In: *Appl. Phys. Lett.* 48.2 (1986), pp. 112–114.

[28] R. S. Robinson. "Increasing the scanning speed of scanning tunnelling microscopes." In: *Journal of Microscopy* 152.2 (1988), pp. 387–397.

[29] C. Ludwig, B. Gompf, W. Glatz, J. Petersen, W. Eisenmenger, M. Möbus, U. Zimmermann, and N. Karl. "Video-STM, LEED and X-ray diffraction investigations of PTCDA on graphite." In: *Zeitschrift für Physik B Condensed Matter* 86.3 (1992), pp. 397–404.

[30] H. J. Mamin, H. Birk, P. Wimmer, and D. Rugar. "High-speed scanning tunneling microscopy: Principles and applications." In: *Journal of Applied Physics* 75.1 (1993), pp. 161–168.

[31] J. Wintterlin, J. Trost, S. Renisch, R. Schuster, T. Zambelli, and G. Ertl. "Real-time STM observations of atomic equilibrium fluctuations in an adsorbate system: O/Ru(0001)." In: *Surface Science* 394.1 (1997), pp. 159–169.

[32] Q. Li and Q. Lu. "Atomic resolution ultrafast scanning tunneling microscope with scan rate breaking the resonant frequency of a quartz tuning fork resonator." In: *Review of Scientific Instruments* 82.5 (2011), p. 053705.

[33] C. Dri et al. "The new FAST module: A portable and transparent add-on module for time-resolved investigations with commercial scanning probe microscopes." In: *Ultramicroscopy* 205 (2019), pp. 49–56.

[34] L. L. Patera, F. Bianchini, C. Africh, C. Dri, G. Soldano, M. M. Mariscal, M. Peressi, and G. Comelli. "Real-time imaging of adatom-promoted graphene growth on nickel." In: *Science* 359.6381 (2018), pp. 1243–1246.

[35] M. J. Rost et al. "Scanning probe microscopes go video rate and beyond." In: *Review of Scientific Instruments* 76.5 (2005), p. 053710.

[36] F. Esch, C. Dri, A. Spessot, C. Africh, G. Cautero, D. Giuressi, R. Sergo, R. Tommasini, and G. Comelli. "The FAST module: An add-on unit for driving commercial scanning probe microscopes at video rate and beyond." In: *Review of Scientific Instruments* 82.5 (2011), p. 053702.

[37] A.-K. Henß, S. Sakong, P. K. Messer, J. Wiechers, R. Schuster, D. C. Lamb, A. Groß, and J. Wintterlin. "Density fluctuations as door-opener for diffusion on crowded surfaces." In: *Science* 363.6428 (2019), p. 715.

[38] S. B. Andersson and D. Y. Abramovitch. "A Survey of Non-Raster Scan Methods with Application to Atomic Force Microscopy." In: *2007 American Control Conference*. 2007, pp. 3516–3521.

[39] J. Wang, J. Wang, Y. Hou, and Q. Lu. "Self-manifestation and universal correction of image distortion in scanning tunneling microscopy with spiral scan." In: *Review of Scientific Instruments* 81.7 (2010), p. 073705.

[40] S.-K. Hung. "Spiral scanning method for atomic force microscopy." In: *Journal of nanoscience and nanotechnology* 10.7 (2010), pp. 4511–4516.

[41] A. Bazaei, Y. K. Yong, and S. O. R. Moheimani. "High-speed Lissajous-scan atomic force microscopy: Scan pattern planning and control design issues." In: *Review of Scientific Instruments* 83.6 (2012), p. 063701.

[42] D. Ziegler, T. R. Meyer, R. Farnham, C. Brune, A. L. Bertozzi, and P. D. Ashby. "Improved accuracy and speed in scanning probe microscopy by image reconstruction from non-gridded position sensor data." In: *Nanotechnology* 24.33 (2013), p. 335703.

[43] M. S. Rana, H. R. Pota, and I. R. Petersen. "Spiral Scanning With Improved Control for Faster Imaging of AFM." In: *IEEE Transactions on Nanotechnology* 13.3 (2014), pp. 541–550.

[44] D. Ziegler, T. R. Meyer, A. Amrein, A. L. Bertozzi, and P. D. Ashby. "Ideal Scan Path for High-Speed Atomic Force Microscopy." In: *IEEE/ASME Transactions on Mechatronics* 22.1 (2017), pp. 381–391.

[45] S. K. Das, F. R. Badal, M. A. Rahman, M. A. Islam, S. K. Sarker, and N. Paul. "Improvement of Alternative Non-Raster Scanning Methods for High Speed Atomic Force Microscopy: A Review." In: *IEEE Access* 7 (2019), pp. 115603–115624.

[46] Z. Sun, N. Xi, Y. Xue, Y. Cheng, L. Chen, R. Yang, and B. Song. "Task Space Motion Control for AFM-Based Nanorobot Using Optimal and Ultralimit Archimedean Spiral Local Scan." In: *IEEE Robotics and Automation Letters* 5.2 (2019), pp. 282–289.

[47] T. Tuma, J. Lygeros, V Kartik, A. Sebastian, and A. Pantazi. "High-speed multiresolution scanning probe microscopy based on Lissajous scan trajectories." In: *Nanotechnology* 23.18 (2012), p. 185501.

[48] X. Sang, A. R. Lupini, R. R. Unocic, M. Chi, A. Y. Borisevich, S. V. Kalinin, E. Endeve, R. K. Archibald, and S. Jesse. "Dynamic scan control in STEM: Spiral scans." In: *Advanced Structural and Chemical Imaging* 2.1 (2016), p. 6.

[49] D. Momotenko, J. C. Byers, K. McKelvey, M. Kang, and P. R. Unwin. "High-Speed Electrochemical Imaging." In: *ACS Nano* 9.9 (2015), pp. 8942–8952.

[50] F. Besenbacher, E. Lægsgaard, and I. Stensgaard. "Fast-scanning STM studies." In: *Materials Today* 8.5 (2005), pp. 26–30.

[51] J. A. Schreifels, S.-K. Shi, and J. M. White. "The effect of electron beam and surface diffusion on the kinetics of adsorbed oxygen reacting with hydrogen on Ru(001)." In: *Applications of Surface Science* 7.4 (1981), pp. 312–324.

[52] M. C. Wheeler, D. C. Seets, and C. B. Mullins. "Kinetics and dynamics of the initial dissociative chemisorption of oxygen on Ru(001)." In: *J. Chem. Phys.* 105.4 (1996), pp. 1572–1583.

[53] P. Piercy, K. De'Bell, and H. Pfnür. "Phase diagram and critical behavior of the adsorption system O/Ru(001): Comparison with lattice-gas models." In: *Phys. Rev. B* 45.4 (1992), pp. 1869–1877.

[54] H. Over. "Surface Chemistry of Ruthenium Dioxide in Heterogeneous Catalysis and Electrocatalysis: From Fundamental to Applied Research." In: *Chem. Rev.* 112.6 (2012), pp. 3356–3426.

[55] T. E. Madey, H. Albert Engelhardt, and D. Menzel. "Adsorption of oxygen and oxidation of CO on the ruthenium (001) surface." In: *Surface Science* 48.2 (1975), pp. 304–328.

[56] K. Meinel, H. Wolter, C. Ammer, A. Beckmann, and H. Neddermeyer. "Adsorption stages of O on Ru(0001) studied by means of scanning tunnelling microscopy." In: *Journal of Physics: Condensed Matter* 9.22 (1997), pp. 4611–4619.

[57] N. Nilius, M. Mitte, and H. Neddermeyer. "Low-temperature scanning tunnelling microscopy study of O_2 adsorption on Ru(0001)." In: *Applied Physics A* 66.1 (1998), S519–S523.

[58] M. Lindroos, H. Pfnür, G. Held, and D. Menzel. "Adsorbate induced reconstruction by strong chemisorption: Ru(001)p(2×2)-O." In: *Surface Science* 222.2 (1989), pp. 451–463.

[59] L. Gura, Z. Yang, M. Brinker, F. Kalaß, W. Kirstaedter, P. Marschalik, H. Junkes, M. Heyde, and H.-J. Freund. "Spiral high-speed scanning tunneling microscopy: Tracking atomic diffusion on the millisecond timescale." In: *Applied Physics Letters* 119.25 (2021), p. 251601.

[60] L. Gura, Z. Yang, J. Paier, F. Kalaß, M. Brinker, H. Junkes, M. Heyde, and H.-J. Freund. "Resolving atomic diffusion in $\mathrm{Ru}(0001) - \mathrm{O}(2 \times 2)$ with spiral high-speed scanning tunneling microscopy." In: *Phys. Rev. B* 105 (2022), p. 035411.

[61] L. Gura, Z. Yang, J. Paier, F. Kalaß, M. Brinker, H. Junkes, M. Heyde, and H.-J. Freund. "Dynamics in the $\mathrm{O}(2 \times 1)$ adlayer on Ru(0001): bridging timescales from milliseconds to minutes by scanning tunneling microscopy." In: *Phys. Chem. Chem. Phys.* 24 (2022), pp. 15265–15270.

[62] H.-J. Güntherodt and R. Wiesendanger. *Scanning tunneling microscopy I: general principles and applications to clean and adsorbate-covered surfaces*. Vol. 20. Springer, 1992.

[63] T. K. Shimizu, A. Mugarza, J. I. Cerdá, M. Heyde, Y. Qi, U. D. Schwarz, D. F. Ogletree, and M. Salmeron. "Surface Species Formed by the Adsorption and Dissociation of Water Molecules on a Ru(0001) Surface Containing a Small Coverage of Carbon Atoms Studied by Scanning Tunneling Microscopy." In: *J. Phys. Chem. C* 112.19 (2008), pp. 7445–7454.

[64] S. Maier, P. Cabrera-Sanfelix, I. Stass, D. Sánchez-Portal, A. Arnau, and M. Salmeron. "Water-induced surface reconstruction of oxygen (2×1) covered Ru(0001)." In: *Phys. Rev. B* 82.7 (2010), p. 075421.

[65] S. Maier, I. Stass, J. I. Cerdá, and M. Salmeron. "Unveiling the Mechanism of Water Partial Dissociation on Ru(0001)." In: *Phys. Rev. Lett.* 112.12 (2014), p. 126101.

[66] R. Souda and T. Aizawa. "Nucleation and growth of water ice on Ru(0001): Influences of oxygen and carbon-monoxide adspecies." In: *Chemical Physics Letters* 722 (2019), pp. 132–139.

[67] T. Li and J. A. Yarmoff. "Intercalation and desorption of oxygen between graphene and Ru(0001) studied with helium ion scattering." In: *Phys. Rev. B* 96.15 (2017), p. 155441.

[68] E. Voloshina, N. Berdunov, and Y. Dedkov. "Restoring a nearly free-standing character of graphene on Ru(0001) by oxygen intercalation." In: *Scientific Reports* 6.1 (2016), p. 20285.

[69] E. Emmez, J. Anibal Boscoboinik, S. Tenney, P. Sutter, S. Shaikhutdinov, and H.-J. Freund. "Oxidation of the Ru(0001) surface covered by weakly bound, ultrathin silicate films." In: *Surface science for heterogeneous catalysis, a special issue in Honour of Richard Lambert* 646 (2016), pp. 19–25.

[70] R. Włodarczyk, M. Sierka, J. Sauer, D. Löffler, J. J. Uhlrich, X. Yu, B. Yang, I. M. N. Groot, S. Shaikhutdinov, and H.-J. Freund. "Tuning the electronic structure of ultrathin crystalline silica films on Ru(0001)." In: *Phys. Rev. B* 85.8 (2012), p. 085403.

[71] J. Couzin. "What don't we know?" In: *Science* 309.5731 (2005), p. 83.

[72] Y. Castro and A. Jitianu. "Preface for the SI International Year of Glass IYOG 2022." In: *Journal of Sol-Gel Science and Technology* 102.3 (2022), pp. 465–465.

[73] D. Löffler et al. "Growth and Structure of Crystalline Silica Sheet on Ru(0001)." In: *Phys. Rev. Lett.* 105 (2010), p. 146104.

[74] B. Yang et al. "Thin silica films on Ru(0001): monolayer, bilayer and three-dimensional networks of [SiO_4] tetrahedra." In: *Phys. Chem. Chem. Phys.* 14 (2012), pp. 11344–11351.

[75] L. Lichtenstein, C. Büchner, B. Yang, S. Shaikhutdinov, M. Heyde, M. Sierka, R. Włodarczyk, J. Sauer, and H.-J. Freund. "The Atomic Structure of a Metal-Supported Vitreous Thin Silica Film." In: *Angewandte Chemie International Edition* 51.2 (2012), pp. 404–407.

[76] J.-Q. Zhong and H.-J. Freund. "Two-Dimensional Ultrathin Silica Films." In: *Chem. Rev.* 122.13 (2022), pp. 11172–11246.

[77] W. H. Zachariasen. "The atomic arrangement in glass." In: *J. Am. Chem. Soc.* 54.10 (1932), pp. 3841–3851.

[78] L. Lichtenstein, M. Heyde, and H.-J. Freund. "Atomic Arrangement in Two-Dimensional Silica: From Crystalline to Vitreous Structures." In: *J. Phys. Chem. C* 116.38 (2012), pp. 20426–20432.

[79] L. Lichtenstein, M. Heyde, and H.-J. Freund. "Crystalline-Vitreous Interface in Two Dimensional Silica." In: *Phys. Rev. Lett.* 109 (2012), p. 106101.

[80] E. I. Altman. "Two-Dimensional Silica from Model System to Applications." In: *Chem. Rev.* 122.13 (2022), pp. 11169–11171.

[81] K. M. Burson, L. Gura, B. Kell, C. Büchner, A. L. Lewandowski, M. Heyde, and H.-J. Freund. "Resolving amorphous solid-liquid interfaces by atomic force microscopy." In: *Applied Physics Letters* 108.20 (2016), p. 201602.

[82] K. M. Burson et al. "Mesoscopic Structures and Coexisting Phases in Silica Films." In: *J. Phys. Chem. C* 126.7 (2022), pp. 3736–3742.

[83] D. Kuhness et al. "A Two-Dimensional 'Zigzag' Silica Polymorph on a Metal Support." In: *J. Am. Chem. Soc.* 140.19 (2018), pp. 6164–6168.

[84] A. L. Lewandowski et al. "Growth and Atomic-Scale Characterization of Ultrathin Silica and Germania Films: The Crucial Role of the Metal Support." In: *Chemistry (Weinheim an der Bergstrasse, Germany)* 27.33118653 (2021), pp. 1870–1885.

[85] C. Büchner, Z.-J. Wang, K. M. Burson, M.-G. Willinger, M. Heyde, R. Schlögl, and H.-J. Freund. "A Large-Area Transferable Wide Band Gap 2D Silicon Dioxide Layer." In: *ACS Nano* 10.8 (2016), pp. 7982–7989.

[86] G. S. Hutchings et al. "Scalable production of single 2D van der Waals layers through atomic layer deposition: bilayer silica on metal foils and films." In: *2D Materials* 9.2 (2022), p. 021003.

[87] D. Naberezhnyi, L. Mai, N. Doudin, I. Ennen, A. Hütten, E. I. Altman, A. Devi, and P. Dementyev. "Molecular Permeation in Freestanding Bilayer Silica." In: *Nano Lett.* 22.3 (2022), pp. 1287–1293.

[88] J.-Q. Zhong, J. Kestell, I. Waluyo, S. Wilkins, C. Mazzoli, A. Barbour, K. Kaznatcheev, M. Shete, M. Tsapatsis, and J. A. Boscoboinik. "Oxidation and Reduction under Cover: Chemistry at the Confined Space between Ultrathin Nanoporous Silicates and Ru(0001)." In: *J. Phys. Chem. C* 120.15 (2016), pp. 8240–8245.

[89] M. J. Prieto, H. W. Klemm, F. Xiong, D. M. Gottlob, D. Menzel, T. Schmidt, and H.-J. Freund. "Water Formation under Silica Thin Films: Real-Time Observation of a Chemical Reaction in a Physically Confined Space." In: *Angewandte Chemie International Edition* 57.28 (2018), pp. 8749–8753.

[90] H. W. Klemm, M. J. Prieto, F. Xiong, G. B. Hassine, M. Heyde, D. Menzel, M. Sierka, T. Schmidt, and H.-J. Freund. "A Silica Bilayer Supported on Ru(0001): Following the Crystalline-to Vitreous Transformation in Real Time with Spectro-microscopy." In: *Angewandte Chemie International Edition* 59.26 (2020), pp. 10587–10593.

[91] P. Y. Huang, S. Kurasch, J. S. Alden, A. Shekhawat, A. A. Alemi, P. L. McEuen, J. P. Sethna, U. Kaiser, and D. A. Muller. "Imaging Atomic Rearrangements in Two-Dimensional Silica Glass: Watching Silica's Dance." In: *Science* 342.6155 (2013), pp. 224–227.

[92] R. J. Hamers. "Atomic-Resolution Surface Spectroscopy with the Scanning Tunneling Microscope." In: *Annu. Rev. Phys. Chem.* 40.1 (1989), pp. 531–559.

[93] L. Lichtenstein. "The structure of two-dimensional vitreous silica." PhD thesis. Freie Universität, Berlin, 2012.

[94] L. Kuipers, R. W. M. Loos, H. Neerings, J. ter Horst, G. J. Ruwiel, A. P. de Jongh, and J. W. M. Frenken. "Design and performance of a high-temperature, high-speed scanning tunneling microscope." In: *Review of Scientific Instruments* 66.9 (1995), pp. 4557–4565.

[95] R. Curtis, T. Mitsui, and E. Ganz. "An ultrahigh vacuum high speed scanning tunneling microscope." In: *Review of Scientific Instruments* 68.7 (1997), pp. 2790–2796.

[96] C. Y. Nakakura, V. M. Phanse, G. Zheng, G. Bannon, E. I. Altman, and K. P. Lee. "A high-speed variable-temperature ultrahigh vacuum scanning tunneling microscope." In: *Review of Scientific Instruments* 69.9 (1998), pp. 3251–3258.

[97] S. H. Pan, E. W. Hudson, and J. C. Davis. "^{3}He refrigerator based very low temperature scanning tunneling microscope." In: *Review of Scientific Instruments* 70.2 (1999), pp. 1459–1463.

[98] L. Petersen, M. Schunack, B. Schaefer, T. R. Linderoth, P. B. Rasmussen, P. T. Sprunger, E. Laegsgaard, I. Stensgaard, and F. Besenbacher. "A fast-scanning, low- and variable-temperature scanning tunneling microscope." In: *Review of Scientific Instruments* 72.2 (2001), pp. 1438–1444.

[99] G. Schitter and M. J. Rost. "Scanning probe microscopy at video-rate." In: *Materials Today* 11 (2008), pp. 40–48.

[100] M. J. Rost, G. J. C. van Baarle, A. J. Katan, W. M. van Spengen, P. Schakel, W. A. van Loo, T. H. Oosterkamp, and J. W. M. Frenken. "Video-rate scanning probe control challenges: setting the stage for a microscopy revolution." In: *Asian Journal of Control* 11.2 (2009), pp. 110–129.

[101] Y.-C. Yang and O. M. Magnussen. "Thiolate-induced surface reconstruction of Cu(100) electrodes studied by in situ Video-STM." In: *Special Issue in Honour of Kingo Itaya* 716 (2014), pp. 80–86.

[102] J. Frenken and I. Groot. "Seeing dynamic phenomena with live scanning tunneling microscopy." In: *MRS Bulletin* 42.11 (2017), pp. 834–841.

[103] Nanonis. *Nanonis SPM control system*. URL: `https://www.specs-group.com/nanonis/products/mimea/`.

[104] Leiden. *Leiden preamplifier*. URL: `https://leidenprobemicroscopy.com/support-equipment/`.

[105] Vmebus. *SIS3316 digitizer*. URL: `https://www.struck.de/sis3316.html`.

[106] Falco-Systems. *High speed high voltage amplifier WMA-300*. URL: `https://www.falco-systems.com/products.html`.

[107] K. M. Bastiaans, T. Benschop, D. Chatzopoulos, D. Cho, Q. Dong, Y. Jin, and M. P. Allan. "Amplifier for scanning tunneling microscopy at MHz frequencies." In: *Review of Scientific Instruments* 89.9 (2018), p. 093709.

[108] C. Xu, Y. Que, Y. Zhuang, K. Wang, and X. Xiao. "Construction of a gigahertz-bandwidth radio-frequency scanning tunneling microscope based on a commercial low-temperature system." In: *Review of Scientific Instruments* 90.10 (2019), p. 103706.

[109] Q. F. Li, Y. Wang, F. Wang, Y. Hou, and Q. Lu. "100 MHz large bandwidth preamplifier and record-breaking 50 kHz scanning rate quantum point contact mode probe microscopy imaging with atomic resolution." In: *Review of Scientific Instruments* 92.1 (2021), p. 013701.

[110] Y. R. Teo, Y. Yong, and A. J. Fleming. "A comparison of scanning methods and the vertical control implications for scanning probe microscopy." In: *Asian Journal of Control* 20.4 (2018), pp. 1352–1366.

[111] Y. K. Yong, S. O. R. Moheimani, and I. R. Petersen. "High-speed cycloid-scan atomic force microscopy." In: *Nanotechnology* 21.36 (2010), p. 365503.

[112] I. A. Mahmood, S. O. R. Moheimani, and B. Bhikkaji. "A new scanning method for fast atomic force microscopy." In: *IEEE Transactions on Nanotechnology* 10.2 (2011), pp. 203–216.

[113] Y. K. Yong, A. Bazaei, S. O. R. Moheimani, and F. Allgöwer. "Design and control of a novel non-raster scan pattern for fast scanning probe microscopy." In: *IEEE/ASME International Conference on Advanced Intelligent Mechatronics (AIM)*. 2012, pp. 456–461.

[114] Y. K. Yong, A. Bazaei, and S. O. R. Moheimani. "Video-rate Lissajous-scan atomic force microscopy." In: *IEEE Transactions on Nanotechnology* 13.1 (2014), pp. 85–93.

[115] A.-K. Henß, J. Wiechers, R. Schuster, V. Platschkowski, and J. Wintterlin. "A beetle-type, variable-temperature scanning tunneling microscope for video-rate imaging." In: *Japanese Journal of Applied Physics* 59.SN (2020), SN1007.

[116] H. Junkes, H.-J. Freund, L. Gura, M. Heyde, P. Marschalik, and Z. Yang. "Experiment Control with EPICS7 and Symmetric Multiprocessing on RTEMS." In: *16th International Conference on Accelerator and Large Experimental Control Systems (ICALEPCS2017)*. JACoW. 2018, pp. 1762–1766.

[117] K. Shroff, C. Rosati, G. Weiss, K. Kasemir, and E. Smith. "New Java Frameworks for Building Next Generation EPICS Applications." In: *17th International Conference on Accelerator and Large Experimental Control Systems (ICALEPCS2019)*. JACoW, 2019. ISBN: 978-3-95450-209-7.

[118] W. E. Norum. "EPICS on the RTEMS real-time executive for multiprocessor systems." In: *Review of Scientific Instruments* 73.3 (2002), pp. 1560–1562.

[119] S. Veseli. *PvaPy: Python API for EPICS PV Access*. URL: `https://epics.anl.gov/extensions/pvaPy/1.1.0/index.html` (visited on 08/16/2021).

[120] C. R. Harris et al. "Array programming with NumPy." In: *Nature* 585.7825 (2020), pp. 357–362.

[121] M. B. Leonard Gura. *Point Cloud Visualization and Analysis, GitHub repository*. 2021. URL: `https://github.molgen.mpg.de/gura/point_cloud_visualization_and_analyis`.

[122] S. van der Walt, J. L. Schönberger, J. Nunez-Iglesias, F. Boulogne, J. D. Warner, N. Yager, E. Gouillart, T. Yu, the scikit-image contributors, and S. Gomez. "scikit-image: image processing in Python." In: *PeerJ* 2 (2014), e453.

[123] P. Virtanen et al. "SciPy 1.0: Fundamental Algorithms for Scientific Computing in Python." In: *Nature Methods* 17 (2020), pp. 261–272.

[124] A. B. Anderson and M. K. Awad. "Binding of Ru, O, and RuO_n ($n = 1 - 4$) to the Ru(001) surface: Structures, stabilities, and diffusion barriers." In: *Surface Science* 183.1 (1987), pp. 289–301.

[125] I. Matrane, M. Mazroui, and Y. Boughaleb. "Diffusion and adsorption of Au and Pt adatoms on ideal and missing row reconstructed surfaces of Au(110): DFT and EAM calculations." In: *Surface Science* 677 (2018), pp. 83–89.

[126] H. T. Lorensen, J. K. Nørskov, and K. W. Jacobsen. "Mechanisms of self-diffusion on Pt(110)." In: *Phys. Rev. B* 60 (1999), R5149–R5152.

[127] M. Henzler and W. Göpel. *Oberflächenphysik des Festkörpers*. 2nd ed. BG Teubner Stuttgart, 1994.

[128] L. Gura, M. Brinker, P. Marschalik, F. Kalaß, B. Junkes, H. Junkes, M. Heyde, and H.-J. Freund. "Similarities between the real honeycomb and atomic network structures." In: (in submission).

[129] L. Gura, S. Tosoni, A. L. Lewandowski, P. Marschalik, Z. Yang, W.-D. Schneider, M. Heyde, G. Pacchioni, and H.-J. Freund. "Continuous network structure of two-dimensional silica across a supporting metal step edge: An atomic scale study." In: *Phys. Rev. Materials* 5 (2021), p. L071001.

[130] K. M. Burson, C. Büchner, M. Heyde, and H.-J. Freund. "Assessing the amorphousness and periodicity of common domain boundaries in silica bilayers on Ru(0 0 0 1)." In: *Journal of Physics: Condensed Matter* 29.3 (2017), p. 035002.

[131] A. L. Lewandowski, P. Schlexer, C. Büchner, E. M. Davis, H. Burrall, K. M. Burson, W.-D. Schneider, M. Heyde, G. Pacchioni, and H.-J. Freund. "Atomic structure of a metal-supported two-dimensional germania film." In: *Phys. Rev. B* 97 (2018), p. 115406.

[132] A. L. Lewandowski, S. Tosoni, L. Gura, P. Schlexer, P. Marschalik, W.-D. Schneider, M. Heyde, G. Pacchioni, and H.-J. Freund. "From Crystalline to Amorphous Germania Bilayer Films at the Atomic Scale: Preparation and Characterization." In: *Angewandte Chemie International Edition* 58.32 (2019), pp. 10903–10908.

[133] A. L. Lewandowski et al. "Determination of Silica and Germania Film Network Structures on Ru(0001) at the Atomic Scale." In: *J. Phys. Chem. C* 123.13 (2019), pp. 7889–7897.

[134] A. L. Lewandowski, F. Stavale, S. Tosoni, W.-D. Schneider, M. Heyde, G. Pacchioni, and H.-J. Freund. "Assessing the film-substrate interaction in germania films on reconstructed Au(111)." In: *Phys. Rev. B* 100 (2019), p. 241403.

[135] L. Grady. "Random Walks for Image Segmentation." In: *IEEE Transactions on Pattern Analysis and Machine Intelligence* 28.11 (2006), pp. 1768–1783.

[136] Y Iwasawa. "Dynamic oxide interfaces by microscopic techniques at high resolutions." In: *Surface Science* 402-404 (1998), pp. 8–19.

[137] S. Shaikhutdinov and W Weiss. "Adsorbate dynamics on iron oxide surfaces studied by scanning tunneling microscopy." In: *Journal of Molecular Catalysis A: Chemical* 158.1 (2000), pp. 129–133.

[138] E. Wahlström, E. K. Vestergaard, R. Schaub, A. R onnau, M. Vestergaard, E. Lægsgaard, I. Stensgaard, and F. Besenbacher. "Electron Transfer-Induced Dynamics of Oxygen Molecules on the TiO_2(110) Surface." In: *Science* 303.5657 (2004), pp. 511–513.

[139] L. Gura, E. A. Soares, J. Paier, F. Stavale, and H.-J. Freund. "Models for Reactions in Confined Space: Can Surface Science Contribute? A Review and Perspective." In: *Topics in Catalysis* (2023). ISSN: 1572-9028.

[140] L. Gura et al. In: (in preparation).

[141] E. I. Altman and U. D. Schwarz. "Structural and Electronic Heterogeneity of Two Dimensional Amorphous Silica Layers." In: *Advanced Materials Interfaces* 1.7 (2014), p. 1400108.

[142] F. Rossel, M. Pivetta, F. Patthey, E. Ćavar, A. P. Seitsonen, and W.-D. Schneider. "Growth and characterization of fullerene nanocrystals on NaCl/Au(111)." In: *Phys. Rev. B* 84 (2011), p. 075426.

[143] K. Lauwaet, K. Schouteden, E. Janssens, C. Van Haesendonck, P. Lievens, M. I. Trioni, L. Giordano, and G. Pacchioni. "Resolving all atoms of an alkali halide via nanomodulation of the thin NaCl film surface using the Au(111) reconstruction." In: *Phys. Rev. B* 85 (2012), p. 245440.

[144] C. Büchner, L. Lichtenstein, S. Stuckenholz, M. Heyde, F. Ringleb, M. Sterrer, W. E. Kaden, L. Giordano, G. Pacchioni, and H.-J. Freund. "Adsorption of Au and Pd on Ruthenium-Supported Bilayer Silica." In: *The Journal of Physical Chemistry C* 118.36 (2014), pp. 20959–20969.

[145] P. K. Roy and A. Heuer. "Influence of the coordination defects on the dynamics and the potential energy landscape of two-dimensional silica." In: *The Journal of Chemical Physics* 157.17 (2022), p. 174506.

[146] M. Schmid, M. Shishkin, G. Kresse, E. Napetschnig, P. Varga, M. Kulawik, N. Nilius, H.-P. Rust, and H.-J. Freund. "Oxygen-Deficient Line Defects in an Ultrathin Aluminum Oxide Film." In: *Phys. Rev. Lett.* 97 (2006), p. 046101.

[147] S. Nie, N. C. Bartelt, J. M. Wofford, O. D. Dubon, K. F. McCarty, and K. Thürmer. "Scanning tunneling microscopy study of graphene on Au(111): Growth mechanisms and substrate interactions." In: *Phys. Rev. B* 85 (2012), p. 205406.

[148] E. A. Soares, J. Paier, L. Gura, K. Burson, C. Ryczek, Z. Yang, F. Stavale, M. Heyde, and H.-J. Freund. "Structure and registry of the silica bilayer film on Ru(0001) as viewed by LEED and DFT." In: *Phys. Chem. Chem. Phys.* 24 (48 2022), pp. 29721–29730.

ACKNOWLEDGMENTS

First and foremost, I am very grateful to my supervisor Prof. Hans-Joachim Freund. Thanks to him I had the unique chance to work on this very inspiring project including the realization of unconventional ideas. Prof. Freund always encouraged me to try new approaches and gave me plenty of opportunity for independent work. He enabled fantastic exchanges with excellent researchers all over the world. For these great experiences I am very grateful.

I want to thank Prof. Klaus Rademann from the Humboldt Universität Berlin for being my second supervisor and I want to thank him and Prof. Nicola Pinna for interesting scientific discussions during the last years.

I truly enjoyed working in the group of Markus Heyde and I am very inspired by his endless enthusiasm and optimism. I benefited a lot from his experimental expertise, especially in the field of SPM. Without his knowledge the project would not have been successful. More importantly, I want to thank him for his helpful and warm advice.

I am very grateful for the fruitful discussions with Prof. Wolf-Dieter Schneider during his monthly visits at the FHI and during international conferences. I benefited a lot from his valuable experience and his constructive feedback.

I enjoyed collaborating with Joachim Paier, Prof. Gianfranco Pacchioni, and Sergio Tosoni, who provided the theoretical calculations that support our experimental measurements. I am happy that collaborations are still ongoing in the context of various projects.

Heinz Junkes has done an amazing job regarding the heart of our high speed electronics. I want to thank him for setting up the custom electronics and the sophisticated data acquisition with us. The high-speed scans would not have been possible without him. It was always great fun to work together and I could broaden my knowledge in the field of data handling, data processing, and programming in general. I am very happy that our work is still ongoing and we are still driven by the aim to push the limits of high-speed STM even further.

The high quality STM measurements would not have been possible without the enormous help in the laboratory with designing and building the machine. Besides my supervisors and collaborators acknowledged above, I want to thank especially Zechao Yang who spent so many long days with me in the laboratory.

I want to thank Patrik Marschalik for the accurate concept development and planning of our software solutions. I enjoyed the interdisci-

plinary exchange in our office. Most importantly, I enjoyed our leisure time activities, our bike and running trips.

Matthias Brinker enabled the user friendly analysis of more than half a million STM images that we acquired in the last few years. His programming skills and his experience in the visualization of point clouds enabled the analysis of this amount of data. I could not be more grateful that he implemented and complemented my ideas to the program which enabled an interactive analysis of the extensive image sequences. More importantly, I want to thank Matthias for our close friendship since primary school.

Regarding the mechanical design, I want to acknowledge the ingenious design skills and brilliant ideas from Jens Hartmann. I enjoyed our discussion about design features and our refreshing conversations.

Also Burkhard Kell and Gero Thielsch helped building the machine from the very beginning and I was always very grateful for their valuable expertise.

Klaus Peter Vogelgesang could always joke about everyday problems while he was carrying out fantastic artworks for the mechanical design of our STM. I want to thank him for producing custom parts for us in the shortest possible time. More importantly, I want to thank him for sharing his inspiring and refreshing mindset.

The whole design process could only be realized thanks to the help and consultancy of the mechanical Workshop, the electronic workshop, and the IT department PP&B.

Florian Kalaß never hesitated to perform some additional analysis to prove our ideas. I want to thank him for working with me on the Phoebus user interface and the data analysis.

The implementation of the experimental setup into the EPICS framework and customizing the Phoebus interface would not have been possible without the help of William Kirstaedter. He solved every issue we had with EPICS and Phoebus, for which I am very grateful.

I want to thank the members of the former SPM group and of the Chemical Physics department of the FHI in general for fruitful discussions and a great time.

Especially, I want to thank Adrián Lewandowski and Mauricio Prieto for fruitful discussions regarding the silica and germania film. I enjoyed conversations - especially the ones in Spanish - at different occasions inside and outside the FHI. I want to thank Adrián for the company during fun sport activities at workshops in Ringberg and for his friendship, which we still maintain.

I want to thank Manuela Misch for her perfectly organized and efficient way to deal with administrative tasks. I am amazed how calm and nice we could talk while she was capable of considering the smallest details of our projects.

I want to thank Kristen Burson, Edmar Soares, and Fernando Stavale for fruitful collaborations at the FHI. Especially, I would like to thank

Kristen Burson for her great company in the laboratory and in the office. She was an amazing supervisor at my very first stay during an internship at the FHI.

I am grateful that I was part of the International Max Planck Research School "Functional Interfaces in Physics and Chemistry" and "Elementary Processes in Physical Chemistry", where I enjoyed scientific symposia, soft skill training, and interesting seminars.

I want to thank my close friends in Gießen, Darmstadt, Madrid, and Berlin for supporting me during the last years. They helped me to maintain the proper balance in life with sport activities like Capoeira, kick boxing, and fantastic bike rides. I will always remember the drum sessions full of energy, the cozy board game evenings, and the fancy cooking sessions in Berlin, during nice trips, and on vacation.

I am very fortunate to have a wonderful family that supports and encourages me in every way. Especially, I want to thank my mother Barbara Gura, my father Josef Gura, my little brother Julian Gura, and my wife Karolin Gura for their great support.

DECLARATION

I declare that I have completed the thesis independently using only the aids and tools specified. I have not applied for a doctor's degree in the doctoral subject elsewhere and do not hold a corresponding doctor's degree. I have taken due note of the Faculty of Mathematics and Natural Sciences PhD Regulations, published in the Official Gazette of Humboldt-Universität zu Berlin no. 42/2018 on 11/07/2018.

Berlin, November 2022

Leonard Gordian Gura